Master Thesis

Numerical investigation of heat transfer on propeller ice protection systems for unmanned aerial vehicles

cand. aer. Markus Frey

October 2023

Institut für Thermodynamik der Luft- und Raumfahrt
der Universität Stuttgart

Direktor: Professor Dr.-Ing. B. Weigand

Universität Stuttgart
INSTITUT FÜR THERMODYNAMIK DER LUFT- UND RAUMFAHRT
Direktor: Professor Dr.-Ing. B. Weigand
Pfaffenwaldring 31, 70569 Stuttgart, Germany · http://www.itlr.uni-stuttgart.de

Master Thesis

for cand. aer. Markus Frey

Numerical investigation of heat transfer on propeller ice protection systems for unmanned aerial vehicles

Description:

A key limitation to the operational envelope of medium-sized fixed-wing unmanned aerial vehicles (UAVs) today is the risk of atmospheric in-flight icing. In contrast to icing in manned aviation, UAV icing is not well established and is an emerging research topic. The Norwegian University of Science and Technology (NTNU) is offering a master thesis on the topic of ice protection systems on UAVs.

The main objective of this project is to run computational fluid dynamics (CFD) simulations for an UAV ice protection system. An electro-thermal ice protection system prevents the ice accretion on the propeller by the use of electrical heaters. Simulations are to be conducted on a 2D UAV propeller section with the CFD tool ANSYS FENSAP-ICE. The simulations will resolve the airflow around the airfoil and the conjugated heat transfer inside the airfoil. Experimental results from icing wind tunnel tests are to be used for validating the simulations. The outcome of this thesis will be used to optimize the design and operation mode of an ice protection system developed in cooperation with UBIQ Aerospace.

Fig.1: Ice on a UAV propeller

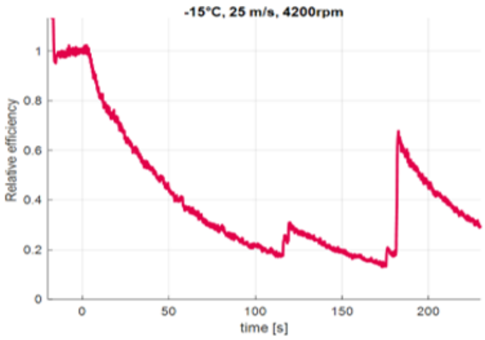

Fig. 2: Performance of a propeller in icing conditions

Tasks:

- Literature study ice protection systems, and icing on UAV propellers
- Validate conjugated heat transfer simulations using ANSYS FENSAP-ICE of the internal temperatures of a propeller with literature values.
- Conduct experiments in an icing wind tunnel to measure the internal temperatures of a UAV propeller with an existing ice protection system.
- Comparison of numerical results on the existing ice protection system layout to the experimental results.
- Optimize the ice protection system for the propeller based on numerical results
- Critical discussion of results

Facility and Duration:

The thesis will be conducted at the Norwegian University of Science and Technology (NTNU) in Trondheim within a 6-month time frame.

Acknowledgements

The numerical simulations were performed on resources provided by the National Infrastructure for High Performance Computing and Data Storage in Norway (UNINETT Sigma2) on the Fram supercomputer, under project code NN9613K Notur/NorStore.

I would like to thank all of my supervisors M.Sc. Nicolas Müller, Dr. Richard Hann and Prof. Dr. Bernhard Weigand for their support during my master’s thesis in Trondheim, Norway. Additionally, I appreciate the opportunity to participate in the experimental campaign in Helsinki, Finland, which added practical depth to my work.

Summary

Ice accumulation on the surfaces of unmanned aerial vehicles (UAVs), particularly on propellers during in-flight conditions, can lead to severe flight performance degradations or even complete loss of control. This study investigates the effectiveness of an electro-thermal ice protection system (ETIPS) to prevent ice formation on UAV propellers.

The propeller material is a composite material and has a low temperature threshold. Therefore, the ETIPS design needs to be optimized to prevent the propeller from being damaged by high temperatures, while still allowing the ETIPS to generate enough heat flux to ensure anti-icing of the propellers. This trade-off between material protection and anti-icing effectiveness is a critical aspect of the study. The propeller and the ETIPS is analyzed numerically using conjugated heat transfer simulations within ANSYS FENSAP-ICE to predict the temperature distribution and heat fluxes through the propeller geometry/body. The simulations are validated with results from the literature experiments in an icing wind tunnel are performed on a ETIPS of a propeller. The results from the experiments are compared to the numerical simulations to verify the simulation models. The conditions of the simulations and experiments are representative for realistic and critical in-flight conditions to examine the ETIPS performance, the required heat fluxes and temperature distributions for a better understanding of the underlying phenomena during the process of anti-icing. The results gained out of the simulations are used to optimize the ETIPS design to ensure that the ETIPS achieves its objectives without negative impacts on the propellers. This study is important to improve already existing ETIPS setups by enlarging the heated area and improve the internal temperature distribution by integrating a highly thermally conductive layer. These approaches lay the foundation for future ETIPS and enable UAVs to operate in potential icing conditions.

Zusammenfassung

Für den sicheren Betrieb unbemannter Luftfahrzeuge stellt die Ansammlung von Eis auf kritischen Oberflächen wie Propellern eine erhebliche Gefahr dar. Dies kann nicht nur zu beträchtlichen Einbußen des Schubes führen, sondern einen vollständigen Verlust der Kontrolle bedeuten. Die vorliegende Studie beschäftigt sich mit der Wirksamkeit von elektrothermischen Eis-Schutz-Systemen, welche die Bildung von Eis auf Propellern verhindern sollen.

Der typische Propeller solcher Luftfahrzeuge besteht aus einem Verbundwerkstoff, welcher einen niedrigen Grenzwert für die maximal zulässige Temperatur aufweist. Das hat zur Folge, dass das Design des Vereisungs-Schutz-Systems dahingehend angepasst werden muss, um einerseits die Propellerflächen eisfrei aber gleichzeitig den Wärmeeintrag in das Material so gering wie möglich zu halten. Dieses Spannungsfeld stellt einen kritischen Aspekt der Studie dar. Zur Untersuchung kommt die Software ANSYS FENSAP-ICE zum Einsatz. Die konjugierten Wärmeübertragungssimulationen zeigen die internen Temperaturverteilungen und Wärmeströme während des anti-icing Prozesses auf. Die numerischen Simulationen werden einerseits mit Ergebnissen aus der Literatur validiert als auch mit den Ergebnissen eines eigens dafür im Vereisungswindkanal der Universität Helsinki aufgebauten Ergebnisse verglichen. Um klimatisch realistische Rahmenbedingungen zu erhalten wurden sowohl die Bedingungen der Experimente als auch die Parameter der Simulationen entsprechend gewählt. Damit können erforderliche Wärmeströme und interne Temperaturverteilungen sehr realitätsnah untersucht und zugrundeliegende Mechanismen bestmöglich nachgebildet werden. Die aus den Experimenten und Simulationen gewonnenen Erkenntnisse legen die Basis für die Optimierung des Designs um strukturelle Veränderungen aufgrund thermaler Einwirkungen zu vermeiden. Diese Studie stellt einen wichtigen Baustein dar um bestehende Eis-Schutz-Systeme weiter zu verbessern, neue zu entwickeln und einen sicheren Betrieb von Luftfahrzeugen unter klimatisch kritischen Bedingungen zu gewährleisten.

Contents

List of figures

List of tables

List of symbols

Latin symbols

Symbol	Unit	Explanation
$\dot{m}_{\mathrm{evap}}$	kg/s	Evaporative mass flux
$\dot{m}_{\mathrm{ice}}$	kg/s	Ice mass flux
$\bar{u}_{\mathrm{f}}$	m/s	Averaged film velocity
$\tilde{u}_{\mathrm{i}}$	m/s	Mean flow velocity
h_{f}	mm	Water film thickness
C_{P}	-	Power coefficient
C_{M}	-	Momentum coefficient
C_{T}	-	Thrust coefficient
F_{G}	kg m/s^2	Gravitational force
Q_{t}	kg m/s^2	Total heat
R_{i}	-	Residual at an element
Re_{d}	-	Droplet Reynolds number
V^{e}	m^3	Element Volume
W_{i}	-	Weight factor
c_{p}	J/(kgK)	Specific heat capacity at constant pressure
c	J/(kgK)	Specific heat capacity
cd_{d}	-	Droplet drag coefficient
d_{r}	m	Radial distance
$\bar{p}$	kg/(ms)	Averaged pressure
p_{s}	kg/(ms)	Static pressure

p_{t}	kg/(ms)	Total pressure
u_{a}	m/s	Air velocity
u_{d}	m/s	Droplet velocity
u_{i}	m/s	Induced velocity
u_{i}''	m/s	Fluctuating flow velocity
u_{T}	m/s	Velocity due to propeller rotation
y^{+}	-	Dimensionless wall distance
h	W/(m^{2}K)	Heat transfer coefficient
A	m^2	Propeller plane area
D	kg m/s^2	Drag
E	kg m^2/s^2	Energy
Fr	-	Froude number
H	kg m^2/s^2	Enthalpy
J	-	Advanced ratio
K	-	Droplet inertia parameter
L	kg m/s^2	Lift
P	W	Power
M	kg m^2/s^2	Momentum
R	K/W	Thermal resistance
Re	-	Reynolds number
S	m^2	Reference are
T	K or °C	Temperature
Tr	Kg m/s^2	Thrust
U	m/s	Propeller inflow velocity
C_{D}	-	Drag coefficient
C_{L}	-	Lift coefficient
d	m	Diameter or distance
f	-	Solutions
g	m/s^2	Gravitational acceleration
k	W/(mK)	Thermal conductivity
l	m	Length
m	kg	Mass

n	1/s	Rotational speed
q	W/m^2	Heat flux density
q_i	W/m^3	Heat source
q_wall	W/m^2	Wall heat flux density
t	s	Time
u	m/s	Flow velocity
x, y, z	m	Cartesian coordinates

Greek symbols

Symbol	**Unit**	**Explanation**
μ_t	m^2/s	Eddy viscosity
μ_w	kg/(ms)	Water dynamic viscosity
$\bar{\rho}$	kg/m^3	Averaged density
ρ_w	kg/m^3	Water density
Δ	-	Difference
Ω	1/s	Propeller rotation rate
α	-	Water volume fraction
η	%	Efficiency
θ	°	Pitch angle
κ	-	Adiabatic index
μ	kg/(ms)	Dynamic viscosity
ν	m^2/s	Kinematic viscosity
ρ	kg/m^3	Density
τ	kg/(ms^2)	Shear stress
ω	-	Relaxation parameter
ϕ	°	Apparent angle

Subscripts

Symbol	**Explanation**
0, 1, 2	Position numbers
∞	Free stream

a	Air
coarse	Coarse
d	Droplet
equ	Equal
evap	Evaporation
f	Film
fine	Fine
G	Gravity
i, j	Element
ice	Ice
P	Power
p	Constant pressure
M	Momentum
r	radial
s	Static
sol	Solid
subl	Sublimation
t	Total
T	Thrust
w	Water
wall	Wall

Superscripts

Symbol	**Explanation**
$''$	Fluctuating part
c	Error order
coarse	Coarse
e	Element
int	Interface
k	State
new	New
old	Old
RANS	Reynolds-averaged navier-stokes

Abbreviations

Symbol	**Explanation**
AOA	Angle of attack

CAD	Computer aided design
CFD	Computational fluid dynamics
CHT	Conjugate heat transfer
DNS	Direct numerical simulation
EID	Extended Icing Data model
ETIPS	Electro-thermal ice protection system
HF	Heat flux
HTC	Heat transfer coefficient
IPS	Ice protection system
LWC	Liquid water content
MVD	Median volume diameter
NRMS	Normalized root mean square
RANS	Reynolds-averaged Navier-Stokes equations
RMS	Root mean square
RPM	Revolutions per minute
SST	Shear stress transport
UAV	Unmanned aerial vehicle
VTT	Technical research center of Finland

1 Introduction

1.1 Scientific background

Until today, the field of applications for unmanned aerial vehicles (UAVs) continues to expand constantly [1]. They can be found in civil sectors as well as in military sectors. Due to the continuous development and widely spread applications, various adverse weather conditions need to be handled during operations. In particular, the phenomenon of freezing of supercooled water droplets on aircraft surfaces poses a hazard. Hence, in-flight icing, which leads to strong aerodynamic degradations or even complete loss of the aircraft, is an issue not only occurring in manned aviation anymore.

In manned aviation, icing research already began back in the 1940s doing experiments and flight tests to gain a better understanding of the process of ice accretion and further to develop the first ice protection systems [2]. Later, in 1970s and 1980s when the first powerful computers were introduced several icing models and numerical tools improved the investigation of the ongoing phenomena. Therefore, icing on manned aviation is a well understood problem and safety has significantly increased as a result [3]. On the other hand, the focus and examination of icing on UAVs started much later. The development of the first UAV dates back to 1917, but due to more complex technology required compared for manned aviation, the initial focus was primarily on achieving autonomous flight capability and increasing operational range [1]. Furthermore, the UAVs were mostly built for military purposes with use in warm areas where no icing occurs. The first mentioned hazard of UAV icing dates back to 1990 was described by Siquig [4]. Only in the last decades UAVs have become more and more applications in civil sectors, as described in section 2.1. The study of icing phenomena and the development of IPS for UAVs is therefore still an open field for much research.

Figure 1.1: Fixed-wing UAV in critical icing conditions [5]

The knowledge gained from research in manned aviation cannot simply be transferred to UAVs due to several reasons [3]. The main aspects that have the biggest influence are size, velocity, weight and materials. The smaller propellers typically spin faster that lead to more ice accretion in shorter time. The smaller size and usually lower velocities, depending on the mission profile and propulsion, result in a significantly lower Reynolds number than for manned aviation. Whereas manned aircraft typically operates at Reynolds numbers of $Re = 10^7 - 10^9$, UAVs operate at lower numbers of $Re = 10^5 - 10^7$. These lower Reynolds numbers change the flow characteristics from a turbulent one to a more laminar flow [6]. It was found that lower Reynolds number regimes lead to more ice accretion of glaze ice and a reduction of rime ice [7].

Important research in this field shows the work by Hann et al. [8]. The basic research results from his team about predicting ice accretion and its effects provided the foundation for developing ice protection systems for essential parts of UAVs. The focus is set on experimental as well as numerical studies of electro-thermal anti-icing and de-icing IPS.

1.2 Motivation

In addition to manned aviation, unmanned aviation represents an emerging technology that is gaining in importance [1]. Those aircraft are used in commercial, military, research and search and rescue (SAR) applications. Especially in recent years, UAVs have been increasingly used in the field of delivering medications and first aid packages to highly remote and inaccessible locations [9]. A variety of these locations are situated in extreme northern latitudes, where the land routes are often cut off by heavy snow and ice, with no suitably lading site for large aircraft. The fast accessibility by UAVs is often the only possibility to provide assist in emergencies to the people living there. To reliably perform these tasks, UAVs must operate in the most challenging weather conditions. One of the greatest dangers occur when flying through a cloud containing supercooled droplets [10]. These droplets freeze immediately when impinging on any surface. The resulting ice formation can lead to significant limitations in flight capability and controllability [11]. Especially propellers are sensitive to ice accretion due to their smaller size and high rotation rate. The consequence is a reduction in thrust generation and increase in required power. In response to these dangers, research on ice protection systems (IPS) represent an important step to increase safety during flight. While IPS for manned aviation have been well established for some time, adapting these systems for UAVs has presented unique challenges due to limited energy availability and strict mass constraints in small UAVs. A leading position in this research field and development of an ice protection system for UAVs represents UBIQ Aerospace [12]. The focus is on a fixed-wing UAV with a wingspan of a few meters and a maximum take-off weight of around 25 kg. These UAVs use composite propellers to produce thrust in contrast to larger UAVs with jet engines. Composite materials convince with low weight and high strength at the same time. While the main goal is to keep the propeller ice-free by electro-thermal heating, the thermal impact on the propeller structure and materials is also an aspect that should not be neglected. Especially, the glass transition temperature states an upper limit of operating conditions to prevent structural changes and maintain instabilities [13].

This thesis focuses on both experimental and numerical investigations of the internal structural temperature distribution of an existing ETIPS design for an UAV propeller. The work conduct studies on thermodynamic factors like heat conduction and heat transfer coefficient and aerodynamic aspects such as flow behavior and relative velocities. On this basis, two improvements of the IPS design are demonstrated. One focuses on enlarging the heated area of the propeller, whereas the second deals with thermal hotspots by integrating highly conductive layers in the propeller structure. Both promising approaches set the foundation for the development of future ETIPS designs. This work represents an important step in enhancing flight safety in extreme weather conditions. Expanding the applications of UAVs in the fields of research, search and rescue and emergency response to geographically- and weather-condition-challenging locations.

1.3 Outline

The present work is structured in this brief introductory chapter, followed by chapter 2, which reviews UAV types, aerodynamic and thermodynamic fundamentals, especially for propellers and the icing process in general. Chapter 3 focuses on the essential numerical as well as analytical methods and approaches for this study. Numerical simulation methods on the one hand and analytical assumptions and approaches on the other hand are described there. Chapter 4 comprises the experimental work for the validation of the numerical simulations, which is described, analyzed and discussed in the following chapter 5. The final optimization approaches, which are derived on basis of the findings from chapters 4 and 5 are elaborated in chapter 6. A critical discussion about the results is included in each chapter respectively as well as potential future work topics. The final chapter 7 shows a conclusion about all the work done.

2 Literature review

2.1 Unmanned aerial vehicles

When studying unmanned aerial vehicles (UAVs), the initial association often pertains to compact quadcopters, commonly referred to as drones. UAVs in general are controlled remotely or fly autonomously on pre-designed routes and without the presence of a human pilot on board [14]. These vehicles can have a wingspan as big as a Boeing 737 or even a diameter of just a few centimeters and can therefore be optimized for their specific mission objectives. There are many different possibilities to distinguish between different types of UAVs considering the size, mass, speed, design or mission to just name a few [14]. Due to the big variety and adaptability to missions without the necessity of taking care of a pilot, UAVs find applications in various fields such as military, delivery, transportation, research or observation as described by Ramesh and Muruga Lal Jeyan [15]. A start-up named Zipline just invented delivery drones to reduce cost and time by delivering parcels autonomously [16].

Figure 2.1: Example of a fixed-wing UAV (left) [17] and a rotary-wing UAV (right) [18]

The two fundamental design concepts are the following. The first concept is a fixed-wing UAV that generates thrust by one or more engines in forward direction like usual manned aircraft. The second concept is the so-called rotary-wing configuration that uses one or more rotors to generate thrust in vertical direction like manned helicopters. Both concepts can be seen in Figure 2.1. The rotary-wing configuration is able to hover, take-off and land vertically and is very flexible in maneuvering by tilting the rotor plane. Nevertheless, due to a required thrust-to-weight ratio it has much shorter flight times than the fixed-wing configuration. Despite this fact, the fixed-wing configuration is the mostly used setup for UAVs until today as it has excellent properties like reaching much higher speeds, a maximum take-off weight, longer flight times due to excellent ratios of flown distance and losing altitude as well as thrust-to-weight ratios of less than one [10] [15].

2.2 Aerodynamic and thermodynamic fundamentals

2.2.1 Aircraft aerodynamics

In literature, there are different approaches available to describe aircraft aerodynamics. The basics are found in the conservation equations of mass, momentum and energy of the flow around an airfoil as described by Charles [19]. The two main theories are set by Bernoulli and Newton which are coupled over the lift force L as described in the following [19]. Newton's theory is based on the conservation of momentum and points on a bigger scale than Bernoulli focuses on. It describes the four forces acting on an aircraft in a stationary horizontal flight as shown in Figure 2.2. The lift force L compensates the weight force F_{G} to maintain at a constant altitude and the thrust F_{N} stands opposite the drag D to maintain at a constant forward speed [20].

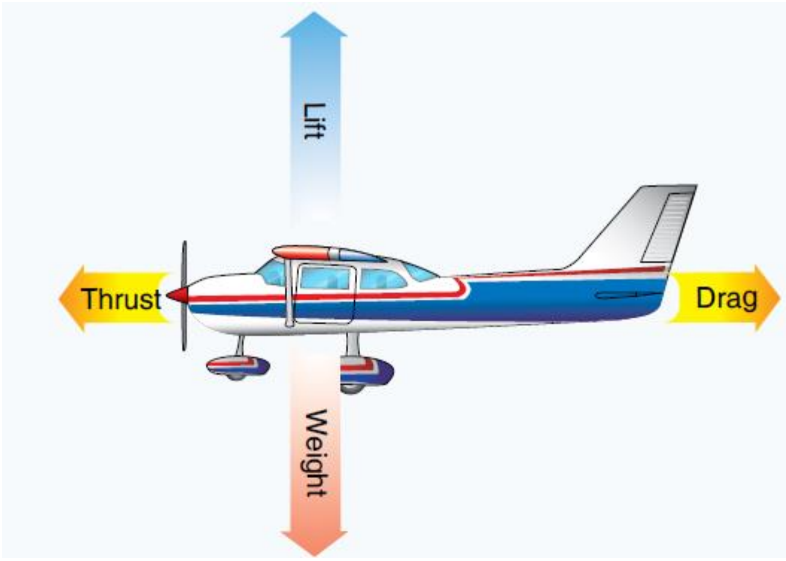

Figure 2.2: Aerodynamic forces acting on an aircraft [21]

In addition, the Bernoulli theory describes the connection between the flow speed and pressure of the fluid [19]. The principle assumes a laminar flow of an incompressible fluid. It describes the phenomenon that pressure decreases when the flow velocity increases. Thus, considering the geometry of an aircraft's wing the flow velocity increases when the air overflows the airfoil, which leads to a decreasing pressure on the upper side of the airfoil. Reversed for the lower side. This difference in pressure between the upper and lower side produces lift for the aircraft. A simplified version of the Bernoulli principle, is described by equation (2.1) where p_{t} describes the total pressure, p_{s} the static pressure, ρ the density and u the velocity [19].

$$p_{\mathrm{t}} = p_{\mathrm{s}} + \frac{1}{2}\rho u^2 = const. \tag{2.1}$$

Thrust can be produced by a propeller-, turbine- or jet-engine. All of them are based on the principle of accelerating gas that produces a thrust force on the aircraft. A more detailed description of the thrust generation by a propeller can be found in chapter 2.2.2. As described above, thrust must overcome the drag of the aircraft when moving through air. Drag force is the summary of all partial forces that resist the movement of an aircraft and can be divided in different types of drag [21]. It can be calculated using equation (2.2) with C_{D} as drag coefficient, ρ as density of air, v as air velocity and S as reference area of the aircraft.

$$D = \frac{1}{2} C_{\mathrm{D}} \rho u^2 S \tag{2.2}$$

Weight force F_{G} is given by the weight m of the aircraft itself multiplied with the gravity constant g:

$$F_{\mathrm{G}} = mg \tag{2.3}$$

As described above the lift force compensates the weight force in order to stay at a constant altitude. Lift L can be calculated by equation (2.4) with C_{L} as lift coefficient, ρ as density of air, v as air velocity and S as reference area of the aircraft.

$$L = \frac{1}{2} C_{\mathrm{L}} \rho u^2 S \tag{2.4}$$

Lift- and drag coefficient are both dimensionless coefficients to analyze the aerodynamic performance of an aircraft [21].

Furthermore, there is a special field of interest that describes the area near the surface. Since the velocity of the airflow at the surface is zero due to friction, the velocity grows when increasing the distance to the surface until the airflow reaches the free stream velocity. This special region is called a boundary layer and is defined by Schlichting [22] as a distance when the velocity reaches 99% of the free stream velocity. The boundary layer influences not only the aerodynamics but also the thermodynamics due to heat transfer through the layer as described in section 2.2.3. The velocity profile inside the boundary layer depends on the flow type of the air stream, meaning laminar or turbulent conditions. Comparing turbulent with laminar flows, the laminar flow is characterized by a rather thin, stable and ordered structure of layers parallel to the surface with a reduction in drag and is more likely to separate. The turbulent flow on the other hand is characterized by a thicker, rather chaotic and irregular shape and usually consists of small vortexes, also called eddies, with an increased momentum transport through the boundary layer compared to the laminar one. To predict the appearance of these two boundary layers the dimensionless Reynolds number Re is used. The Reynolds number describes the ratio of inertial to viscous forces and indicates if a flow is rather laminar or turbulent. It can be calculated by equation (2.5) with the velocity u, the characteristic length l and the kinematic viscosity ν:

$$Re = \frac{ul}{\nu} \tag{2.5}$$

In a rather small Reynolds number region a laminar flow is prevalent whereas when the Reynolds number increases the transition to a turbulent flow occurs. The transition of the flow is dependent on the velocity of the flow and therewith the pressure gradient but can also be influenced by surface roughness, turbulences in the free stream or obstacles on the surface.

2.2.2 Propeller aerodynamics

Propellers are a category of rotors and the part of an aircraft that generates thrust. There are different types of rotors [23]. If a rotor is used to compress air, it is called a compressor. If it is used to transform energy of a fluid into mechanical energy, it is called a turbine. Rotors are used in many different applications like in wind turbines, helicopters, pumps or engines. The focus in this work is on propellers of aircrafts only.

Comparing a wing with a propeller, both provide a similar working principle in generating lift. The difference is that a propeller is powered by an engine and moves through the surrounding air. Due to the rotation, the propeller is covered by the velocity of an airstream depending on the distance from the rotating axis. The velocity increases by an increasing distance. A characteristic value is the advance ratio J describing the ratio of the axial flow velocity u and the propeller peripheral speed calculated by the rotational speed n and diameter d of the propeller [24]:

$$J = \frac{u}{nd} \tag{2.6}$$

The rotation of the propeller produces different forces. When the air is sucked in at the front side of the propeller and accelerated to the back side, a recoil force from the air on the propeller is produced which is called thrust Tr. The rotation of the propeller and the accompanying drag produces a momentum M around the axis of the propeller. To overcome the momentum, a certain power P by the engine is required to keep the propeller rotating at a constant speed. To analyze and optimize the aerodynamic efficiency and performance of a propeller and make it comparable to different sizes and conditions, the coefficients of thrust C_{T}, momentum C_{M} and power C_{P} are calculated according to equations (2.7), (2.8) and (2.9). As can be seen in the equations below, all coefficients are calculated by ratios of the forces Tr, Q, P to the atmospheric density ρ and the propellers peripheral speed potentiated:

$$C_{\mathrm{T}} = \frac{Tr}{\rho n^2 d^4} \tag{2.7}$$

$$C_{\mathrm{M}} = \frac{M}{\rho n^2 d^5} \tag{2.8}$$

$$C_{\mathrm{P}} = \frac{P}{\rho n^3 d^5} \tag{2.9}$$

For performance analyses of different propeller designs/geometries, the efficiency η is of interest. It is calculated by equation (2.10):

$$\eta = \frac{Tru}{P} = \frac{C_{\mathrm{T}} J}{C_{\mathrm{P}}} \tag{2.10}$$

The equation describes the ratio between the generated thrust and the inserted power and can also be calculated by the coefficients of thrust and power.

Propellers are available in different sizes, shapes and amounts of blades where all of them are optimized for their specific purpose. Another important characteristic value is the pitch that describes how far a propeller would ideally move forward during one rotation. This value influences the thrust and the power of the propeller and is usually measured at 75% of the radius of the propeller [25].

2.2.3 Thermodynamic fundamentals

After considering flow properties, an important part of this study are thermodynamic processes and effects. The most important process is the heat transfer of the propeller. Heat transfer describes the transport of the energy type heat due to a temperature difference [26]. Heat transfer consist of two main mechanisms. The first mechanism requires a medium that transfers the heat, subdivided in conduction and convection. The second mechanism is called radiation and appears without the present of particles [27].

Heat conduction describes the process of energy transport due to the interaction of atoms and molecules. An example is the 1D heat conduction through a solid wall. Important for the heat conduction process are the material properties like wall thickness d, the temperature difference of the wall sides and the thermal conductivity k that describes the intermolecular transport properties. The thermal conductivity of fluids and solids differ by orders of magnitude. While solids show the biggest values (copper: $k = 372\ W/(mK)$), followed by liquids (water: $k = 0.598\ W/(mK)$), gases show the smallest values (air: $k = 0.0278\ W/(mK)$). Considering an isotropic and homogenous wall, the heat flux density q can be expressed according to Fourier [28] in one dimension:

$$q = -k\frac{dT}{dx} \tag{2.11}$$

Equation (2.11) shows that heat transfer requires a spatial temperature gradient and heat is always transferred to the location of lower temperature. Whenever heat conduction passes through a medium, that medium has a thermal resistance R, which can be analogized to electrical resistance. The greater the thermal resistance of a medium, the less efficiently the heat is conducted. As showed in equation (2.12), the resistance depends on the thickness, conductivity and reference area S.

$$R = -\frac{d}{kS} \tag{2.12}$$

If a solid medium consists of several materials arranged in layers, it is important whether the heat conduction is parallel or normal to the layers. For the layers arranged normal to the heat flux, the heat flux density can be described for a 1D steady state problem as:

$$q = \frac{(T_1 - T_2)}{\sum_{\mathrm{i}=1}^{\mathrm{n}} \frac{d_\mathrm{i}}{k_\mathrm{i}}} \tag{2.13}$$

Corresponding if the layers are arranged parallel to the heat flux, one obtains:

$$q = \frac{\sum_{\mathrm{i}=1}^{\mathrm{n}} k_\mathrm{i} \mathrm{d}_\mathrm{i}}{ld}(T_1 - T_2) \tag{2.14}$$

With l as the length of the layers. In addition to equation (2.11), a time-dependent problem with an internal heat source q_i can be expressed in one dimension as

$$\frac{\partial T}{\partial t} = \frac{k}{\rho c_\mathrm{p}}\frac{\partial^2 T}{\partial x^2} + \frac{q_\mathrm{i}}{\rho c_\mathrm{p}} \tag{2.15}$$

and is known as the 1D heat conduction equation. The left part describes the temperature change in time on a location. The first part on the right side considers the heat conductivity due to material properties and describes, combined with the second derivative in x, the spatial temperature change along x. Meaning how fast the temperature along x changes in time also depends on the heat source, considered in the last term on the right side.

Convective heat transfer on the other hand just appears in fluids like liquids or gases. It requires movement of macroscopic particles. Such heat transfer appears when a fluid transports heat. The particles at the wall get heated up, increase their internal energy, move and transport the absorbed heat away from the surface. If external forces influence the fluid flow, one speaks of forced convection in contrast to free convection. An example of forced convection is a flying plane. In this situation, a flow over the airfoil surface can be recognized. In addition to the boundary layer described in section 2.2.1, a temperature boundary layer appears. It is characterized by having the wall temperature T_{wall} at the heated surface decreasing over the boundary layer until reaching the free flow temperature T_∞. In a laminar boundary layer, the heat transfer from the surface normal to the stream lines happens by conduction which is forced by the temperature difference of the surface temperature and the free flow temperature. In a turbulent boundary layer, the flow is much more mixed up and therefore, the transportation of heat away from the surface is more efficient. Introducing the heat transfer coefficient (HTC) h, the following equation describes the intensity of heat exchange on an interface:

$$h = \frac{q_{\mathrm{wall}}}{T_{\mathrm{wall}} - T_{\infty}} \tag{2.16}$$

Equation (2.16) shows a definition of the heat transfer coefficient that is dependent on many influencing material- and flow-properties like density, velocity, geometry and the specific heat at constant pressure c_{p}:

$$c_{\mathrm{p}} = \frac{\Delta Q_{\mathrm{t}}}{m\Delta T} \mid p = const. \tag{2.17}$$

Equation (2.17) describes the heat capacity of a medium normalized by the mass m, which is known as specific heat at constant pressure. It is defined as the ratio of change in heat ΔQ_{t} and the corresponding change in temperature ΔT.

Another form of transferring heat is due to radiation. This mechanism is based on electromagnetic waves and appears even in vacuum [26]. Every structure with a temperature higher than 0 K is emitting energy in the form of heat. The intensity is dependent on the bodys' properties and temperature as described by the law of Stefan-Boltzmann [29]. In comparison to heat conduction and convection, radiation is negligible in the present work.

Regarding inflight icing of UAVs, other effects due to a water film on the surface, ice accretion and air flow over the airfoil lead to several effects which interact with each other and make the understanding even more complex. When water droplets impinge onto a surface, their kinetic energy is transferred to the surface. The kinetic energy is converted into thermal energy and the surface gets heated up. The amount of energy is dependent on the droplet size and velocity. The amount of heat due to droplet impingement is relatively small, especially when the surface is already heated by an ice protection system (IPS), the temperature rise due to droplet impingement can therefore be neglected in several cases. Furthermore, the impinging droplets create a water film on the surface that in turn show several influences on the heat balance. The heat is transferred from the solid in the water dependent on the HTC as described above. The water gets warmer and the solid cools down. The heated water molecules get a rise in kinetic energy and move to the liquid and gas interface. When the latent evaporative heat is big enough, a phase transition from liquid to gas is the result. This process is called evaporation and leads to a noticeable decrease of temperature in the surroundings also known as evaporative cooling [30]. This phenomenon depends on several aspects. The velocity, humidity and with it the temperature of the surrounding air has a big influence [31]. On the other hand, when the liquid water film reaches surface areas with a temperature below zero degree, a phase transition from liquid to solid ice appears. During this transition, the energy of the molecules reduces and the latent heat is transferred to the surroundings that is heated up slightly.

2.3 Inflight icing of manned and unmanned aerial vehicles

Inflight icing describes phenomena during a flight of manned or unmanned aerial vehicles when ice accumulates on surfaces of wings or propellers. It poses a great hazard to the aircraft due to performance degradations. Inflight icing occurs in supercooled conditions found in clouds. Under these conditions, the temperature of the liquid droplets is lower than the freezing point but without freezing, so called supercooled droplets. The impingement of the droplets depends on the size of the droplets. When the mass of a droplet is too big to follow the streamlines around the body, it hits the surface of the aerial vehicle as shown in Figure 2.3. This can happen to several parts of the aircraft like wings, propellers, turbines, pitot tubes and sensors. However, this thesis focuses on the icing of propellers only.

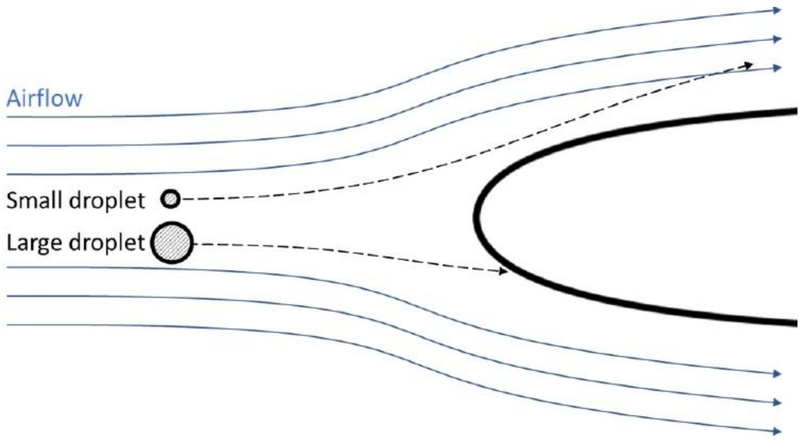

Figure 2.3: Schematic illustration of droplet impingement on airfoil [3]

After colliding with the surface, droplets can instantly freeze or create a water film depending on the heat balance and further lead to different ice shapes that occur on the surface. The two most influencing factors are the enthalpy of fusion and convection. When it comes to a phase change due to freezing, latent heat is released that heats up the colder surrounding air. Convection on the other hand describes the process when heat is transferred from the warmer surface to the colder surrounding air by particles. Both processes depend on three parameters: the ambient temperature, the liquid water content (LWC) and the median volume diameter (MVD). Other influencing parameters like the shape of the aircraft and the relative airspeed must also not be neglected as described by Hann [10].

2.4 Ice types, shapes and their effects

The three most common ice types are rime ice, glaze ice (see Figure 2.4) and mixed ice. All of them are characterized by their own shape and form when accumulating on a surface.

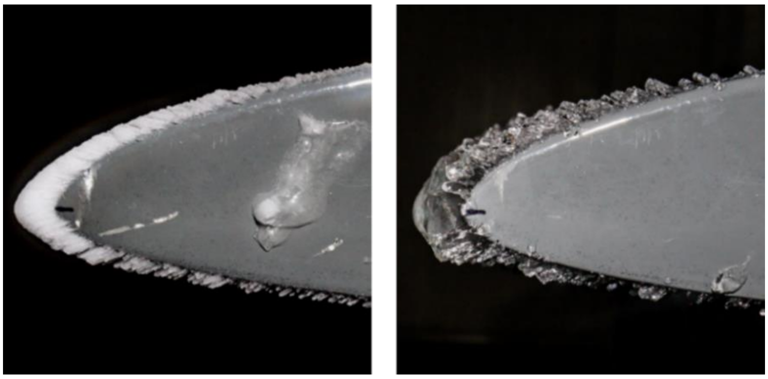

Figure 2.4: Rime ice accreation (left) and glaze ice accreation (right) on an airfoil [3]

In very low temperature regimes, the impinging droplets freeze immediately and generate rime ice. Rime ice is typically white due to enclosed pockets of air, has a rather rough surface, and is usually formed streamwise on the surface as shown in

Figure 2.4. Due to the streamwise form and depending on the icing durations, the influences of rime ice on wing aerodynamics are typically lower than other ice shapes [3].

In the temperature regimes near the freezing point, glaze ice occurs. Therefore, not all impinging droplets freeze immediately but create a liquid water film that freezes gradually on the surface. Glaze ice appears clearer due to the lack of air pockets and creates bigger and more irregular shapes e.g. ice horns as shown in Figure 2.4.

Further shapes and appearances are a combination of rime and glaze ice e.g. mixed ice, supercooled large droplets, snow and cold soaking. More information about this are described by Hann and Johannsen [3].

All the ice appearances described above are due to natural cloud or air conditions. When using ice protection systems a third important ice shape occurs, the so-called runback water or runback ice. The different types of ice protection systems are described in more detail in chapter 2.5. When using an electro-thermal ice protection system, especially the leading edge on the airfoil or propeller is heated up to keep the surface free of ice. Within this study the focus is on such an IPS system. In this case the water on that surface then runs back and freezes later more downstream where the surface is not heated. At this point it forms shapes that are called spanwise-ridge ice as shown in Figure 2.5.

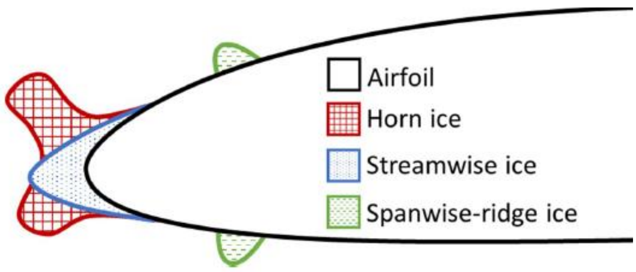

Figure 2.5: Ice shapes on a clean airfoil [3]

Icing effects all four forces (lift, drag, thrust, weight) acting on an aircraft [2]. The biggest influence represents the disturbance of the airflow by the ice shapes leading to lift reduction and drag increase, followed by the additional mass of the accumulated ice [32]. According to Bragg et al. [6] the ice shapes have an influence on aerodynamic properties in a descending order of spanwise-ridge ice, horn ice, streamwise ice and ice roughness.

Ice roughness describes a thin layer of ice on the clean airfoil that increases the roughness of the surface. A rougher surface supports an early laminar-turbulent transition by increased shear stress. The turbulent boundary layer leads to increased drag and further is likely to separation of the flow and the surface with a consequence of a decreased lift and stall angle of an aircraft. Similar influences can be found by the accumulation of stream wise ice. Horn ice and spanwise-ridge ice on the other hand can both be seen as turbulators of the airflow with large recirculating zones behind. While horn ice forces a laminar-turbulent transition right at the leading edge effecting in early separation and reduction in lift and stall angle, spanwise-ridge ice can also be an issue for mechanical parts on a wing. Control surfaces like flaps are usually at the rear part and can be blocked by spanwise-ridge ice [6].

Examination of ice accretion on spinning parts like rotors of helicopters or wind turbines state an extra aspect and significant effort has been invested [33]. In contrast to fixed-wing ice accretion are rotor icing predictions more complex by periodic changing angle of attack and velocity. In addition, make the spanwise changing thickness and curvature the issue even more challenging. Ice does not accrete in a uniform coating on the rotor but rather rough and ragged structure. That causes flow separation and further a considerable reduction in lift/drag ratio. Additional hazard occurs by the high rotational speed that leads to shedding events, which causes extreme vibrational forces on the structure as described in the following.

Regarding propeller icing of small-medium sized fixed-wing UAVs, extensive research shows the work by Müller et al. [34]. Inspections have been made for icing conditions of −5 °C, −10 °C and −15 °C, wind speeds of 25 m/s, propeller rotation speed of 4200 RPM and a LWC of 0.44 g/m^3.

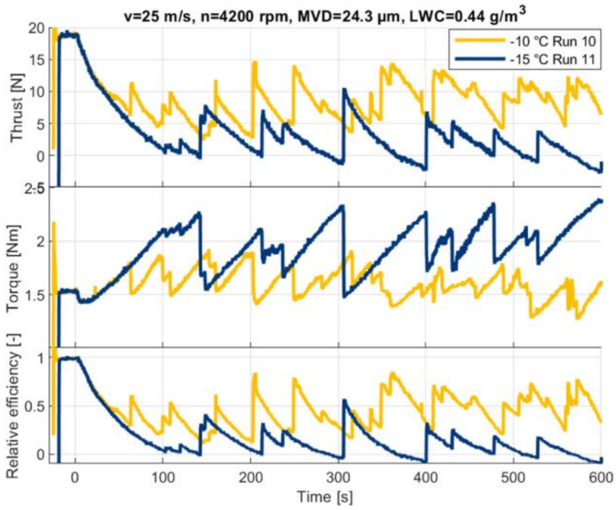

Figure 2.6: Performance degradation of a UAV propeller due to ice accreation over 600 s [34]

The results obtained for the conditions of −10 °C and −15 °C are shown in Figure 2.6. A direct correspondence between decreasing thrust and increasing torque due to ice accumulation on the propeller surface can be seen. The peaks over time, where suddenly the thrust increases followed by an again decreasing phase, are due to ice shedding events. These events happen when the centrifugal forces are too high and the accumulated ice breaks of the surface because the adhesion forces between the ice and surface are not strong enough to keep the ice on the propeller [35]. Despite the fact that ice shedding damps the performance degradation, these events cause extreme vibrational forces on the propeller- and whole mounting-structure and the loosened ice parts are dangerous for the whole UAV [36]. Consequently, to prevent performance degradation and ice shedding events to ensure a safe operation of the aircraft, an IPS is a necessary and critical component.

2.5 Ice protection systems

As stated before, protecting critical parts of aircrafts like the airfoil is essential for ensuring safe flights. Therefore, IPSs have been developed that are not only used in aviation but also for wind turbines for example. In general these systems can be categorized in passive and active techniques [37]. Passive systems prevent ice accumulation without any source of energy, using special coatings and paints. Active IPSs use methods like chemical, mechanical, pneumatic, ultrasonic or electro-thermal to name a few. This thesis focuses on electro-thermal ice protection systems (ETIPS) only. Further information about other techniques can be found by Fakorede et al. [37].

ETIPS usually consist of heating pads embedded in the material. The working principle is based on resistivity heating which involves passing electrical current through a resistive material like wires or carbon fibers. By applying current to ETIPS, the produced heat is transferred through the solid material via heat conductivity resulting in a heated surface, which prevent ice from forming. The active strategy enables on the one hand more flexibility and faster adaptability on changing conditions but on the other hand requires an additional source of energy.

Until today, the development of rotor ice protection systems of helicopters states a critical aspect and a lot of research has been done. Challenging are the rather pointy leading edge of rotor blades and spanwise variations in rotational speed. Nevertheless, on basis of experimental examinations back in 1976, electro-thermal approaches covering the leading edge show great success [38]. Often separated spanwise and equipped with several heating elements further aft around the chord to deal with runback ice [39]. Current improvements are done by powering the elements periodically to minimize the electrical power requirements.

2.6 State of the art

2.6.1 ETIPS design

Only a few available studies of anti-icing IPS tests on propellers of small-medium size UAVs are available. While one focusses on coatings to avoid ice accretion [40], the second one tested an ETIPS, separated spanwise in three parts on propellers for small multi-rotor drones [41]. Most interesting for this study is the work by Müller et al. [34], who developed an ETIPS for a propeller of a small fixed-wing UAV. For the simulations in this study the same propeller is used. The developed ETIPS consists of two unidirectional carbon fiber heating zones in the leading edge as can be seen in Figure 2.7. It measures a width of 7 mm in chord direction of the propeller. The heating zones and wires are connected by resin containing silver additives for electrical connection. The two ETIPS are powered by the power supply of the UAV and consequently have a direct influence on the power of the UAV in general. In the study of Müller et al. [34] the two heating zones are of different thicknesses to regulate the heating along the spanwise direction while keeping a constant power.

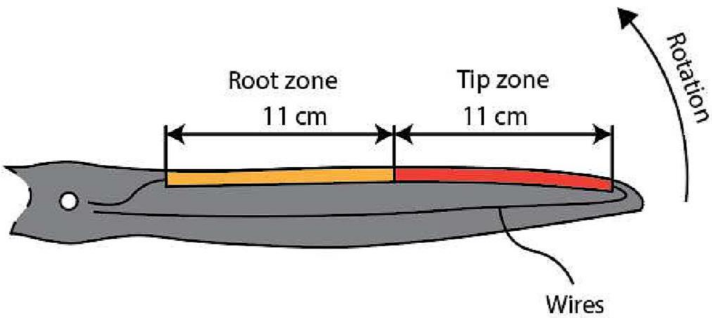

Figure 2.7: Ice protection system position in a UAV propeller [34]

Especially in the root zone, the propeller rotation speed is slower, thus resulting in a decreased inflow compared to the tip zone and consequently smaller heat flux is required to keep the blade ice-free. The heating pad in the root zone measures twice the thickness than the one in the tip zone.

2.6.2 Composite structure of UAV propellers

Most of today's available UAV propellers are made of composite structures. Composite materials show many advantages in comparison to metallic alternatives. On the one hand, composites have a very lightweight while still keeping high stiffness and strength on the other hand [13]. Due to the availability of various combinations of fibres and resins resulting in distinct material properties, along with the flexibility of utilizing different layup configurations, the properties can be further optimized. In addition, composites are insensitive to corrosion and show a high grade of design flexibility due to the manufacturing process as described in the following.

In the manufacturing process of composites on the example of the propeller of Müller et al. [34], the single fibres of usually glass, carbon or polymers are woven or interwoven to get fabric mats of different properties. These mats are layered in the final propeller mould in a process called ‘layup’. Then a resin is injected to connect the single fibres and layers. To cure the resin, the mould is compressed and heated at 60 °C. This whole process shows flexibility in the decision of which materials are used, how they are layered and lead to the possibility to integrate heating layers for ETIPSs into the structure.

An influence of a thermal IPS that is often neglected especially regarding composite structures is the maximal glass transition temperatures of the resin. The glass transition temperature in general describes the temperature at which a material changes from a glass solid state to a rubbery state [42]. This transition influences mainly the materials’ mechanical-, thermal- and electrical-properties [43]. For propeller applications like in this study, the most critical aspects are the change in stiffness and strength that may cause deformations and material instabilities followed by performance degradation or even complete loss of the propeller.

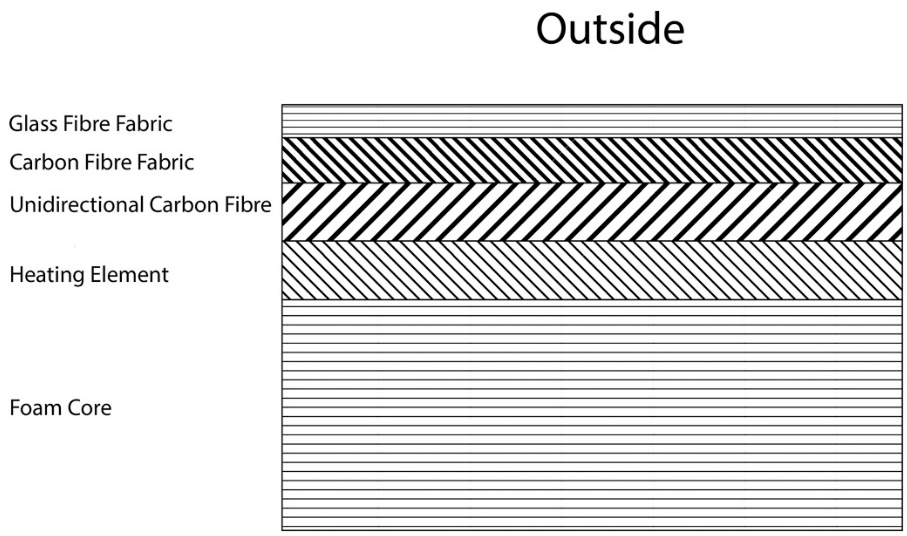

Figure 2.8: Composite structure layup of a UAV propeller [34]

Figure 2.8 shows the composite structure and integrated heating element in the above-described propeller. The heating element is placed right above the foam core and insulated by a glass fiber layer. To find the perfect layup is a crucial step. First, the structure should be strong enough to withstand the aerodynamic and centrifugal forces during a flight. Second, the position of the ETIPS influences the required heat flux and the maximum internal temperature. Third, the propeller structure should stay as light as possible.

All above mentioned aspects result in a complex situation. Neglecting in this study the influences of different composite layups but focusing on the ETIPS design parameters and examinations of the required heat fluxes and internal temperature distribution. On one hand, the ETIPS must generate sufficient heat to prevent the formation of ice on the surface, and on the other hand, it must avoid causing any detrimental effects to the internal structure of the propeller, particularly ensuring that the temperature remains below the glass transition temperature of 60 °C.

3 Numerical and analytical methods

3.1 CFD simulations with ANSYS FENSAP-ICE

For this study the commercial software ANSYS FENSAP-ICE (version 2022R2) with the built-in modules FENSAP, DROP3D, ICE3D, C3D and CHT3D is used [44]. Each of the modules are relevant for a specific aspect of the simulation. The simulation is performed in an iterative process. First, FENSAP is the fluid solver that calculates the airflow around the surface. With the results of FENSAP, DROP3D models the trajectories of the fluid particles and their interaction with the surface. Lastly, ICE3D uses the previous results of FENSAP and DROP3D to simulate the ice accretion on the surface of the airfoil and is used to calculate the required heat fluxes for running-wet cases. Running-wet cases focus on heating the surface of up to around zero degree to avoid water from freezing. In contrast in the fully-evaporative cases surface is heated that much, so that the impinging water is evaporated immediately to avoid any liquid water on the surface. Focusing on the internal heat fluxes and temperature distribution in this thesis, the module C3D is responsible for calculations of heat conduction within the structure. Finally, to iteratively examining all heat transfers between the solid-, ice- and fluid part of the whole setup, the module CHT3D merges all previously announced modules together as shown in Figure 3.1. A detailed description of all FENSAP-ICE modules can be found in the following.

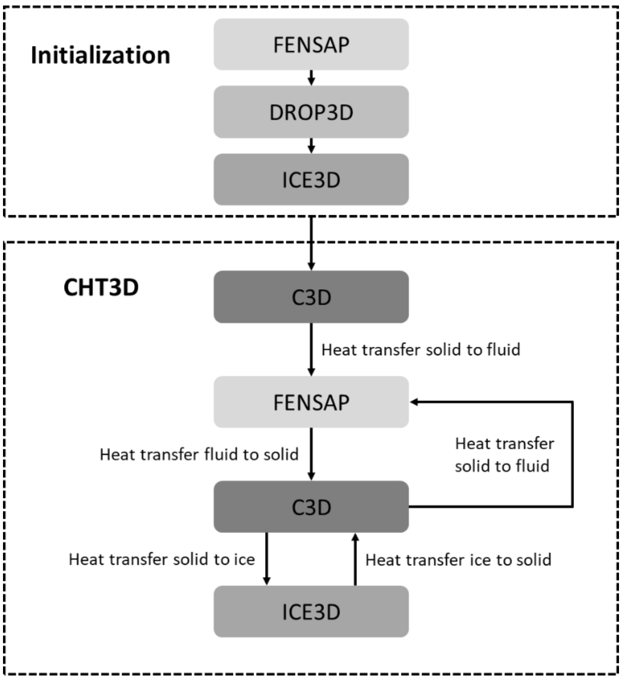

Figure 3.1: Visualisation of CHT3D simualtion loops

3.1.1 FENSAP

FENSAP is an advanced computational fluid dynamics (CFD) solver that can be used as part of a large simulation loop to calculate ice accretion and as a standalone system for simulating aerodynamic performances. In general, FENSAP is able to solve three-dimensional flows, including incompressible and compressible, steady and unsteady as well as viscous and inviscid flows [45]. It uses a weak Galerkin finite element method for spatial discretization [46] and a Newton method to linearize the governing nonlinear equations when solving for a steady-state solution [47].

The calculation of the viscous flow is based on the conservation equations of mass (3.1), momentum of Newtonian fluids (Navier-Stokes equations) (3.2) and energy (3.3). Compared to the Euler equations, these equations consider viscosity to describe the viscous flow [47]. To approximate these equations numerically, boundary conditions need to be defined in advance of the simulation.

$$\frac{\partial \rho}{\partial t} + \frac{\partial}{\partial x_{\mathrm{i}}}(\rho u_{\mathrm{i}}) = 0 \tag{3.1}$$

$$\frac{\partial}{\partial t}(\rho u_{\mathrm{i}}) + \frac{\partial}{\partial x_{\mathrm{j}}}\left(\rho u_{\mathrm{j}} U_{\mathrm{j}}\right) = -\frac{\partial p}{\partial x_{\mathrm{i}}} + \frac{\partial \tau_{\mathrm{ij}}}{\partial x_{\mathrm{j}}} \tag{3.2}$$

$$\frac{\partial}{\partial t}(\rho E) + \frac{\partial}{\partial x_{\mathrm{j}}}\left(\rho u_{\mathrm{j}} H\right) = -\frac{\partial}{\partial x_{\mathrm{j}}}(u_{\mathrm{i}} \tau_{\mathrm{ij}}) + \frac{\partial}{\partial x_{\mathrm{j}}}\left(\kappa \frac{\partial T}{\partial x_{\mathrm{j}}}\right) \tag{3.3}$$

For calculating the physical properties of the continuous flow field, a mesh is generated to discretize the field in a finite number of nodes (finite elements). The properties can only be calculated at the nodes of the mesh and are interpolated for the area in between the nodes [48]. There are several discretization methods for partial differential equations like the Navier-Stokes equations according to Munz and Westerman [49]. One of the most common method is the finite element method. Within this method, finite elements are approximated through mathematical functions that are called basis functions. By integrating the differential equations over these elements, the equations are converted into a system of algebraic equations. The method can be expressed as shown in equation (3.4), with R_{i} describing the residual at an element i, Φ the conservation equation, W_{i} a weight factor and V^{e} the element volume [50]. The result is obtained by minimizing a residual.

$$R_{\mathrm{i}} = \iiint W_{\mathrm{i}} \Phi dV^{\mathrm{e}} \tag{3.4}$$

This method is appropriate for complex geometries and examining material behavior due to a flexible spatial discretization. Further information can be found in [49].

3.1.2 Turbulence models

Until today, the phenomena of turbulence is an extremely complex problem in aerodynamics, which is not yet completely understood. Especially in modeling turbulence flows, several assumptions and simplifications need to be considered. When doing direct numerical simulations (DNS) solving the Navier-Stokes equations as a whole, turbulence must be calculated over the complete spatial range and time scale in order to account for all dissipative scales [47]. This method necessitates finely resolved meshes and results in significant computational expenses. A common approach to bypass these demands are the so called Reynolds Averaged Navier-Stokes (RANS) equations [51]. Within this approach, the solution variables of the Navier-Stokes equations u_{i} are separated in a mean $\tilde{u}_{\mathrm{i}}$ and fluctuating part u_{i}''. The

RANS-equations are time averaged and the turbulent fluctuations are depicted as statistical average values as shown in equation (3.5). To reduce the amount of details lost due to this approach, the Favre-decomposition is a method that considers the density, especially important for cases where the density is not constant. By taking the change in density into account, the turbulence is described in a much more accurate manner and effects like pressure- and viscosity-changes can be observed [52].

$$u_{\mathrm{i}} = \tilde{u}_{\mathrm{i}} + u_{\mathrm{i}}'' \tag{3.5}$$

The average of the fluctuating part is always equal to zero. The Favre-averaged RANS equations can be found by replacing the variables in the continuity and momentum equations by equation (3.5) [53]:

$$\frac{\partial \bar{\rho}}{\partial t} + \frac{\partial}{\partial x_{\mathrm{i}}}(u_{\mathrm{i}}) = 0 \tag{3.6}$$

$$\frac{\partial}{\partial t}(\bar{\rho}\tilde{u}_{\mathrm{i}}) + \frac{\partial}{\partial x_{\mathrm{j}}}\left(\bar{\rho}\tilde{u}_{\mathrm{i}}\tilde{u}_{\mathrm{j}}\right) = \frac{\partial \bar{p}}{\partial x_{\mathrm{i}}} + \frac{\partial}{\partial x_{\mathrm{j}}}\left[\mu\left(\frac{\partial \tilde{u}_{\mathrm{i}}}{\partial x_{\mathrm{j}}} + \frac{ial\tilde{u}_{\mathrm{j}}}{\partial x_{\mathrm{i}}}\right)\right] - \frac{\partial}{\partial x_{\mathrm{j}}}\tilde{\tau}_{\mathrm{ij}}^{\mathrm{RANS}} \tag{3.7}$$

While on the left hand side of equation (3.7) the fluid momentum is described, the right hand side shows viscous stress and Favre-averaged Reynolds stress. The Reynolds stress cannot be calculated directly due to the closure problem. Models are necessary to solve this problem. The first approach by Joseph Boussinesq [54] was to model the Reynolds stress tensor by implementing the eddy viscosity μ_{t}. The so-called Boussinesq hypothesis is described in equation (3.8).

$$-\tilde{\tau}_{\mathrm{ij}}^{\mathrm{RANS}} = \mu_{\mathrm{t}}\left(\frac{\partial \tilde{u}_{\mathrm{i}}}{\partial x_{\mathrm{j}}} + \frac{\partial \tilde{u}_{\mathrm{j}}}{\partial x_{\mathrm{i}}}\right) - \frac{2}{3}\left(\bar{p}\tilde{k} + \mu_{\mathrm{t}}\frac{\partial \tilde{u}_{\mathrm{k}}}{\partial x_{\mathrm{k}}}\right)\delta_{\mathrm{ij}} \tag{3.8}$$

From dimensional analysis, it is known that μ_{t} is proportional to a length scale l and a velocity scale u. Therefore, eddy viscosity models can be distinguished in the way of modelling l and u. This can either be done algebraically or by transport equations. The algebraic approach is used by so called zero-equation turbulence models. These rather simple models are only applicable for simple geometries [55]. Models often used for a wider range of geometries are one- and two-equation models. These models use transport equations to model the transport of μ_{t} [56]. By applying transport equations, the history of the flow field is considered.

An example of a one-equation model is the Spalart Allmaras turbulence model [57]. This model uses one transport equation for an additional property that is derived from the turbulent viscosity. The Spalart Allmaras model works well with aerodynamic shapes.

A common two-equation model is the k-ω shear stress transport (SST) model [58]. This model transports the specific rate of dissipation ω next to the kinematic eddy viscosity k. The k-ω SST model is well known to work better in the boundary layer region and predicts the laminar-turbulent transition much more precisely. It is dependent on the case which model is the best choice.

As described in section 5.1.2 the validation simulations on the NACA 0012 profile showed better agreement with the literature result by using the Spalart Allmaras model. For the propeller profile, with detachments of the airflow, previously studies showed more accurate results using the k-ω SST model according to [59].

3.1.3 DROP3D

After modeling the flow field, to calculate the droplet trajectories a multi-phase simulation is required. The module DROP3D of FENSAP-ICE is used for that. DROP3D is capable of predicting the impingement data on the surface for calculating the ice accretion [60]. The multi-phase flow can be distinguished by the internal structure. In a dispersed multi-phase flow a finite amount of particles are distributed in a continuous phase, like droplets in a cloud. Whereas in a stratified multi-phase flow an interface separates the two phases, like an interface between the surface water film and the free flow.

The module uses an Eulerian two-fluid model based on the Euler equations. The phases are considered as continuum respectively that are characterized by their mass fraction in each volume element. By calculating the motion of each phase using the equation of mass and momentum and considering assumptions for the transfer of mass, momentum and energy enables the calculation of physical properties separately for each phase. The model was introduced by Bourgault et al. [61] and can be described by the following equations:

$$\frac{\partial \alpha}{\partial t} + \nabla \cdot (\alpha u_{\mathrm{d}}) = 0 \tag{3.9}$$

$$\frac{\partial u_{\mathrm{d}}}{\partial t} + u_{\mathrm{d}} \cdot \nabla u_{\mathrm{d}} = \frac{cd_{\mathrm{d}} Re_{\mathrm{d}}}{24K}(u_{\mathrm{a}} - u_{\mathrm{d}}) + \left(1 - \frac{\rho}{\rho_{\mathrm{wat}}}\right)\frac{1}{Fr^2} g \tag{3.10}$$

The velocity of air and velocity of droplet are described by u_{a} and u_{d}. α describes the water volume fraction and K a droplet inertia parameter [44]. The droplets drag coefficient cd_{d} is defined by using an empirical relation and this model is valid for applications of the droplet Reynolds number $Re_{\mathrm{d}} < 500$. The Froude number Fr expresses the ratio of inertia to gravity field described by equation (3.11) with l as the characteristic length and g describing the gravity acceleration. In this approach, it is assumed that the droplets with the water density ρ_{w} are spherical and the size of the droplets is uniform according to the median volume diameter [62].

$$Fr = \frac{u}{\sqrt{gl}} \tag{3.11}$$

3.1.4 ICE3D

The next step is to calculate the ice accretion over a specific time range on the surface of the model. The FENSAP-ICE module ICE3D uses the Messinger model [63]. This model is based on the conservation of mass and energy. Starting with the fluid film as crucial part of the calculations, the phenomena of impingement, evaporation, ice accretion and runback are shown in Figure 3.2.

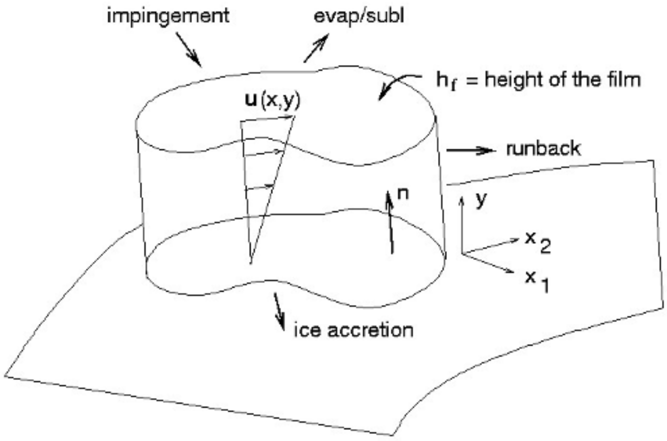

Figure 3.2: Illustration of modelling heat and mass transfer during ice accretion [44]

The velocity of the water film u_{f} as a function of x parallel to the surface and y perpendicular can be calculated as follows:

$$u_{\mathrm{f}}(x,y) = \frac{y}{\mu_{\mathrm{w}}}\tau_{\mathrm{wall}}(x,y) \tag{3.12}$$

According to experimental investigations and assuming a thin water film of less than 10 µm a linear distribution of the velocity is justified starting off at the wall with a velocity of zero due to the no-slip condition [64]. τ_{wall} describes the shear stress of air and μ_{w} the dynamic viscosity of water at the wall. By integrating equation (3.12) over the film thickness h_{f} the average velocity can be described as:

$$\bar{u}_{\mathrm{f}}(x,y) = \int_0^{h_{\mathrm{f}}} \frac{y}{\mu_{\mathrm{w}}}\tau_{\mathrm{wall}}(x,y)dy = \frac{h_{\mathrm{f}}}{2\mu_{\mathrm{w}}}\tau_{\mathrm{wall}}(x,y) \tag{3.13}$$

Furthermore, considering the equations above a set of partial differential equations can be found.

$$\rho_{\mathrm{w}}\left[\frac{\partial h_{\mathrm{f}}}{\partial t} + \nabla(\bar{u}_{\mathrm{f}}h_{\mathrm{f}})\right] = u_\infty LWC\beta - \dot{m}_{\mathrm{evap}} - \dot{m}_{\mathrm{ice}} \tag{3.14}$$

$$\begin{aligned}\rho_{\mathrm{w}}\left[\frac{\partial h_{\mathrm{f}}C_{\mathrm{w}}\tilde{T}}{\partial \mathrm{t}} + \nabla\left(\bar{u}_{\mathrm{f}}h_{\mathrm{f}}C_{\mathrm{w}}\tilde{T}\right)\right] &= \left[C_{\mathrm{w}}\tilde{T}_{\mathrm{d},\infty} + \frac{\|u_{\mathrm{d}}\|^2}{2}\right]u_\infty LWC\beta \\ -0.5\left(L_{\mathrm{evap}} + L_{\mathrm{subl}}\right)\dot{m}_{\mathrm{evap}} &+ \left(L_{\mathrm{fusion}} + C_{\mathrm{ice}}\tilde{T}\right)\dot{m}_{\mathrm{ice}} + \varepsilon\delta(T_\infty^4 - T^4) + \dot{Q}_{\mathrm{h}}\end{aligned} \tag{3.15}$$

Equation (3.14) is the conservation of mass considering on the right side the water impingement as source and evaporation and ice accretion as sink. Equation (3.15) is the conservation of energy and considers on the right side the heat transfer due to impingement of supercooled droplets, evaporation of water, the sublimation of ice and the convective and radiative heat transfer separately.

In addition, the module ICE3D is able to calculate the necessary anti-icing heat fluxes for keeping the surface free of ice. Regarding the two scenarios running-wet and fully-evaporative. For the running-wet scenario, the heat fluxes are calculated to keep the surface temperature at 0 °C to prevent the water-film from freezing. Consequently, the water on the surface runs back freezing downstream at colder surface parts creating runback-ice or reenters the airflow again. For the second scenario of fully-evaporative heating the heat fluxes are calculated to force the evaporation of the impinging droplets immediately, resulting in preventing runback ice. This scenario requires much higher heat fluxes than the running-wet case, having consequently a higher impact on the temperature in the structure.

In this thesis, the evolution of runback ice after anti-icing simulations is of special interest. To be able to predict the areas of ice accretion and runback ice correctly, ICE3D uses a model named Beading [65]. Due to heating the surface, the impinging droplets do not freeze immediately. The beading model calculates analytically the ice accretion not only in space but also in time. It assumes that impinging droplets on the surface build growing beads until they reach a definite size to run back and freeze at a cold surface as half-spherical ice. It enables to predict the sand-grain roughness on the surface due to beading [44]. By incorporating the Beading model, it becomes possible to simulate the impact of ice accretion on heat transfer with greater accuracy.

Calculating flow solutions like the heat transfer coefficient (HTC), FENSAP-ICE offers two approaches [44]. The first approach is an isothermal approach, where walls are set to +10 K of the expected stagnation temperature. Due to this temperature difference, heat fluxes are measureable and ICE3D can convert them into HTCs. The second option, recommended for simulations of high speed flow or rotating surfaces like propellers, where the wall recovery temperature cannot be easily related to the free stream reference temperature anymore, a so called Extended Icing Data (EID) model is used. The model uses an iterative system to extract HTC values of adiabatic flow solutions and is therefore used for the propeller simulations within this thesis. Further insights into the functionality of the model are not provided by ANSYS.

3.1.5 C3D – Unsteady Heat Conduction

After all flow- and icing-simulations are done, the internal heat conduction needs to be considered. The module C3D of FENSAP-ICE is able to calculate the heat conduction of solids made of different materials for steady and unsteady cases when heater pads inside the solid turned on or off [44]. The energy equation reads:

$$\rho_\mathrm{s} c \frac{\partial(\Delta T)}{\partial t} = \nabla \cdot [k(T)\nabla(\Delta T)] - \rho_\mathrm{s} \frac{\Delta H}{\Delta T} \tag{3.16}$$

The solid properties encompass the solid density ρ_s, the specific heat capacity c, the conductivity k, and the enthalpy H. The calculation represents an iterative process. Convergence is reached when the temperature difference ΔT is zero [44].

It is required to provide property information (ρ_s, c and H) of each solid material used in the simulation where the enthalpy is correlated to the temperature.

$$T^\mathrm{new} = T^\mathrm{old} + \Delta T \tag{3.17}$$

After setting an initial temperature, C3D iteratively solves equation (3.16) until the new temperature matches the temperature according to the new enthalpy:

$$H^\mathrm{new} = H^\mathrm{old} + \Delta H = H^\mathrm{old} + c\Delta T \tag{3.18}$$

3.1.6 CHT3D – 3D Conjugate Heat Transfer

Finally, all the modules described above are merged into the last module called CHT3D. This module calculates the temperature exchange between the solid solution and flow solution iteratively, considering all effects like convection in fluids, heat conduction through solids, droplet impingement, surface water film flow, water evaporation, change of phase and ice formation [44]. All these effects are considered by calculating the solutions for each domain separately and exchanging the interface boundary conditions. The CHT3D loop can be described as follows [66]:

1. Initialize surface start temperature by the user.
2. Solve the Navier-Stokes Equations in the fluid domain using FENSAP as described in 3.1.1 with Dirichlet boundary conditions (3.19) at the fluid-solid interface.

$$T = T^{\mathrm{k}} \tag{3.19}$$

3. Calculate heat flux from fluid to solid within FENSAP.
4. Use C3D to calculate the solid temperature distribution by equation (3.16) with Neumann boundary conditions at the fluid-solid interface with $\dot{q}_{\mathrm{sol}}$ describing the conduction heat flux from the wall, k_{sol} the solid conductivity and n as the direction normal to the wall.

$$\frac{\partial T}{\partial n} = -\frac{\dot{q}_{\mathrm{sol}}}{k_{\mathrm{sol}}} \tag{3.20}$$

5. Update the interface temperature T_{int} from the conduction solution.
6. Calculate the new Dirichlet boundary condition considering the heat transfer from solid to fluid with a relaxation parameter ω:

$$T^{\mathrm{k+1}} = (1-\omega)T^{\mathrm{k}} + \omega T_{\mathrm{int}} \tag{3.21}$$

7. Restart at point 2.

This loop is repeated until the required convergence is reached depending on a specific problem. CHT3D is able to consider unsteady de-icing simulations and steady state anti-icing simulations. In anti-icing simulations, a distinguishing feature is the continuous activation of heating pads at a consistent power level. Thus, the temperature distribution converges onto a constant value. Especially these anti-icing simulations with the goal of keeping the surface free of ice are of interest in this thesis.

3.2 Geometries and grid generation

In this study, simulations were done for two different geometries. The first CHT-simulations for validating these simulations were done on a NACA 0012 airfoil, since only few studies done on propellers are available. The final results and examinations of temperature distributions were done on the geometry of a 21-inch propeller from Mejzlik [67]. All simulations are performed in 2D and the grids are generated by using the software Pointwise 2022.2.2 [68]. For CHT-simulations, two grids are required. The flow-grid is necessary for simulating the flow field around and at the surface of the airfoil. The second solid-grid provides the internal structure of the airfoil for simulating heat conduction.

The flow-grid is generated as an O-type having a far-field size of 100 times the airfoil chord length to avoid boundary influences. The grid inside this circle is mainly unstructured beside near the surface. Near the surface, the T-Rex function from Pointwise is applied to enhance grid quality and density in critical areas, such as near walls or geometries with high curvature. The T-Rex mesh consists of 600 layers of triangles and squads. At the surface, the initial cell height is 10^{-6} m with a growth rate of 1.2. This lead to a dimensionless wall distance of $y_1^+<1$. This requirement ensures that the mesh is fine enough to accurately simulate the boundary layer, which is crucial for analyzing momentum and heat transfer at the surface. Especially at the leading edge, the flow has a big impact on the airfoil. Therefore, spacing ensures smaller distances of grid points on the surface, which guarantees a more detailed resolution. The grid is typically divided at the interface where the solid-grid terminates on the surface.

The solid-grid is formed by extracting the grid points directly located at the surface from the previously established flow-grid. For generating the internal mesh two methods are used. The basic method uses the pointwise function ‘normal extrusion’ enabling generating layer-by-layer normal to the surface. This method just works for the first two to three rather thin layers right at the surface. For thicker layers at positions of curvature like at the leading edge the layers start to thicken up generating unrealistic layers. To prevent this, the internal boundaries of the layers and structures, especially for the propeller simulations, were generated in the CAD software Siemens NX [69] in advance. Afterwards the generated layers were equipped with grid points to generate meshes in Pointwise.

Finally, both generated meshes are extruded in spanwise direction by one cell because FENSAP-ICE is not able to simulate in 2D.

3.2.1 NACA 0012

The NACA 0012 airfoil, shown in Figure 3.3, describes a symmetrical airfoil often used for validation data. The airfoil data was obtained from a database called airfoil tools [70] with a chord length of 1 m. The airfoil was cut at a chord length of 0.9144 m to generate a blunt trailing edge to avoid numerical issues and the focus is on the leading edge anyways.

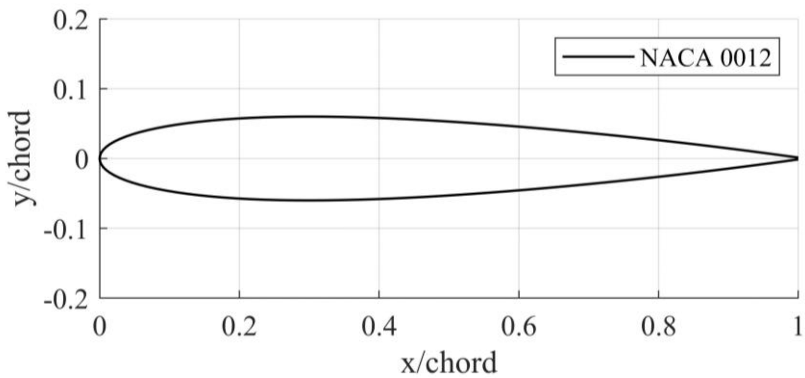

Figure 3.3: Illustration of the symetrical NACA 0012 airfoil

The generated flow-grid is shown in Figure 3.4 and the solid-grid in Figure 3.5. Both grid generations were already explained before in the main chapter 3.2.

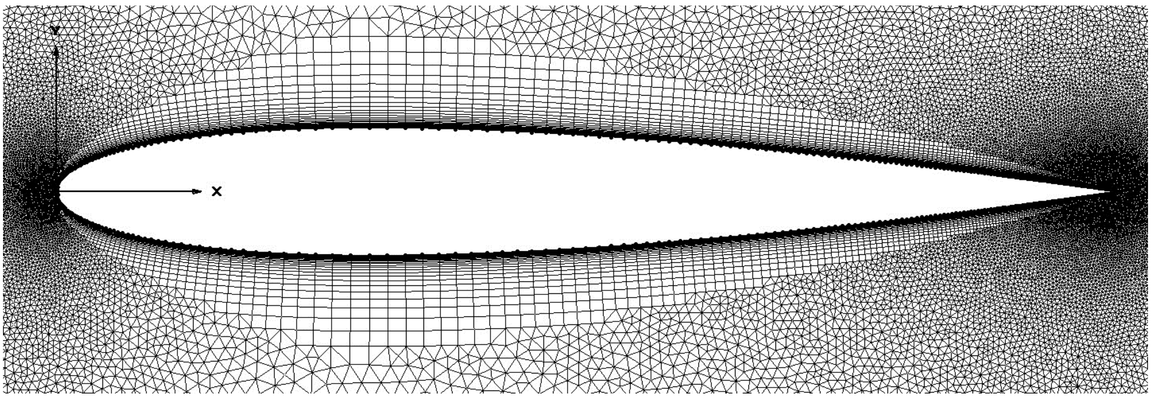

Figure 3.4: Flow-grid of NACA 0012 airfoil

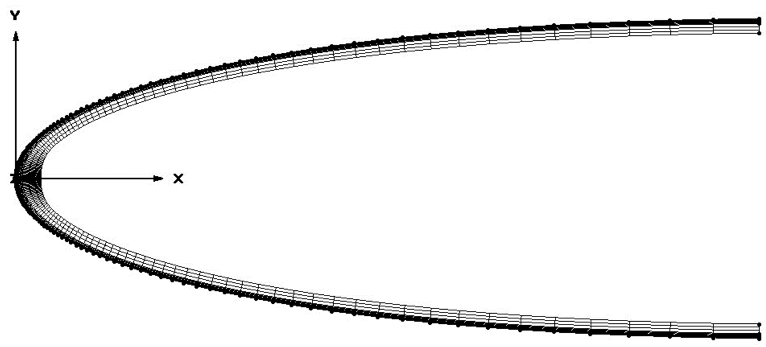

Figure 3.5: Solid-grid of NACA 0012 leading edge

As shown in Figure 3.5 the solid grid is only generated in the leading edge until the same position where the grid of the flow-grid is cut. The solid-grid consists of several layers.

3.2.2 Mejzlik 21x13 inch Propeller

The Mejzlik 21-inch two-blade propeller is mounted on small fixed-wing UAVs, which is considered in this work. This propeller was also used for experimental research within this study described in chapter 4.1. The propeller has a diameter of 21-inch, corresponding to 0.5334 m and a pitch of 13-inch (0.3302 m). Mejzlik provided the 3D CAD propeller data shown in Figure 3.6. For the 2D propeller simulations, three cross-sections of the propeller were created using Siemens NX. The sections were taken at 30%, 50% and 70% of the blade radius accordingly to the thermistor positions during the experimental tests to examine the differences along the propeller radius properly. The chord length of each section was examined geometrically between the two points with the biggest distance. Due to the twist in spanwise direction, each section provided a different pitch angle. The important propeller data and differences between the three sections are shown in Table 3.1.

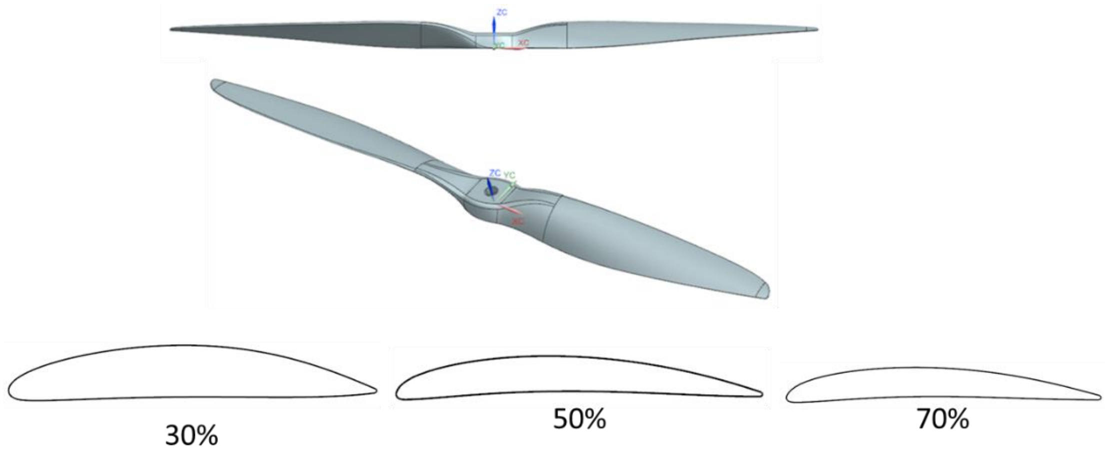

Figure 3.6: 3D model of the Mejzlik 21x13 propeller and the three propeller sections

The generated grids can be seen in Figure 3.7 and Figure 3.8 for the 70% propeller section. As shown, the propeller consists of several internal layers und structures each modelled by a grid.

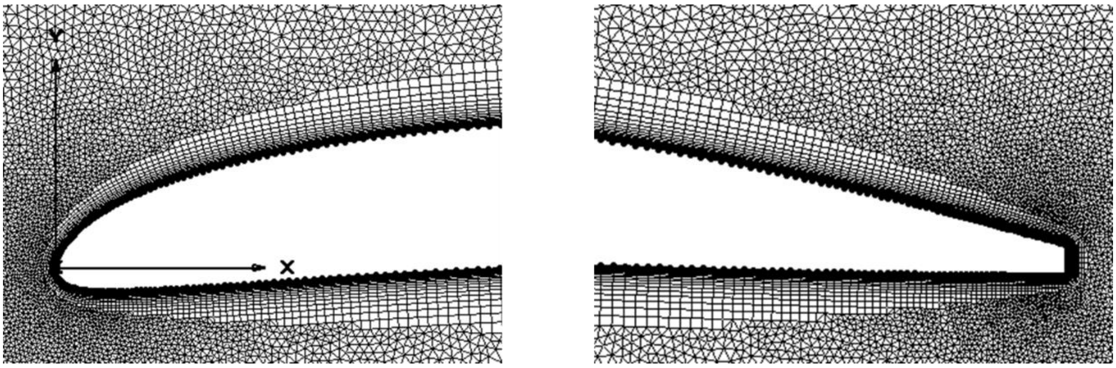

Figure 3.7: Flow-grid at 70% radius cross section of the Mejzlik 21x13 propeller

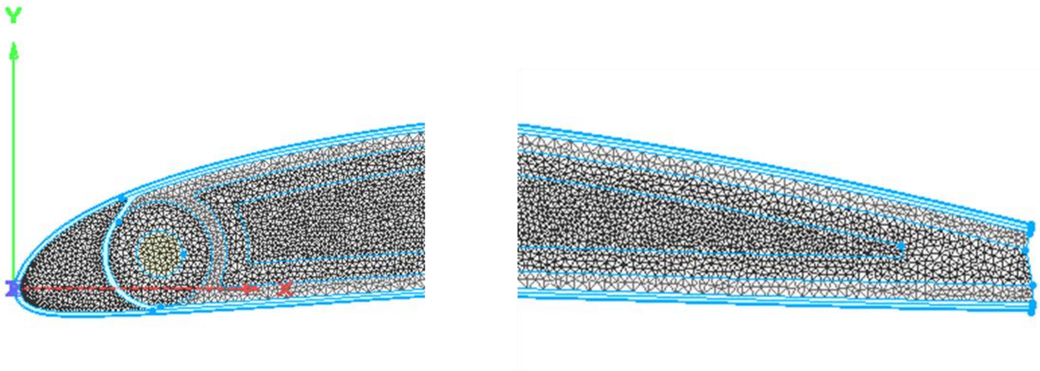

Figure 3.8: Solid-grid at 70% radius cross section of the Mejzlik 21x13 propeller

The grid generation of the propeller grids was done as described above. The dimension of the heating pad in the leading edge was measured photometrical of the experimental propeller, cut at approximately 75% radius. Since the propeller has different thickness between the 30%, 50% and 70% it was assumed that the measured heating pad area and circumference was constant. During the grid generation an accuracy of the heating pad geometry of the solid-grids of around 5% - 10% was reached.

Propeller section	Radial distance [m]	Chord length [m]	Pitch angle [°]
30%	0.0800	0.0407	31.31
50%	0.1334	0.0405	23.38
70%	0.1867	0.0330	17.78

Table 3.1: Propeller data at each propeller section

3.3 Grid dependence study

In CFD simulations, a crucial step is to obtain the optimal mesh resolution. It influences the outcome of critical surface areas, the computational cost and the time for the simulation. Therefore, before doing the final simulations, a grid dependence study is an important step to not only ensure to get correct results but also to reduce computational time. Several aspects need to be considered for the grid generation, such as the spatial resolution and the spacing at critical areas.

In this study, four flow-grids with a refinement ratio of $r = \sqrt{2}$ and three solid-grids are compared in order to find the best possible grid for the applications. For the flow-grids, comparisons were done regarding the aerodynamic parameters of lift- and drag- coefficient and the heat transfer coefficient at the surface of the airfoils. Considering the solid-grids, the surface mesh resolutions of the three least fine flow-grids are used to generate the solid-grids. Evaluation of the solid-grids are done by comparisons of the surface temperature.

To evaluate the differences of the outcomes, several methods are possible. For the aerodynamic values of lift- and drag-coefficient a Richardson extrapolation [71] was used to observe the convergence, while for the other values the Root Mean Square [72] (RMS) approach was applied.

The Richardson extrapolation method is based on a Taylor series and therefore can only be used when the values show a monotonic trend. The approach uses two solutions f_1 and f_2 with different step sizes to calculate a next more accurate value f_0. By iteratively reducing the step size, even more accurate values can be approximated while the step size tends to zero.

$$f_0 \cong f_1 + \frac{f_1 - f_2}{r^{\mathrm{c}} - 1} \tag{3.22}$$

The value c in equation (3.22) describes the order of the error in the numerical method and can be calculated as:

$$c = \frac{ln\left(\frac{f_3 - f_2}{f_2 - f_1}\right)}{ln(r)} \tag{3.23}$$

For the evaluation of the difference in data sets of two grids, the Root Mean Square method is used. It describes a statistical measure to calculate the square root of the average of the squared values and helps to quantify the differences among the solutions of different fine grids.

$$RMS_{\mathrm{fine}}^{\mathrm{coarse}} = \sqrt{\frac{\int_0^{\mathrm{d}} (s_{\mathrm{coarse}} - p_{\mathrm{fine}})^2 dd}{D}} = \sqrt{\frac{\sum_{\mathrm{n=0}}^{\mathrm{i}} (s_{\mathrm{coarse}} - p_{\mathrm{fine}})^2 \Delta d}{D}} \tag{3.24}$$

A complication occurs due to the difference in the number of grid points between the cases. To solve this issue, a linear interpolation was performed. Furthermore, to be able to make a statement regarding the accuracy of the compared values, the RMS is divided by the mean value of the finer grid:

$$NRMS = \frac{RMS_{\mathrm{fine}}^{\mathrm{coarse}}}{\overline{p_{\mathrm{fine}}}} \tag{3.25}$$

$NRMS$ as the normalized Root Mean Square describes the deviation between the values and the mean values of the fine grid.

3.4 Anisotropic heat conduction

Heat can be conducted through a material uniformly or direction dependent. Composite materials show differences in heat conduction dependent on how the fibers are layered. Usually the heat conductivity reaches higher values in fiber direction than normal to it. FENSAP-ICE is not able to take into account anisotropic heat conductivity. Therefore, an analytical approach by Ohmura et al. [73] was applied to calculate an equivalent thermal conductivity k_{equ} and equivalent material lengths $\tilde{x}$ and $\tilde{y}$ based on the hot-wire method.

Considering a 2D anisotropic composite material with the parallel fiber direction x and normal direction y. The heat conduction can be calculated as:

$$\frac{\partial T}{\partial t} = \frac{k_{\mathrm{x}}}{\rho c_{\mathrm{p}}} \frac{\partial^2 T}{\partial x^2} + \frac{k_{\mathrm{y}}}{\rho c_{\mathrm{p}}} \frac{\partial^2 T}{\partial y^2} \tag{3.26}$$

The hot wire method is a method to experimentally examine the thermal conductivity which assumes that heat generated by the wire conducts in a radial direction uniformly. Therefore, the thermal conductivity of an anisotropic material can be calculated by using the thermal conductivity k_{equ}, which describes the equivalent conductivity of an imaginary isotropic material with the same properties.

$$\frac{\partial T}{\partial t} = \frac{k_{\mathrm{equ}}}{\rho c_{\mathrm{p}}} \left(\frac{\partial^2 T}{\partial \tilde{x}^2} + \frac{\partial^2 T}{\partial \tilde{y}^2} \right) \tag{3.27}$$

Equations (3.26) and (3.27) can be transformed with each other in equivalent lengths:

$$\tilde{x} = \sqrt{\frac{k_{\mathrm{equ}}}{k_{\mathrm{x}}}}\, x \text{ and } \tilde{y} = \sqrt{\frac{k_{\mathrm{equ}}}{k_{\mathrm{y}}}}\, y \tag{3.28}$$

Since the total heat, produced by the hot wire, is equal for both cases, the following condition must be satisfied:

$$\int \rho c [T(x, y, t) - T_{\infty}]\, dx dy = \int \rho c [T(\tilde{x}, \tilde{y}, t) - T_{\infty}]\, d\tilde{x} d\tilde{y} \tag{3.29}$$

Applying equations (3.28) to equation (3.29), a relation for the equivalent thermal conductivity can be observed:

$$k_{\mathrm{equ}} = \sqrt{k_{\mathrm{x}} k_{\mathrm{y}}} \tag{3.30}$$

This approach is used for material layers with anisotropic properties applied in this study to gain more realistic results.

3.5 Propeller setup

The propeller setup used in this study was already defined for the experimental tests and was therefore also used for the simulations within this thesis. The propeller was made of different composite materials as shown in Figure 3.9. The material values of the different layers are shown in Table 3.2. The material properties were provided for this study and got previously examined on the basis of literature and online calculators [74], [75], [76] and [77].

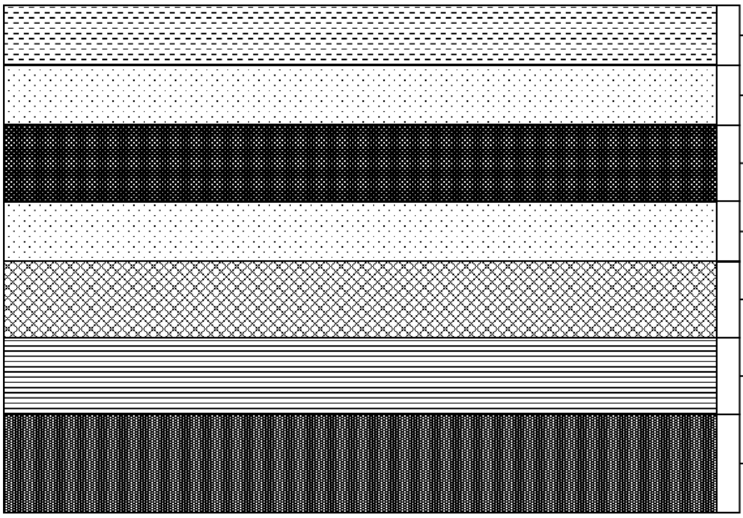

Figure 3.9: Propeller composite layup plan at the leading edge without the wire

The base of the propeller layup was a foam core as inner part with an extremely low density to reduce weight as much as possible but increase inner stability compared to a hollow setup. The first carbon layer on the foam core was a unidirectional carbon/epoxy layer. The fibers were extended in spanwise direction, therefore this layer showed isotropic behaviors in a 2D-section along the chord. Followed by a ±45° carbon/epoxy layer where the carbon fibers are woven at a 90° angle to each other. This structure causes anisotropic material behavior, why equivalent material values for the simulation setups were calculated. The next three layers consist of two identical glass fiber/epoxy layers and the unidirectional carbon heater pad as the ETIPS in between. The glass fiber layers are both isotropic. The heater pad is twisted along the propeller spanwise direction, thus showing thermal conductivity always normal to the fibers in a 2D-section. The outside layer of the propeller setup was an epoxy topcoat with again isotropic behavior in a 2D-section.

	Foam	Uni carbon	±45° carbon	Glass fiber	Uni carbon (ETIPS)	Epoxy topcoat	Cop-per	Silicone
Layer thick-ness [mm]	2	0.38	0.18	0.06	0.7	0.02	0.65	0.85
Equivalent thickness [mm]	-	-	0.26	-	-	-	-	-
Density [kg/m^3]	80	1340	1340	1570	1340	1150	8960	1190
Specific heat [J/(kgK)]	1.25	1065	1065	1000	1065	1110	383	1255
Thermal conductivity normal to fiber [W/(mK)]	0.028	0.35	0.65	0.5	0.8	0.18	370	0.25

Thermal conductivity parallel to fiber [W/(mK)]	-	0.35	2.8	0.5	0.6	0.18	-	-
Equivalent thermal conductivity [W/(mK)]	-	-	1.35	-	-	-	-	-

Table 3.2: Composite material values of the propeller

The wire to power the ETIPS was placed in the leading edge between the glass fiber and ±45° carbon layers as shown in Figure 3.11. Due to the relatively large size of the wire, the influence on thermal conductivity through the propeller cannot be neglected. That is why the wire was considered in the simulations along with the material properties of copper and silicone as can be seen in Table 3.2.

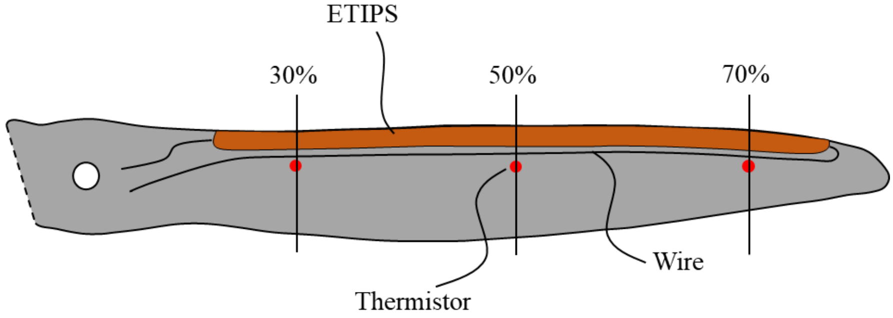

Figure 3.10: Schematic sketch of the ETIPS setup and thermistor positions

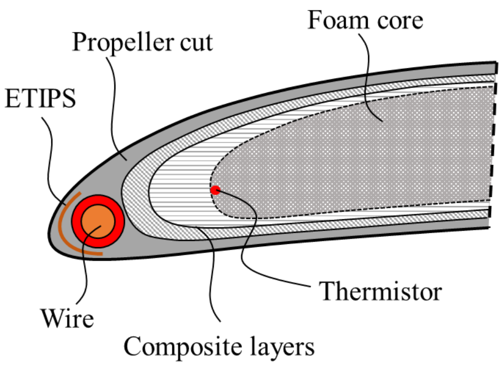

Figure 3.11: Schematic sketch of propeller cut leading edge

Within the propeller setup at three separate locations along the spanwise direction, (30%, 50% and 70%) thermistors were integrated to gain experimental temperature data. The ETIPS in the leading edge of the propeller was extended over 70% - 75% of the propeller diameter as shown in Figure 3.10.

3.6 Validation case for CHT3D simulations

To first validate the CHT3D simulations, a test campaign from Al-Khalil et al. in 1997 was chosen as reference [78–80]. The objective of the conducted work was to validate NASA´s

LEWICE and ANTICE computer codes for thermal ice protection systems. This validation was done based on an experimental test campaign on an NACA 0012 airfoil section. The first part [78] of this campaign focuses on the experimental investigation and procedures, the second part [79] on the de-icing test cases and the third part [80] on the anti-icing cases. The focus in this thesis is mainly on the electro thermal anti-icing, that's why in the following only the results of the anti-icing test cases from [80] are shown.

The experiments were performed at the NASA Lewis Icing Research Wind Tunnel, which is a closed-loop icing wind tunnel. The test section of the NACA 0012 airfoil had a span of 1.830 m and a chord length of 0.914 m separated in a leading-edge section of 0.254 m and a wooden after body of 0.660 m. The leading edge was equipped with an electro-thermal IPS separated in seven heater zones as shown in Figure 3.12. During the test campaign, it was determined that all heater zones were shifted towards the side of heaters C, E and G by 4.8 mm due to mistakes in the manufacturing process.

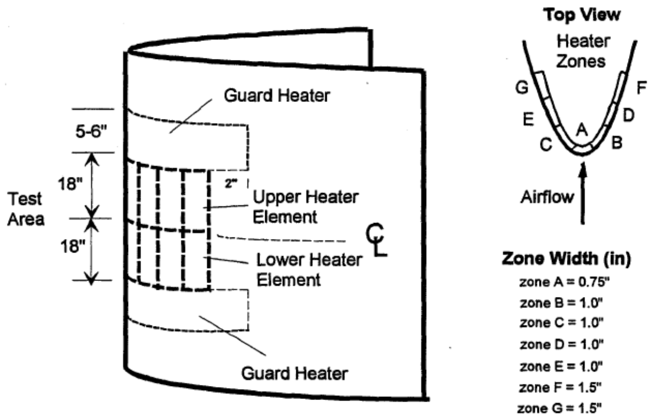

Figure 3.12: Leading edge heater setup of the NACA 0012 airfoil [78]

The leading-edge structure consists of several materials. The exact setup with all material properties and thicknesses can be found in Table 3.3. It shows the most inner material in the first column and the ends with the outer material in the last column.

	Silicone Foam insulation	Fiber Glass/ Epoxy composite	ETIPS, Alloy 90	Elastomer, COX 4300	Erosion shield, SS 301 HH
Layer thickness [m]	$34.3 \cdot 10^{-4}$	$8.9 \cdot 10^{-4}$	$0.13 \cdot 10^{-4}$	$5.59 \cdot 10^{-4}$	$2.03 \cdot 10^{-4}$
Density [kg/m^3]	648.75	1794.07	8906.28	1383.99	8025.27
Specific heat [J/(kgK)]	1130.43	1570.05	385.18	1256.04	502.42
Thermal conductivity [W/(mK)]	0.121	0.294	41	0.256	16.27

Table 3.3: Material properties of leading edge structure [78]

Furthermore, temperature sensors were integrated in the structure, always in a normal to the surface order at different locations. One was placed at the underside of the abrasion shield, one under the heater element and one at underside of the insulation layer.

The test case chosen for the validation of the CHT3D simulations was an anti-icing running wet case with zero angle of attack, meaning the chord line was parallel to the air stream. The exact icing and flow conditions can be found in Table 3.4.

	Air velocity [m/s]	Air temperature [°C]	LWC [g/m^3]	MVD [µm]	AOA [°]	Time [s]
Validation case	44.7	−6.67	0.78	20	0	325

Table 3.4: Flow and icing conditions of the validation case [78]

The test was done for 325 s, all heater zones were powered the whole time as usual for an anti-icing case. The ETIPS were powered with the heat sources shown in Table 3.5.

	Zone A	Zone B	Zone C	Zone D	Zone E	Zone F	Zone G
Heat source [W/m^3]	$3.78{\cdot}10^8$	$3.17{\cdot}10^8$	$2.32{\cdot}10^8$	$2.32{\cdot}10^8$	$2.69{\cdot}10^8$	$2.07{\cdot}10^8$	$1.83{\cdot}10^8$

Table 3.5: Heat source of all heater zones of the validation case [78]

The influence of the shift of the heater zones, to the side of zones C, E and G, can already be observed in the required heater powers. This results in a non-symmetrical distribution of the volumetric power density. The heater zones C and G, require less power as the corresponding heater zones on the other side (B and F).

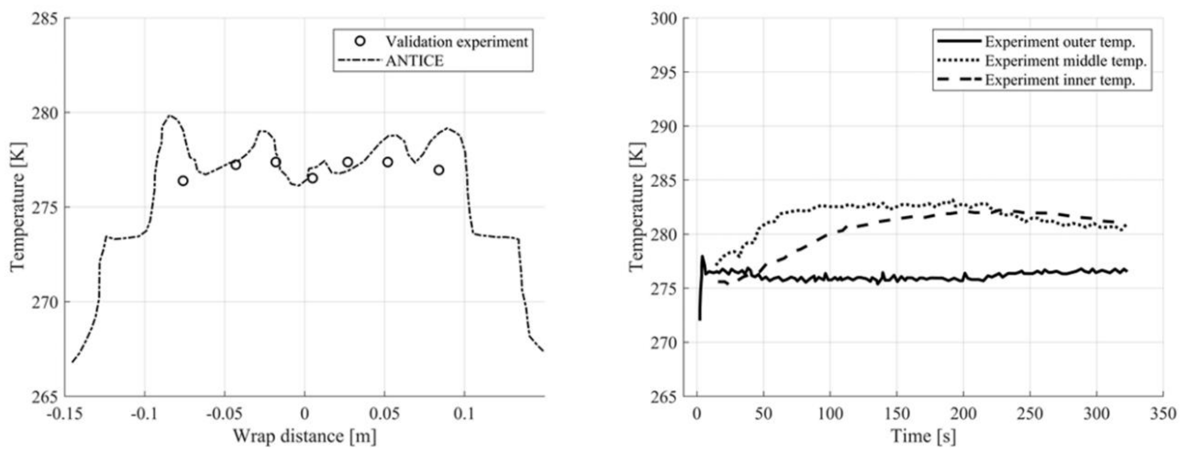

Figure 3.13: Experimental and numerical obtained results for validation [78], [80]

The validation test compared the CHT3D simulations with the actual surface temperature and temperature development over time at three specific locations inside the structure, as depicted in Figure 3.13. The results and comparisons of the CHT3D simulations with the literature are shown in 5.1.

3.7 Flow conditions on propellers

The airflow around a propeller is quite complex due to many different velocity components acting on the propeller. In addition to the natural inflow by the moving aircraft, the rotation of the propeller has a big influence on the inflow. The simulations in this thesis are done in

2D and therefore rotation cannot be directly simulated as in a 3D case. For each 2D section, the inflow velocity and angle must be calculated previously considering different aspects. The blade element theory was used [81] which calculates the aerodynamic forces on the blade assuming that each blade section acts as a 2D airfoil with the sum of all sections describing the whole propeller. This theory neglects stall- and compressibility effects to get an analytical solution.

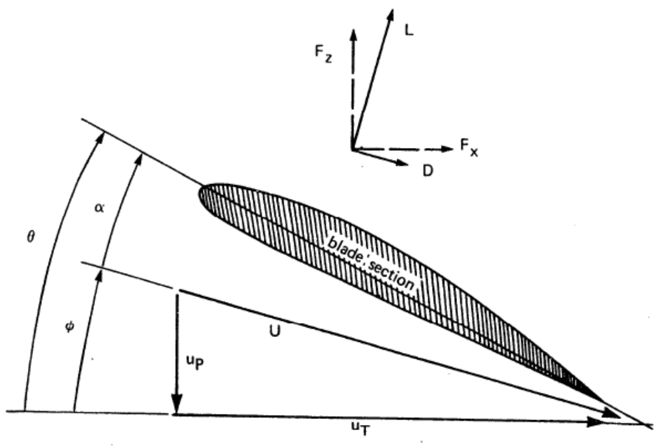

Figure 3.14: Aerodynamics of a proepller blade section [81]

The airflow around a propeller consists of three components. The surrounding air velocity u_a due to wind or the aircraft movement describes the first part. The second part is due to the rotation of the propeller and is illustrated as u_T in Figure 3.14. The last part describes the induced flow u_i which appears due to the forward movement of the air by the thrust generated by the propeller and can be calculated using the momentum theory [81]:

$$u_\mathrm{i} = 1.15\sqrt{\frac{Tr}{2\rho A}} \tag{3.31}$$

Equation (3.31) is a simplified calculation of the induced flow with a correction value of 1.15. With Tr describing the produced thrust by the propeller, the air density ρ and the propeller plane area A that can be calculated by the propeller radius r as:

$$A = \pi r^2 \tag{3.32}$$

The induced flow therefore counteracts the inflow of the surrounding air, thus u_p is composed of u_a and u_i as follows:

$$u_\mathrm{p} = \frac{u_\mathrm{a}}{2} + \sqrt{\left(\frac{u_\mathrm{a}}{2}\right)^2 + u_\mathrm{i}^2} \tag{3.33}$$

The airflow u_T is dependent on the distance of the section from the propeller hub. The further out the section of the propeller is, the faster is the relative spin velocity and the higher is the rotational airflow. This can be calculated by the radial distance d_r and the rotation rate of the propeller Ω:

$$u_\mathrm{T} = \Omega d_\mathrm{r} \tag{3.34}$$

Finally resulting in the propeller section inflow as:

$$U = \sqrt{u_\mathrm{p}^2 + u_\mathrm{T}^2} \tag{3.35}$$

Under consideration of the pitch angle θ and the apparent angle $\phi = \arctan\left(\frac{u_\mathrm{p}}{u_\mathrm{T}}\right)$, the angle of attack α can be calculated by the difference of θ and ϕ. All the above-described steps lead to the results of the air inflow velocity and the corresponding angle with which the propeller section is flowed towards.

	Air velocity [m/s]	Density [kg/m^3]	Rotation rate [RPM]	Thrust [N]	Area [m^2]
Propeller	25	1.2041	4200	12	0.2235

Table 3.6: Constant values for calculating the propeller flow conditions

All experimental and numerical inquiries of the 21-inch propeller described in section 3.2.2 were done at constant values of air density, inflow velocity and rotation rate. These values are shown in Table 3.6. The thrust was measured during the VTT experiments in dry conditions without any degradations due to ice accretion. Using Table 3.1 and Table 3.6 with the equations (3.31) - (3.35), the final flow properties for each propeller sections can be calculated as shown in Table 3.7.

Propeller sections	Inflow velocity [m/s]	Angle of attack [°]
30%	43.830	−5.282
50%	64.207	−0.635
70%	86.168	0.128

Table 3.7: Propeller data at each propeller section

It can be observed that as the radial distances decrease, the relative inflow velocity decreases due to the ratio between the constant air velocity and the increasing rotational speed across the span. Consequently, the angle of attack changes over the span and may even become negative. A phenomenon of a propeller, resulting in the fact that the produced thrust of the propeller depends on all relative velocities, even the flight velocity of the aircraft, and is not constant along the propeller blade. The focus in this thesis is not on the propeller calculations, therefore such assumptions are considered as acceptable trade-offs with the accuracy of the results in a sufficient frame.

4 Experimental investigation of inflight icing on propellers

4.1 VTT – icing wind tunnel tests

An experimental test campaign was performed in order to obtain data for validating the numerical results. The tests were done at the VTT Technical Research Centre in Helsinki, Finland [82]. The icing wind tunnel there has an open loop design with a square test section of 70 cm in edge length. Wind speeds of up to 50 m/s with icing conditions of −25 °C can be reached.

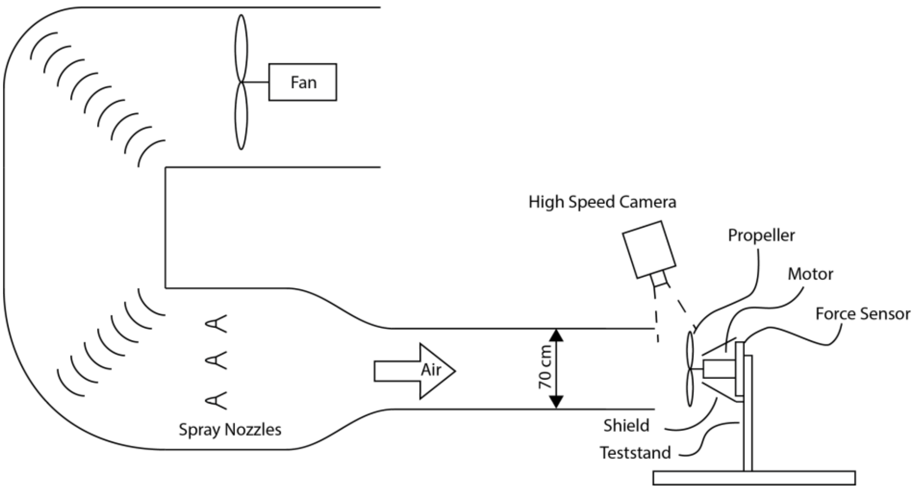

Figure 4.1: Test setup at the VTT - icing wind tunnel [36]

As shown in Figure 4.1, the propeller test stand consists of multiple sensors. The dynamometer “Flight Stand 15” from Tyto Robotics [83] was equipped with an internal torque- and thrust- meter that sends commands directly to the electronic speed controller [84]. An infrared sensor and reflector were used to measure the rotation of the propeller driven by a Hacker Q80-9M motor [85]. A custom-made shield to protect everything from ice accretion and shedding covered all sensible components behind the propeller. The rotation rate was kept constant at 4200 RPM equals 40 Hz using a python code. To power the ETIPS a slip ring [86] was used which was controlled via a control board and pulsed width modulation.

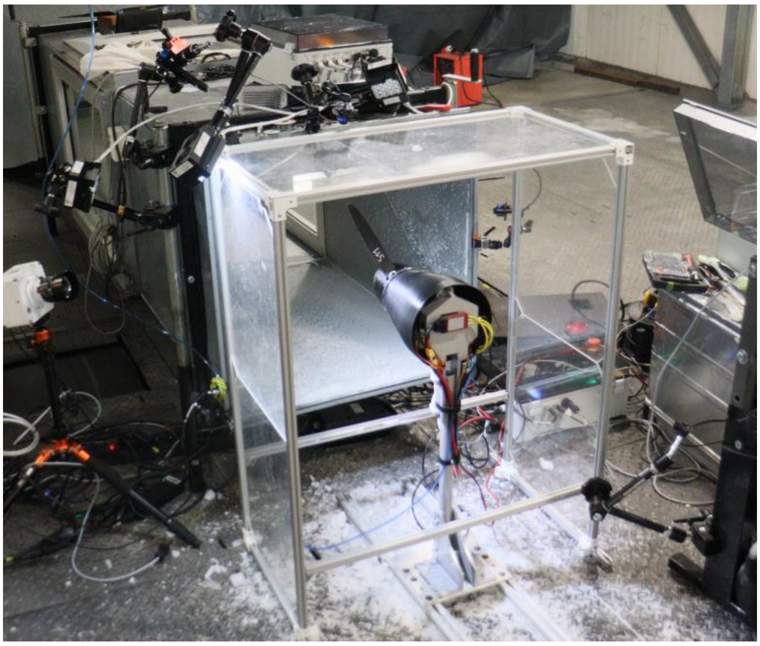

Figure 4.2: Image of propeller stand test setup at VTT

At the beginning of the test campaign, the liquid water content is calibrated with the method of a rotating cylinder. For the test campaign, two propellers were manufactured and equipped as described in section 3.5. Experiments were done at two temperatures and different icing conditions but with the same air velocity of 25 m/s and constant propeller rotation rate of 4200 RPM. The test cases used for the validation process in this thesis is shown in Table 4.1.

Test Case	Temperature [°C]	Air velocity [m/s]	LWC [g/m^3]	MVD [µm]	ETIPS power [W]	Run time [s]
#1	−5	25	0.44	20	70	120
#2	−5	25	0	-	50→130 (40 per 60 s)	180
#3	−10	25	0.44	20	230	120

Table 4.1: Test cases of the experimental test campaign

While test cases #1 and #3 are on wet-conditions, with constant ETIPS power but different temperatures, test case #2 is on dry-conditions with increasing power of 40 W every minute. The idea behind the dry- and wet- conditions is the examination of the differences when only forced convection (#2) on the surface happens without the influence of effects like water impingement, evaporation cooling and latent heat. The results of this investigation can be found in section 5.2.2. During the experimental tests, the maximum ETIPS power was found iteratively. Every run the power was increased gradually to not overheat the internal propeller structure. As indicator, the measured temperature of the thermistors was kept below 60 °C, except for the dry run since this one was done at the end of the test campaign.

4.2 Experimental uncertainties

Regardless of the topic, every scientific measurement inherently involves a degree of uncertainty that can lead to differences when comparing the data to numerical results. Further, uncertainties affect numerical simulations as well as described later. Inaccuracies already start in the manufacturing process, considering minor variations in material composition and dimensions, position of sensors or even ambient conditions during production. Two of the same propellers are never identical. Furthermore, regarding experimental tests in an icing wind tunnel, variations occur in the flow and icing conditions as well as changes in the humidity over several runs in the test chamber. A small amount of ice accretion on the spray nozzles or on tunnel walls can lead to LWC variations over the propeller area and influence flow characteristics. Every measuring instrument has limited accuracy due to calibration drifts or sensor sensitivities. The thermistor for example has a resistance tolerance of 1% [87]. In first estimations, this would result in a temperature tolerance of ±1 K. As can be seen the list of uncertainties during experiments is quite long and every uncertainty has a varying degree of influence. Nevertheless, the following processes were done to keep the quality of the results as high as possible. The flow rate through the nozzles were monitored to detect blocked nozzles. The measuring instruments were calibrated before every run. After every run with ice accretion, the propeller was cleaned with isopropanol to remove every bit of water from the surface. To minimize the influence of uncertainties runs were repeated.

Considering manufacturing uncertainties, previous destructive testing of samples were performed to ensure acceptable variations between the propellers. Further dealing with uncertainties like thermistor positions are described later.

5 Validation of numerical simulations

5.1 Validation of CHT-simulations

One of the most important steps in a numerical study is to validate the simulation results. Therefore, among the limited existing work on CHT-simulations involving anti-icing and obtaining sufficient information for setting up the simulations correctly, the study conducted by Al-Khalil et al. [78–80] was selected as a reference. It consists of three parts, with the first part [78] describing the experimental setup, the second part [79] focusing on de-icing results and the third part [80] showing the anti-icing investigations. The study results and experimental setup is described in 3.6.

5.1.1 Grid- and time- dependence study

Before performing the simulations, a grid dependency study was done to find the most suitable case to get results as accurate as possible but keep the computational effort as low as possible. For this study, four flow-grids and three solid-grids were inspected as described in 3.2.1. The setup of the four different flow-grids is shown in Table 5.1. The refinement ratio was chosen to be $\sqrt{2}$. After the flow simulations, solid-grids of the Coarse-, Medium- and Fine-flow-grids were generated. The CHT-simulations are computationally intensive and due to limited resources, it was decided to restrict on three grids.

	Coarse	Medium	Fine	xFine
Points on lower and upper side	180	255	360	510
Leading edge spacing [mm]	0.60	0.40	0.30	0.20
Trailing edge spacing [mm]	0.50	0.30	0.25	0.15
Points on far field	200	283	400	566

Table 5.1: Flow-grid features of the NACA 0012 airfoil

The solid-grids were all generated in the same way on the basis of their flow-grids and it was chosen that an amount of grid points for each layer normal to the surface of four was sufficient. The flow-grid is much more sensitive in the aspect of resolution especially in the boundary layer and at the leading edge. The flow-simulations were set up according to Table 3.4 and the CHT-simulations considering the material properties of Table 3.3 with all heaters were powered with the same volumetric heater power density of $4{\cdot}10^8$ W/m^3. The CHT-simulations were done with a time step of 10 s and 10 iterations. In addition, the influence of the time steps was examined by reducing the time steps to 5 s and 2 s. The grids were analyzed under the aerodynamic parameter drag-coefficient C_d, the heat transfer coefficient h and the surface temperature.

All plots in this thesis that show values along the surface are plotted against the wrap distance. The wrap distance shows the distance along the surface from the leading edge with positive values along the upper surface and negative values along the lower surface. The results of the C_d analysis shown in Figure 5.1 show an asymptotic trend that enables the calculation of a Richardson extrapolation. All meshes show just a relatively small deviation with the biggest deviation between the coarse mesh and the xFine mesh of $1.75 \cdot 10^{-4}$. The difference in the HTC, which is also comparably small, shows again the biggest deviation between the Coarse and the xFine mesh. The difference between the medium and fine mesh compared to the xFine mesh show just small deviations, with the biggest difference at the wrap distance 0.021 m where the flow seems to change its characteristics from a laminar to a turbulent one. The relative differences expressed in the NRMS show the smallest deviation between the xFine and the Fine mesh with 0.25% followed by the Medium mesh with 0.91% and 2.56% for the Coarse mesh.

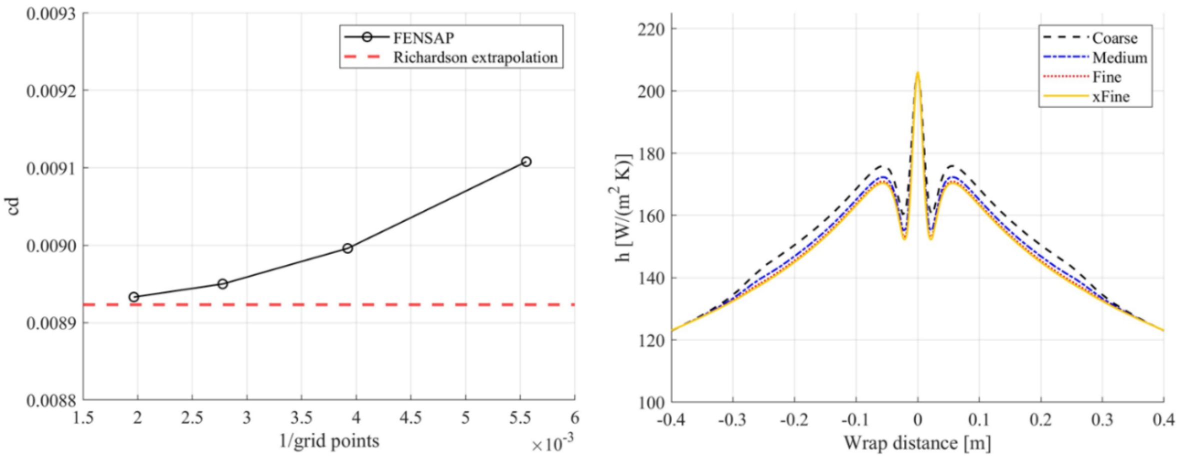

Figure 5.1: Grid dependence in cd and heat transfer coefficient

Regarding the surface temperature in Figure 5.2 the influence of the HTC becomes visible and shows again almost similar results for the Medium and Fine mesh with a relative difference NRMS of 0.19% and a NRMS between the Coarse and Fine mesh of 0.29% which is also comparably low.

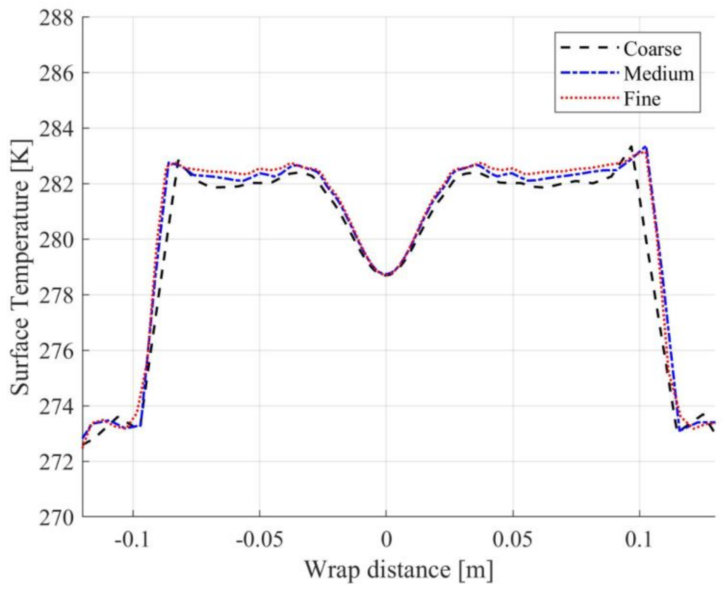

Figure 5.2: Grid dependence in surface temperature

Regarding all above shown results, even the Coarse mesh shows good results with only small deviations compared to the Fine and xFine grid. Nevertheless, to capture all effects along the leading edge surface like the laminar-turbulent transition with an impact on the HTC and surface temperature in an acceptable range it was decided to use the Medium grid for the final validation simulations.

The influence of the time discretization within the CHT-simulations is visualized in Figure 5.3 and shows the largest differences especially at the beginning of the simulations. In the first seconds of the simulations where the heater turn on, the change in temperature is the biggest. Although all three simulations have the initial temperature of 266.5 K, the first data point is calculated according to their time discretization. Which means for the 2 s case after two seconds, for the 5 s case after 5 seconds and for the 10 s case after 10 seconds. The shorter the time between calculating the gradients, the more accurately the temperature development can be mapped at the beginning. Time steps of less than a second are necessary to avoid the unphysical overshooting temperature at the beginning.

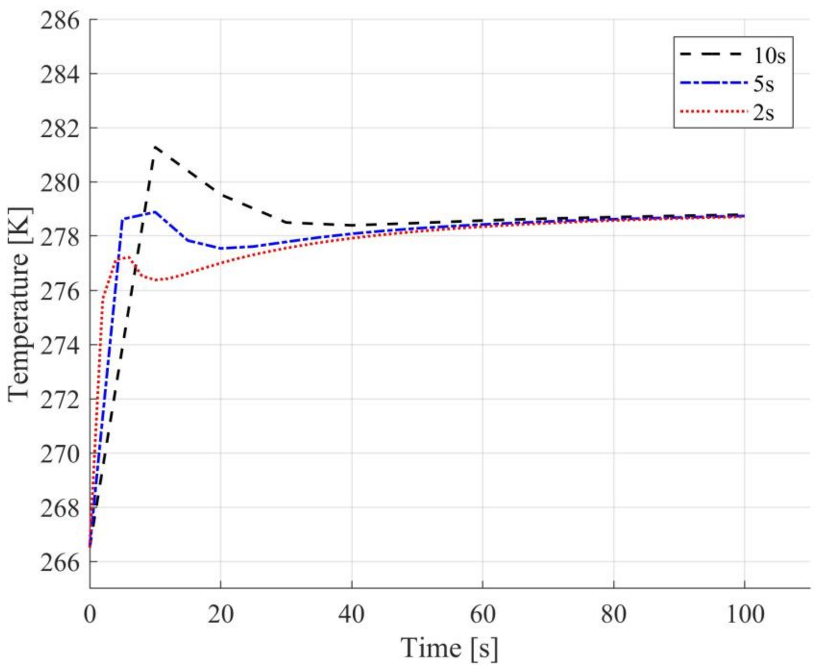

Figure 5.3: Influence of time steps in CHT-simulations

Nevertheless, all three simulations converge to the same temperature after 100 s. Since anti-icing simulations are steady state cases where one final value is reached after an amount of time, this final value is the most interesting one in most cases. The impact of smaller time steps is the increasing number of iterations necessary to reach convergence. Therefore, the optimal balance between accuracy and computational effort was found to be at time steps of 2 s - 3 s.

5.1.2 Comparison with experiments from the literature

After the grid for the simulations has been chosen, the simulations for the validation have been performed. As shown in 3.6 the results are compared to the surface temperature and the temperature development within the structure at the leading edge over time. The flow and icing conditions of the test case can be found in Table 3.4. The numerical setup of the validation simulations is shown in Table 5.2.

FENSAP	
Turbulence model Surface roughness BC wall parameters Artificial viscosity	Spalart Allmaras No roughness Temperature - stagnation temperature + 10 Streamline upwind + cross wind dissipation 1e-7
DROP3D	
Physical model Distribution Water density	Droplets Monodisperse 1000 kg/m^3
ICE3D	
Ice – Water model Beading Roughness output	Glaze - Advanced Activated Sand-grain from beading
C3D	
Material definition BC – walls BC – interface Cycles	Table 3.3 Heat Flux: 0 W/m^2 Nothing Table 3.5

Table 5.2: Numerical parameter setup for the validation CHT-simulations

During the experimental study by Al-Khalil et al. [78,80] it was observed, that the predicted transition from laminar to turbulent flow for the wet cases do not correspond to the experimental observations. This was due to beads and rivulets on the leading edge that forced the transition of the flow, which consequently shows differences in the heat transfer coefficient. During the FENSAP-ICE simulations it was found that the assumption of a fully turbulent flow with the Spalart Allmaras model showed the best results compared to the literature and was therefore used for the validation. This assumption was also be done by Carozza et al. [88] who's predicted HTC is in good agreement with the one calculated by FENSAP-ICE. Especially the common laminar zone fits well to the experimental values on dry conditions when no water on the surface disturbs the flow. The transition location is in well agreement with Carozza et al. [88], while HTC values more downstream match the values predicted by Bu et al. [89] and Iuliano and Ferraiuolo [90]. The faster decrease of the HTC in the laminar region compared to the slower decrease in the turbulent region is evident after the transition at approximately 0.02 m. While in the laminar flow the stratified distribution leads to a less efficient heat transfer normal to the surface, the well-mixed turbulent flow transfers the heat better away from the surface.

Apparently, directly at the leading edge (wrap distance 0 m) the differences between FENSAP-ICE and the experiments are maximal. This might be due to not fine enough spacing at the leading edge during the grid generation. Nevertheless, the grid was not changed any more, since a decreased spacing at the leading edge would have led to a less fine resolution along the surface when keeping the amount of grid points constant and the computational cost acceptable.

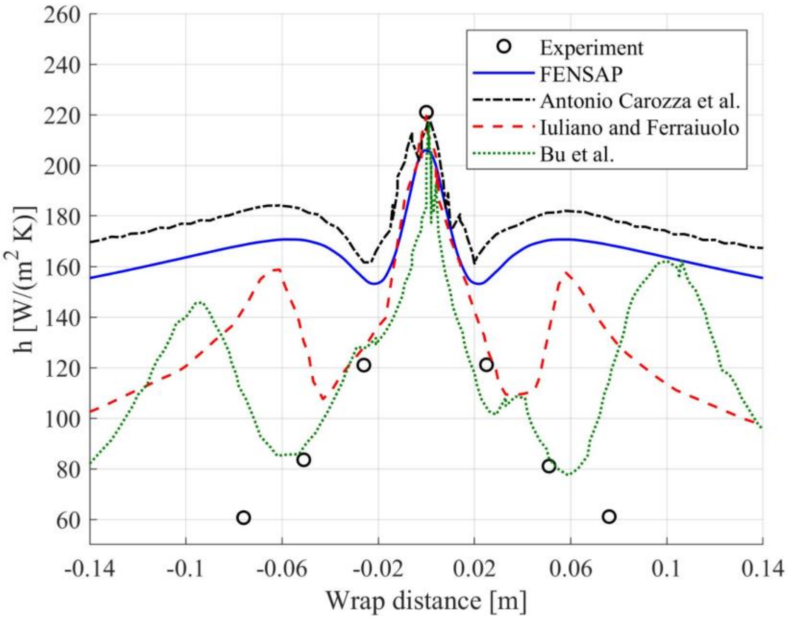

Figure 5.4: Comparison of the heat transfer coefficient to values from the literature

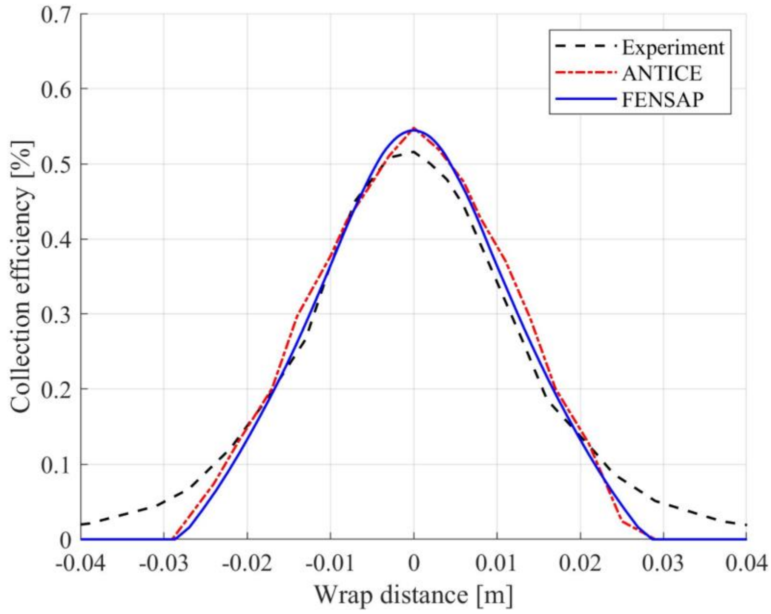

Figure 5.5: Comparison of the collection efficiency with experimental and numerical values from the literature

Figure 5.5 show the comparison of the collection efficiency at the leading edge. The collection efficiency describes how efficient droplets are collected at surface positions. Numerical predictions have also be conducted [80] and show similar results as FENSAP-ICE. Overall, the differences between the numerical and experimental results are small. This leads to the results of the CHT-simulations as shown in Figure 5.6.

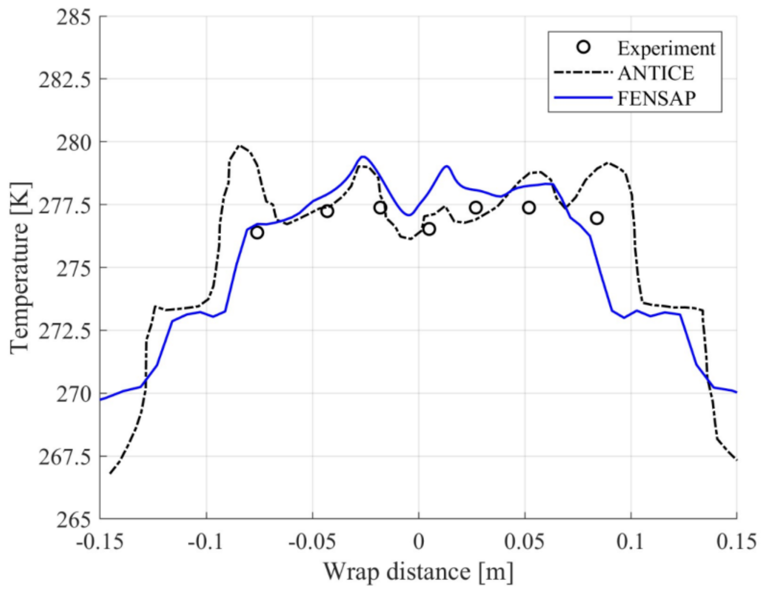

Figure 5.6: Comparison of the surface temperature with results from the literature

The results in Figure 5.6 are in good agreement with the experimental values. This might confirm the choice of the turbulent model and the predicted transition. The biggest differences can be observed at the leading edge, which corresponds to the lower maximal HTC compared to the experiments.

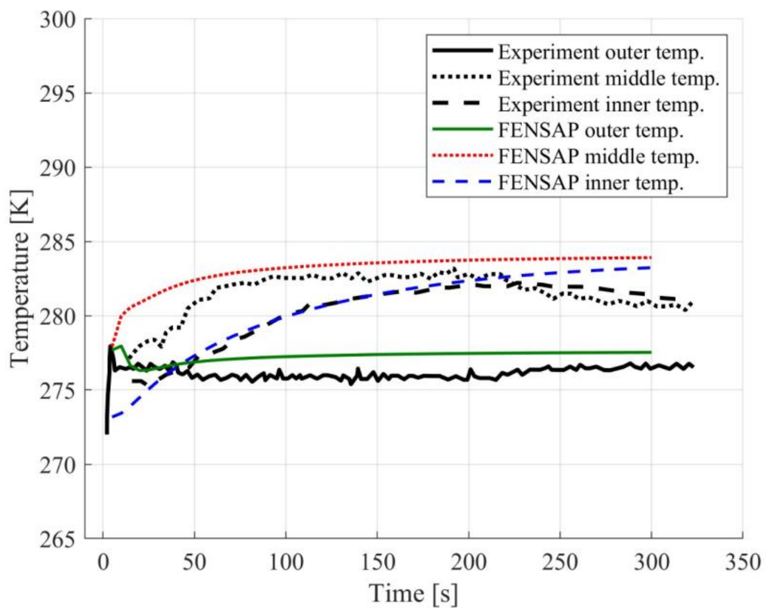

Figure 5.7: Comparison of temperatures in the structure over time with results from the literature

The temperature development over time is in good agreement with the measured values as well. The biggest differences can be seen within the first 20 s. The initially set temperature or rather rough time stepping might cause this. Nevertheless, the inner temperature matches the values between 75 s and 200 s exactly, which indicates that the heat conduction over time must be similar and with it the material properties and heater powers are chosen correctly. In addition, the drop of the experimental examined temperature in the last 100 s for the middle and inner temperature is not captured. At the same time, the outer temperature experiences a slight rise. This must be due to changes in the test, like changes in the power supply or a measurement error, since anti-icing is a stationary case, where such changes cannot happen naturally.

Experimental data are always influenced by many more effects than numerical simulations can capture but are therefore affected by uncertainties such as measurement errors, initial settings, sensor positions or manufacturing mistakes, just to name a few. Nevertheless, the numerical data obtained with FENSAP are in good agreement to the experimental tests by Al-Khalil et al. [78–80]. In summary, the validation process of the numerical simulations confirmed the accuracy and reliability of the model. It demonstrates great alignment with experimental data and underlines the accuracy of the numerical tools.

5.2 Validation of 2D CHT - propeller simulations

5.2.1 Grid dependence study

As previously done for the NACA 0012 airfoil, a grid dependence study is required for the propeller validation to ensure reliable results independent of the grid. Although three different propeller sections are considered within this thesis, it was decided to focus on the 70% section for the grid dependence study. The rotation of the propeller results in the 70% section being exposed to the highest relative velocity among all three sections, making aerodynamic and thermodynamic phenomena more sensible to grid resolution.

As before, four flow-grids and three solid-grids out of the Coarse-, Medium- and Fine- flow-grids were generated and compared. The grid parameters are presented in Table 5.3. The refinement ratio was again $\sqrt{2}$. The flow simulations were set up according to Table 3.6 and Table 3.7 at −5 °C with an LWC of 0.44 g/m^3. The material values for the CHT-simulation can be found in Table 3.2 and the ETIPS was powered with a heat source of $7 \cdot 10^7$ W/m^3.

	Coarse	Medium	Fine	xFine
Points on lower and upper side	280	400	560	790
Leading edge spacing [mm]	$7 \cdot 10^{-5}$	$5 \cdot 10^{-5}$	$3.5 \cdot 10^{-5}$	$2.4 \cdot 10^{-5}$
Trailing edge spacing [mm]	$7 \cdot 10^{-5}$	$5 \cdot 10^{-5}$	$3.5 \cdot 10^{-5}$	$2.4 \cdot 10^{-5}$
Points on far field	280	400	560	790

Table 5.3: Flow-grid features of the propeller grids

As shown in Figure 5.8 the lift coefficient C_L do not follow a clear trend along the amount of grid points. Especially the xFine grid shows a value out of the trend and reaches a value between the values of the Coarse- and Medium-grid. Nevertheless, all values are in a rather small range with the value of the Medium grid between the values of the Fine- and xFine-grids.

	NRMS
Coarse	8.55%
Medium	3.47%
Fine	2.68%

Table 5.4: NRMS values for the HTC comparison

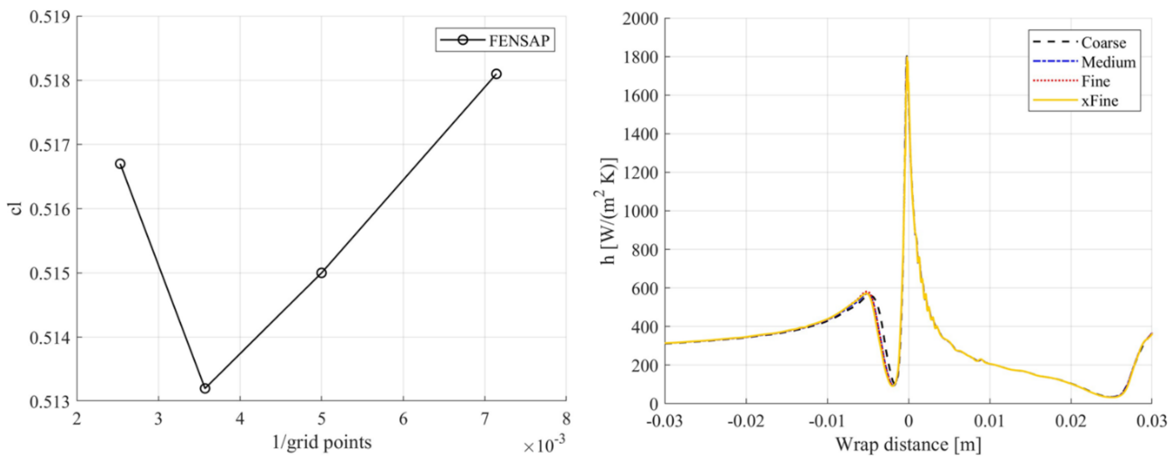

Figure 5.8: Grid dependence in cl and HTC of propeller 70% section

Comparing the HTC values along the propeller surface, all grids show a similar contour. The biggest visible deviation occurs for the Coarse gird compared to the others between the wrap distance of −0.002 m and −0.012 m. It seems that all grids are able to resolve the critical stagnation point at the leading edge. Even the maximum values vary in only 5 W/(m^{2}K) between all grids. The observations of just small differences are confirmed by analyzing the mean differences (NRMS) always referred to the xFine grid as shown in Table 5.4.

	NRMS
Coarse	0.200%
Medium	0.046%

Table 5.5: NRMS values for the surface temperature comparison

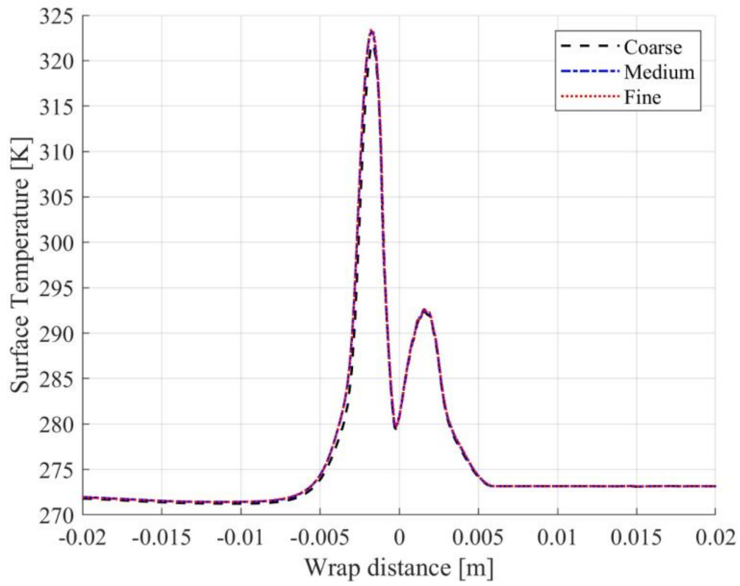

Figure 5.9: Grid dependence of surface temperature of propeller 70% section

In the last comparison of the surface temperature shown in Figure 5.9, the previous obtained findings are confirmed. All grids match each other quite well. Again just small deviations of the Coarse grid are visible especially at the lower surface right behind the leading edge where aerodynamic phenomena take place as described later. By calculating the mean differences referred to the Fine grid as shown in Table 5.5 it can be seen that even the Coarse grid has a difference of just 0.2%.

In summary all grids show a sufficient resolution for observing critical spots and flow conditions. Nevertheless, due to the albeit small deviations and the available computational resources it was decided to use the Medium grid for all propeller simulations.

5.2.2 Comparison with experimental results

The validation of the numerical simulations with the experimental data is a crucial step to verify the accuracy of the numerical results. It provides information about the correctness of the numerical setup, the material properties of the propeller layers and if assumptions like the calculations of the propeller inflows are in an acceptable range. Furthermore, numerical simulations provide more insights into the flow conditions or the effects inside the structure, which would be costly to examine experimentally. With corresponding results of numerical and experimental investigations, the numerical results are more capable to describe the complex processes during icing conditions than the experimental results. Furthermore, these results can be used to obtain a deeper understanding of the ongoing phenomena.

Table 5.6 shows the numerical parameter setup of all further propeller CHT-simulations within this thesis. Some parameters like the heating cycles are not listed, because they need to be set for each simulation individually. As described in section 3.1.2 the turbulence model k-ω SST was used for the propeller simulations. Anti-icing simulations assume no ice accretion and therefore no initial surface roughness is required, hence laminar-turbulent transition was activated.

FENSAP	
Turbulence model	k-ω SST
Transition	Intermittency
Surface roughness	No roughness
BC wall parameters	Heat Flux: 0 W/m^2
Artificial viscosity	Streamline upwind + cross wind dissipation 1e-7
DROP3D	
Physical model	Droplets
Distribution	Monodisperse
Water density	1000 kg/m^3
ICE3D	
Ice – Water model	Glaze - Advanced
Beading Model	Activated
Compute EID	Enabled
Roughness output	Sand-grain from beading
C3D	
Material definition	Table 3.2
BC – walls	Heat Flux: 0 W/m^2
BC – interface	Nothing

Table 5.6: Numerical parameter setup for the propeller CHT-simulations

For the experimental research, the propellers were equipped with thermistors positioned at the foremost point of the foam core as shown in Figure 5.10. Due to manufacturing variations, it was assumed that the thermistor positions vary around 1mm in every direction. Regarding the analyzed propeller sections, all thermistor temperatures obtained from the numerical results are taken at the exact same position. Starting exactly at the front tip of the foam core, for the 50% and 70% section the temperature was taken from the point shifted 0.1 mm in the foam core and not changing the height. For the 30% section the temperature was taken at the position shifted 0.8 mm in the foam core and 0.1 mm downwards.

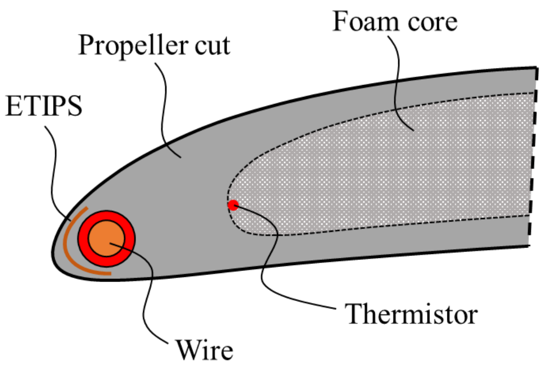

Figure 5.10: Schematic sketch of the thermistor position within the propeller

The first validation is done with the test cases #1 and #3. Both cases have the same icing conditions but test case #1 was done at −5 °C and test case #3 at −10 °C. The IPS is powered constantly according to Table 4.1. The comparison of the experimental results with the numerical outputs are shown in Figure 5.11 and Figure 5.12. The experimental data show two data sets for every propeller section, because thermistors were built in on both blades of the propeller. For the 70% section just one set of data is shown because a wire of one thermistor was cracked right before the first test execution.

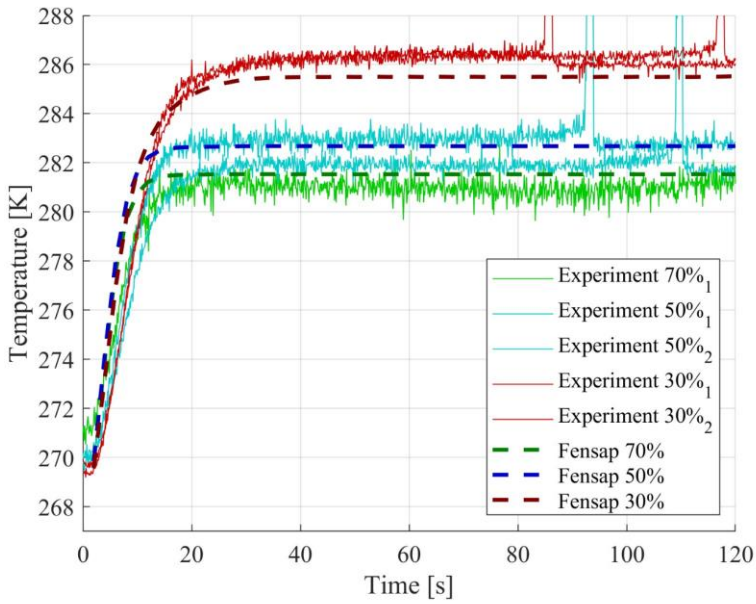

Figure 5.11: Comparison of internal temperature to experimetal test case #1

It can be seen that the numerical data agree well with the experimental data when convergence is achieved. As described in section 4.2 all experimental measured temperatures have an accuracy of ±1 K. To maintain clarity in the plots, the ranges of experimental deviations were not shown in the figures. The differences between the blades regarding the experimental temperatures at corresponding propeller sections have several causes. For the 30% section a bigger difference between the blades can be observed for test case #3 than for test case #1. This difference might be caused by uneven appearance of runback ice behind the heated zone of the two blades, which was observed during the experiments. This is most likely caused by small surface impurities or flow field variations. For the 50% section in both cases, a similar gap occurs between the blades. This might rather indicate manufacturing inaccuracies when the thermistors are not placed in the exact same positions. Both explanations can be strengthened by having a look at the experimental data of test case #2 (see Figure 5.13). Nevertheless, the experimental data show useful results. The differences in the total reached temperatures of the relevant propeller sections are due to the different inflow velocity caused by the radial distances at the propeller blade. This can also be confirmed by comparing the convective HTC between the three propeller sections, as discussed later.

The biggest observable difference between the numerical and experimental results can be seen in the temperature gradient within the first 15 s - 20 s of the tests. The steady temperature is reached in the numerical results faster than in the experiments. This is more evident in test case #3, where much higher temperatures are generally achieved due to the greater ratio between ambient temperature and heating power. Considering equation (2.15), material properties such as density, specific heat and thermal conductivity have the greatest influence on how fast heat is transferred through a solid. The heater power and with it the temperature difference that forces heat conduction has an influence as well. The power is known from the test execution, so the uncertainty of the material values is more likely.

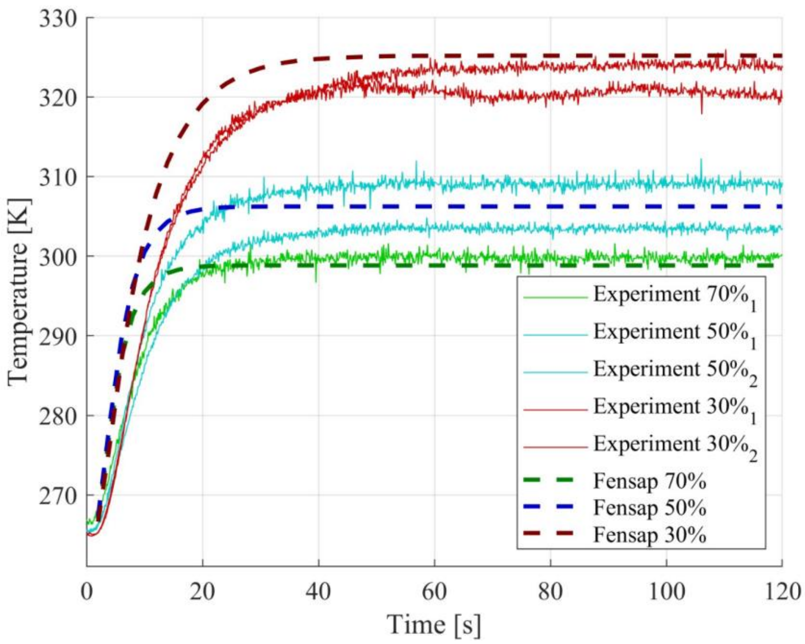

Figure 5.12: Comparison of internal temperature to experimetal test case #3

Despite the inaccuracy in the temperature gradient, the reached temperatures of the numerical simulations are in good agreement with the temperatures obtained experimentally. For the 70% section, the difference is the smallest, while for the 50% section the numerical data is right between the two blades for both test cases. The biggest difference can be observed by the 30% section, which are still in an acceptable range.

To continue with the dry test case #2 as shown in Figure 5.13, Figure 5.14 and Figure 5.15 separately for each propeller section, good agreement between the numerical and experimental results are observable as well. To maintain comparability between the dry (#2) and wet (#1, #3) test cases, the stationary anti-icing module of FENSAP-ICE was also used for test case #2. The unsteady de-icing module of FENSAP-ICE would have been able to simulate changing heater powers, but this would led to results with decreased reliability due to missing validation. Differences to the anti-icing module occur in required inputs like initial surface roughness to mimic ice accretion or the method used to calculate the HTC, because the de-icing module cannot handle the EID module. For that reason, the dry simulations were performed with the anti-icing module for each heater power respectively by setting the LWC to 0 g/m^3. The temperatures are taken at the same position for all three test cases as described above.

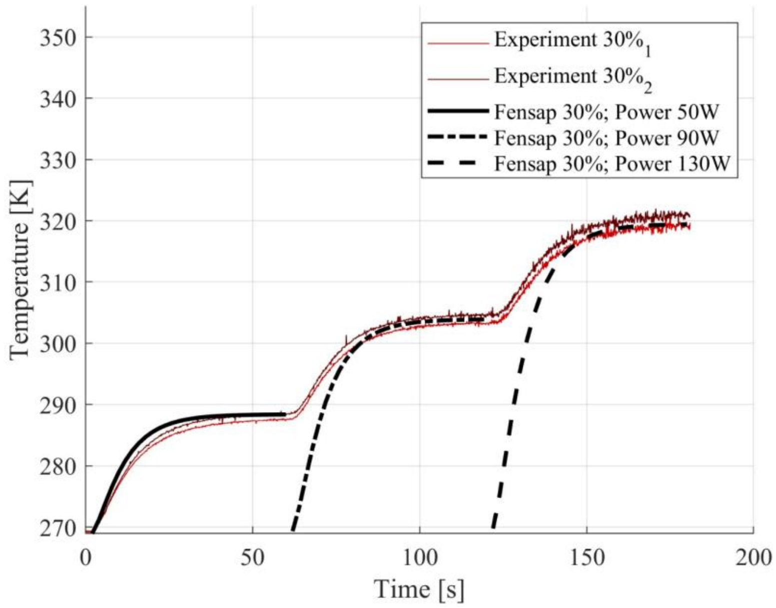

Figure 5.13: Comparison of internal temperature to experimental test case #2 (−5 °C) for 30% section

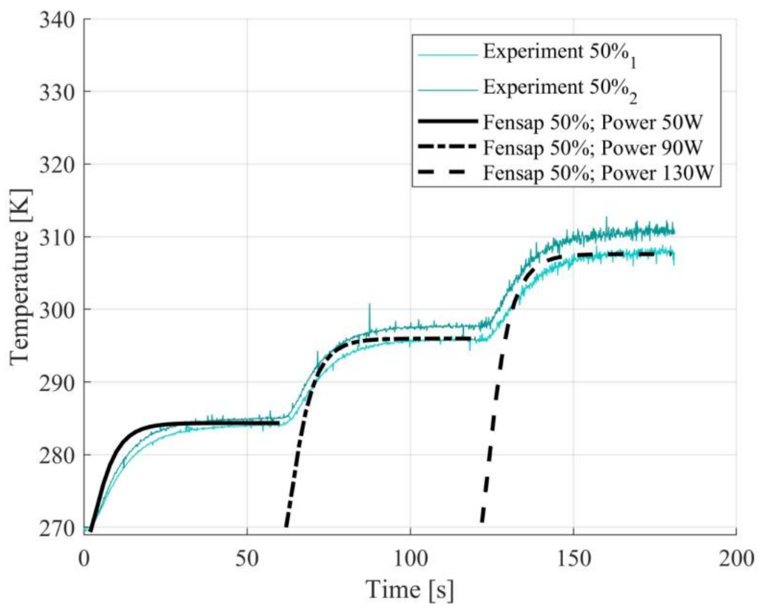

Figure 5.14: Comparison of internal temperature to experimental test case #2 (−5 °C) for 50% section

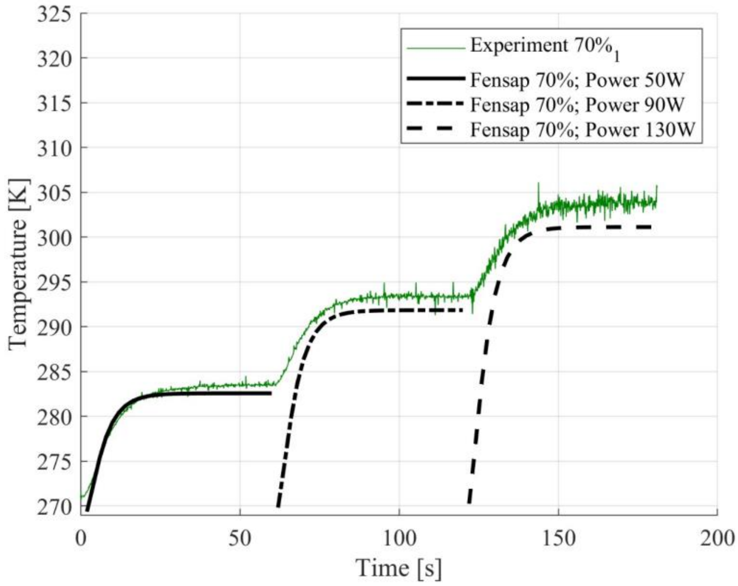

Figure 5.15: Comparison of internal temperature to experimental test case #2 (−5 °C) for 70% section

Due to a limitation of the anti-icing module, the initial temperature of the simulations is the same. The additional time required for the 90 W and 130 W cases compared to the experiments is clearly visible. At first glance, it seems that the temperature gradient between the 90 W and 130 W cases are always different compared to the 50 W case related to the experiments. Based on the experiments where every heater power step lasts more or less 60 s, the simulations are set to a duration of 60 s as well. Therefore, the time to convergence is longer in the 90 W and 130 W cases, which means a greater difference at the beginning compared to the experiments. If one would shift the simulation results to the time when the temperature equals the temperature of the previous run, one would determine that the temperature gradients at the beginning are all steeper than in the experiments, as already observed in test cases #1 and #3.

Furthermore, an interesting difference emerges when comparing the data of test case #1 with that of test case #2, both at a temperature of −5 °C but with different LWC. The first 60 s of test case #2 the heater is powered with 50 W, whereas in test case #1 the heater is powered with 70 W. When comparing an investigated propeller section, the reached internal temperature in test case #2 is always higher than for test case #1. This might be a first indicator of differences between cases where only convection occurs, as in test case #2, and the combination of convection and evaporation, like in test case #1, where obviously more heat is dissipated at the surface of the propeller in the area of the ETIPS. Further analysis on that can be found in the following.

5.2.3 The effects of flow and icing conditions

To understand the occurring aerodynamic and thermodynamic phenomena, properties like the HTC and heat fluxes (HF) are analyzed. The difference in total temperatures achieved between the three propeller sections can be observed by the comparison of the three HTCs as shown in Figure 5.16.

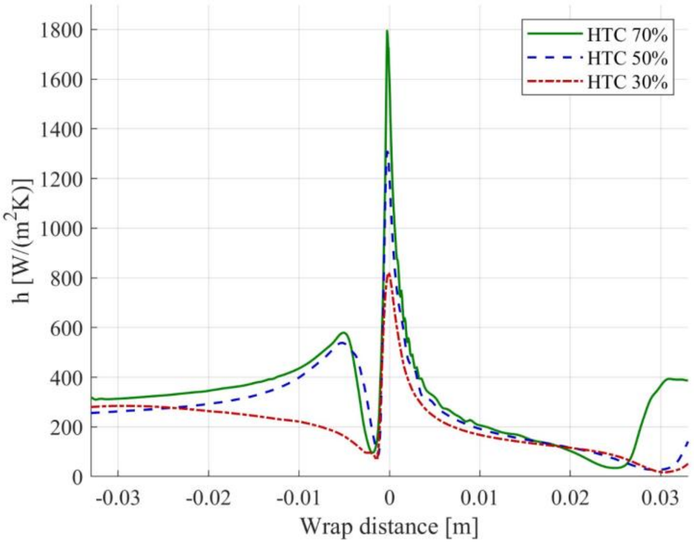

Figure 5.16: Comparison of HTC between propeller sections using FENSAP-ICE results

The 70% section has the biggest radial distance from the propeller hub and therefore the biggest relative speed, followed by the 50% and 30% sections. This results in the highest inflow velocity at the leading edge for the 70% section and therefore convection is forced the most at that point, which leads to the highest peak value of the HTC. In addition, several flow conditions and effects can be seen in the evolution of the HTC along the surface. Starting at the stagnation point of the flow right at the propellers leading edge. For all three cases, the flow has a laminar structure and start to build up a boundary layer. Along the upper surface, the HTC lowers similar in all cases as typical for laminar boundary layers as described in 2.2.3. In all three cases a drop of the HTC with a followed rise is visible for the 70% section at a wrap distance for 0.024 m and the 50% and 30% sections at around 0.03 m. The drop indicates the position where the flow starts to detach due to the curvature of the propeller surface. In the detachment area, backflow occurs and the flow transits from a laminar to a turbulent characteristic as shown in Figure 5.17. The rise in the HTC afterwards shows the region where the turbulent flow reattaches and heat is extracted more efficient again.

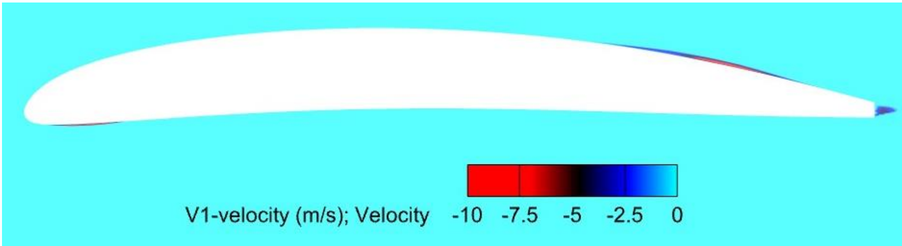

Figure 5.17: Visualisation of separation bubbles at the 70% propeller section

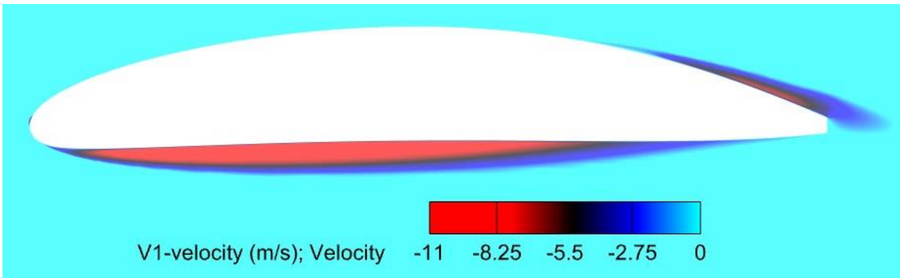

Figure 5.18: Visualisation of separation bubbles at the 30% propeller section

On the lower surface, the low point right at the wrap distance of −2 mm is in accordance to an observable separation bubble. Due to the rather steep negative AOA for the 30% section, the separation bubble is along the complete lower surface of the propeller and the flow does not re-attach but rather forces backflow as shown in Figure 5.18. For the 50% and 70% sections, the flow re-attaches almost immediately with a turbulent characteristic. This causes the rise in HTC at that position and is followed again by a slight reduction along the surface due to the development of a boundary layer. The separation bubbles and evolving vortexes in that area cause peaks of the water film. It seems that the separation leads to small issues with the film modelling, since the fluid is pushed into one position from both sides. Interesting to observe in Figure 5.20 for the 70% section. In reality, the water film would be rather pulled with the separating flow above the separation bubble. In general, each of the three propeller sections show individual flow characteristics due to the difference in AOA and rotation rate. The most pronounced effects are observable at the 70% section because of the highest inflow speed and therefore in the following, some results are discussed at the 70% section only.

Regarding the heat fluxes of test cases #1 and #3, the separation between convection and evaporation is clearly visible. Figure 5.19 and Figure 5.21 show the convective, evaporative and the sum of both over the propeller surface. Additionally, the caught water is shown on the right y-axis as well.

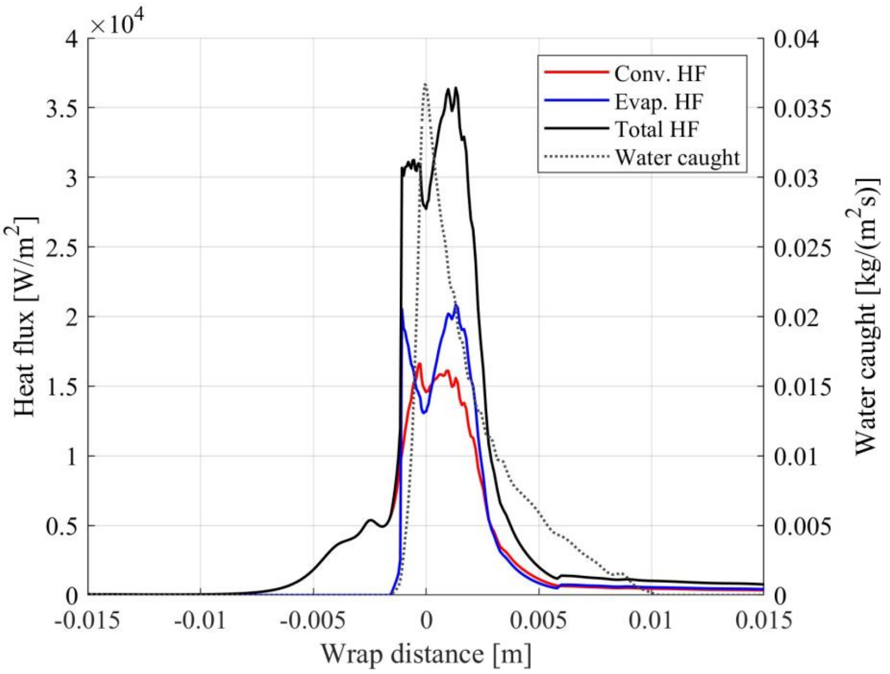

Figure 5.19: Heat fluxes of test case #1 at the 70% section

Many phenomena related to the previously discussed effects and influences are visible. Starting with general conspicuities, the evaporative heat flux is only dependent on water. At locations without a water film or impinging water droplets, no evaporation can be found and only convection occurs. According to equation (3.15), evaporation depends mainly on temperature. The rise in heat causes the phase change from liquid to gas. Furthermore, the evaporative heat flux at the impinging zone reaches higher values than the convective one. This might be due to the better heat exchange between water and solid than air and solid, which causes a more efficient heating of the water film. This subsequently leads to a higher evaporative heat flux. In these cases, more energy goes into latent heat. Indications for that are due to general lower values of the convective heat flux in areas where water occurs.

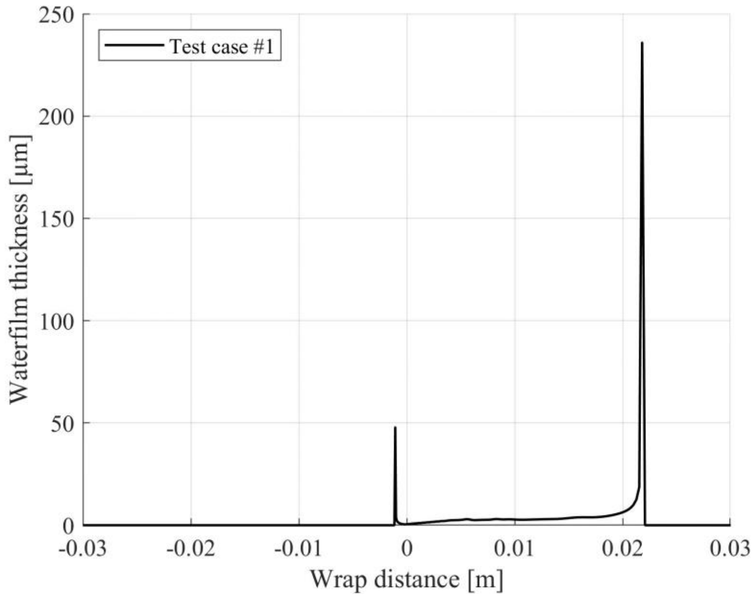

Figure 5.20: Waterfilm thickness along the surface of test case #1 at the 70% section

Interesting is the drop of the evaporative heat flux at the stagnation point at the leading edge. At this point the highest amount of water impingement on the surface is reached. At the stagnation point, effects such as impingement cooling and forced convection must be taken into account. As cold water droplets come into contact with the heated surface, heat is transferred into the water due to the temperature difference between the surface and the cold water. However, despite this heat transfer, the energy extracted at the leading edge is not sufficient to instantly evaporate the continuous stream of droplets and a water film occurs, comparing Figure 5.20. The two unphysical peaks of the water film are discussed above. Due to the shear stress, the airflow along the surface initiates the movement of the water film and leads to the smallest thickness at the leading edge, in accordance to equation (3.12). The ongoing stream of cold water droplets on the leading edge constantly extracts heat. That might cause the drop of the evaporative heat flux. The heat flux increases again downstream when the extracted heat is sufficient to cause evaporation.

The convective heat flux on the other hand stays constant or even experiences a slight rise at the leading edge. Convection is treated by temperature difference between surface and air or a high HTC. While the surface temperature reaches a minimum at the leading edge due to the impinging droplets as shown in Figure 5.23, the HTC reaches its maximal values as can be seen in Figure 5.16. This peak value is due to the flow at the stagnation point, when convection is forced the most. The particles extract heat and increase the internal energy according to 2.2.3. Due to the high speed of the air flow, these particles are moved away from the surface much faster and space is created for new particles, which can extract more heat.

In addition, the total heat flux becomes almost zero at the surface locations where the heat generated from inside is insufficient and the surface temperature drops to almost 0 °C.

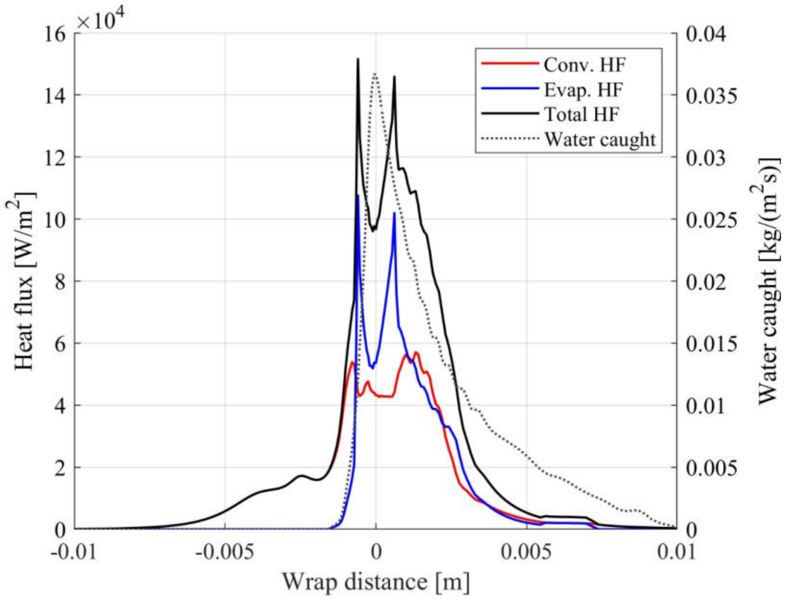

Figure 5.21: Heat fluxes of test case #3 at the 70% section

Evaporation and convection are the two most influencing heat fluxes on the propeller surface. By quantifying the evaporative and convective heat flux above the whole propeller surface it was found that for test case #1 the convective heat flux reaches 88.35 W/m and the evaporative one 75.67 W/m, which corresponds to 53.87% and 46.13%. For test case #3 the values are 260.93 W/m and 216.04 W/m which are 54.71% to 45.29% for convection and evaporation. This shows again that evaporation only occurs when liquid water is present, usually at the leading edge of the heated propeller. Interesting are the almost same relative values for convection and evaporation for both test cases, which differ for just 1%. This might be due to a similar relative ratio of heater power and ambient temperature in the test cases #1 and #3.

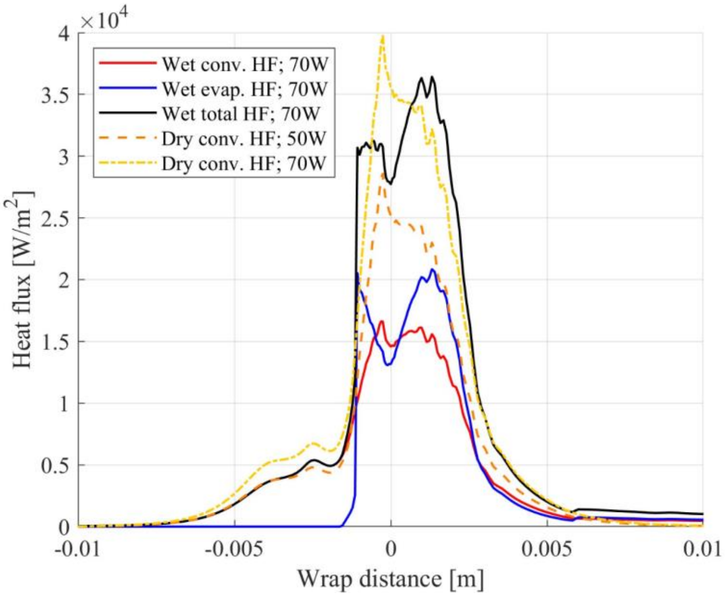

Figure 5.22: Comparison of all heat fluxes between the wet and dry test cases at the 70% section

For a deeper understanding of the differences between the convective and evaporative heat fluxes, comparisons between the wet test case #1 and dry test case #2 are necessary, also taking into account the surface temperatures, as shown in Figure 5.22 and Figure 5.23. Presented are the test cases at −5 °C and the first 60 s of the dry test case #2. Additionally, a further simulation is shown under dry conditions with a heater power of 70 W as in the test case #1. The smallest values in the droplet-impinging zone are found for the wet test case when evaporation is present as well. Increased for the dry cases according to the heater power. The previously described phenomena of water pushed away from the stagnation point along the surface can be seen in Figure 5.22 even more clearly. Considering the wet case and dry case powered with 70 W, the dry case reaches much higher values right at the stagnation point and the heat flux is sharpened. The total HF of the wet case does not reach such high values, but covers a larger area than the dry HF due to the water movement and the heat conduction in the water along the surface, which transfers the heat away from the stagnation point. With regard to the surface temperature at the stagnation point and at the right peak value, which is still in the area of the water impact, it can also be seen that the convective heat flux is mainly determined by the HTC and the temperature difference between the surface and the ambient air. Comparing Figure 5.16, the HTC reaches its maximal values at the stagnation point due to forced convection and therefore most of the heat is dissipated from the surface at that spot and the surface temperature reaches its minimal values. Along the upper surface, the surface temperature reaches a local maximum, which prevents the HF from dropping even though the HTC decreases.

Furthermore, the surface temperature in the impinging zone of test case #1 is lower compared to test case #2, despite the higher power of the wet test case #1. This also applies to cases where wet and dry conditions are each operated with 70 W. This observation again might prove the higher specific heat and increased HTC between water and solid than between gas and solid. More heat from the surface is extracted to heat up the water film and further leads to evaporation.

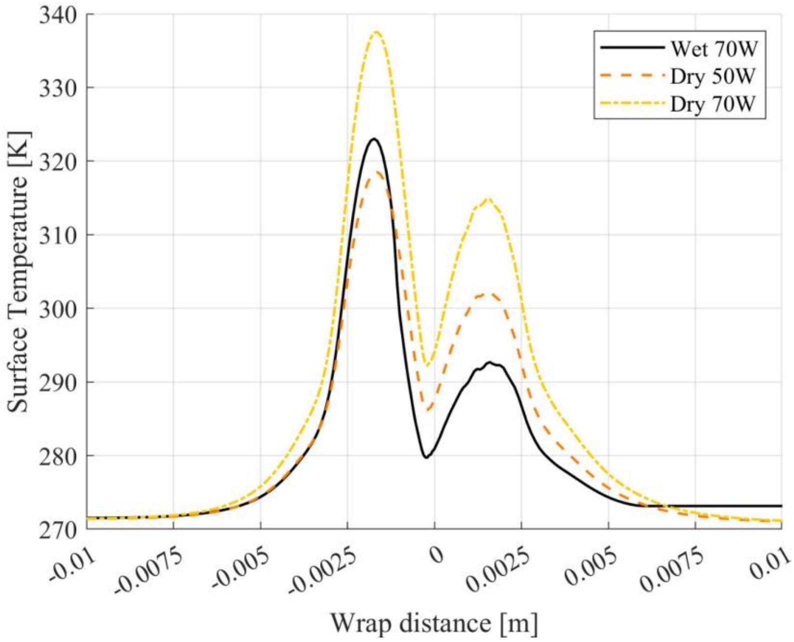

Figure 5.23: Comparison of the surface tempearture between the dry and wet test cases at the 70% section

This is further confirmed by looking at the lower propeller surface when the surface temperature of the wet case with 70 W rises above that of the dry test case with 50 W. The separation bubble causes this maximum temperature when the heat transfer away from the surface is damped. In this area, no water impinges and only convection occurs for all test cases. On the one hand, this shows that with higher heater power the surface is heated even more. On the other hand, in the two cases with 70 W, the influence of water and evaporation is also visible at the surface spots where no water is present. At the upper leading edge, the heat transfer is increased for the wet case, resulting in a lower surface temperature. The result is a greater temperature difference between these surface points and the IPS heater. This leads to a greater heat conduction and heat flux that is mainly forced by the temperature difference. Consequently, less heat is internally transferred to the lower surface despite the same heating power, resulting also in different surface temperatures. That means the internal temperature distribution depends on the location and amount of extracted heat, as shown in Figure 5.24.

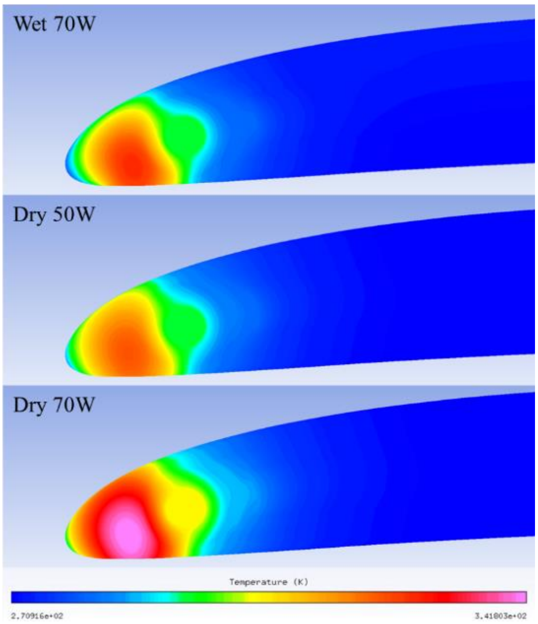

Figure 5.24: Internal temperature distribution of wet and dry test cases at −5 °C with 50 W and 70 W heater power at 70% section

Finally, a different surface temperature behavior can be seen on the upper surface behind the heated area when surface temperatures of around 0 °C occur. For the dry cases, the temperature drops below the freezing point immediately, whereas for the wet case a constant surface temperature can be seen at around the freezing point. This is caused by an accumulation of ice at that point. In contrast to evaporation, when liquid water freezes, energy in form of latent heat is released. This latent heat is sufficient to keep the surface at 0 °C and therefore does not immediately drop below it, as for the dry cases where no water is in the air. By comparing the maximum internal temperatures usually reached at the heating pad, it was found that all the phenomena and appearances discussed above lead to the following findings. The highest temperature of 68.65 °C is reached for the dry case with 70 W followed with 52.86 °C for the wet test case #1 and 48.40 °C for the dry test case #2 at 50 W heater power.

5.3 Numerical uncertainties

As well as experimental uncertainties, numerical ones need also to be considered. Numerical uncertainties due to the underlying discretization of the physical equations and simplifications of the computational models are known, accepted, and not further discussed in this work.

More interesting are the uncertainties that occur due to the definition of the start conditions and the numerical parametrization by the user. A study on a smaller propeller than the one used in this thesis shows a rather early detachment as it is the case with the k-ω SST model as well [91]. However, the exact flow characteristics along the propeller surface have never been examined experimentally. Hence, the choice of the turbulent model might be a source of uncertainty. The same applies for the calculation of the HTC by the EID model that is recommended by ANSYS for high-speed simulations, as it is the case for propellers. The underlying equations and data are both not known in detail and therefore state another uncertainty.

Further, the LWC measurements during the icing experiments showed a non-uniform droplet distribution over the whole propeller area. That might lead to differences compared to the simulations, which were performed with the average LWC from the experiments.

The biggest uncertainty of the numerical simulations states the material properties used for the C3D simulations. The composite layup of the propellers is made out of several different materials, which are also orientated or twisted individually. Furthermore, the thickness of the composite layers is just a fraction of a millimeter, which leads to errors when measuring it. The bulking of a composite layer in the leading edge cannot be taken into account as well. All that makes the calculation of the material values even more complex and lead to several assumptions like even layer thickness or homogeneous fibers. This uncertainty might be responsible for the differences in the temperature gradient as previously discussed. A separate study would be necessary to properly examine the correct material values by experiments and simulations on every material layer separately.

This might further be influenced by grid generation uncertainties. An example is the position of the wire behind the leading edge IPS, based on a propeller section at about 75% radial distance. For the bigger 30% propeller section the wire was at the same position but could have been in reality shifted to the upper or lower surface. That difference might have an influence on the internal temperature distribution.

Nevertheless, among all the described experimental and numerical uncertainties, the numerical results are in good agreement with the experimental data. This observation suggests that the impact of the uncertainties may be less pronounced than initially anticipated or have been good analyzed and the relevant assumptions are in good agreement with real experimental conditions.

6 IPS optimization under consideration of design parameters

6.1 Flow and icing conditions

After validating the numerical simulations by experimental tests, the results are used to optimize the IPS design with regard to efficiency. The new design is numerically tested in several ambient conditions. The first conditions are chosen in reference to the VTT experimental test campaign to validate these results in future campaigns.

Test Case	Temperature [°C]	Air velocity [m/s]	LWC [g/m^3]	MVD [µm]	Run time [s]
#4	−5	25	0.44	20	60
#5	−10	25	0.44	20	60

Table 6.1: Test cases of optimized IPS design for VTT experimental tests

Further conditions are chosen to test the design in realistic UAV inflight conditions. Therefore, the Federal Aviation Administration (FAA) provides several envelopes in the Code of Federal Regulations [92]. The continuous maximum icing defines icing conditions in a stratiform cloud with a length of 17.4 miles and a height between zero and 22,000 ft. This rather low regime covers the altitude range of typical UAVs. The envelope can be seen in Figure 6.1. With the chosen cases it was tried to cover as much as possible of the envelope until the temperature regime where the IPS does not work anymore.

Test Case	Temperature [°C]	Air velocity [m/s]	LWC [g/m^3]	MVD [µm]	Run time [s]
#6	−2	25	0.760	15	60
#7	−2	25	0.140	40	60
#8	−15	25	0.450	15	60
#9	−15	25	0.078	40	60
#10	−30	25	0.200	15	60
#11	−30	25	0.038	40	60

Table 6.2: Test cases of optimized IPS design according to FAA

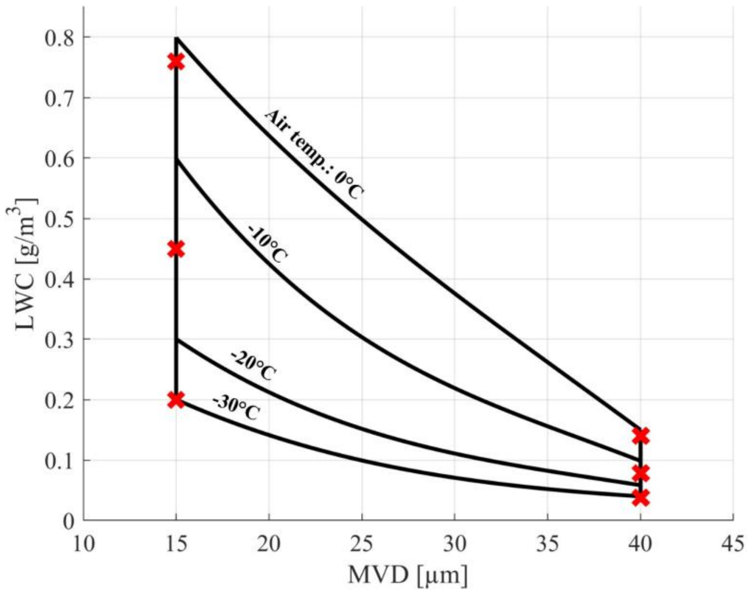

Figure 6.1: Continious maximum envelope of FAA

The cases of less than −15 °C are tough regimes. Just a few specialized UAVs e.g. for arctic research would experience such low temperatures. Nevertheless, in order to find the limits of the IPS, these conditions are considered as well.

6.2 IPS optimization in form of additional heaters

6.2.1 Optimization setup

As previously shown the original ETIPS design that consisted of only one module in the leading edge of the propeller could not prevent the accumulation of ice along the upper surface of the propeller in both the experiments and the numerical results. Even with maximum power of the ETIPS and overshooting the internal temperature limit, the heat conductivity to the back of the propeller along the surface was insufficient and ice always accumulated.

On the rear part of the 70% section at the lower surface, a relatively thin layer of ice accretion occurs in most of the cases as well. In this thesis, the focus is on avoiding the upper runback ice, as this causes a higher impact on aerodynamic degradation. Regarding the aspect of runback ice on the upper surface of the propeller, the improving concept is to implement more ETIPS modules along the surface of the propeller as shown in Figure 6.2. The idea with this method is to keep more of the upper surface above the freezing temperature of 0 °C. One condition in this optimization process is that the basic layup of the composite propeller, as described in 3.5, needs to stay the same. Furthermore, it was always the aim to keep the design and functionality as simple as possible to remain realistic in a manufacturing manner. For that reason, it was decided to power all of the added heaters as one big heater pad. The separations are done to numerically examine how long extra heating is necessary to avoid runback ice and not to generate a grid for every case.

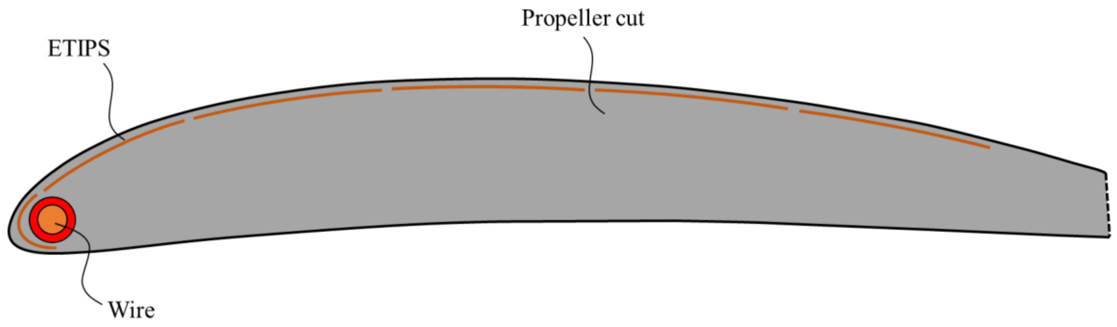

Figure 6.2: Schematic sketch of additional heater pads along the surface

As can be seen, five additional modules, each the length of 5.730 mm and the height of 0.215 mm are integrated between the glass fiber layers just like the original ETIPS module in the leading edge. The design was customized on the 70% propeller section, since this section has the smallest chord length of all of them. The heater modules are made out of unidirectional carbon, as the heater pad in the leading edge. The unidirectional carbon is not twisted in the additional integrated heaters as it is for the single leading edge heater. Hence, these heater elements have anisotropic properties and an equivalent height of 0.200 mm with an equivalent conductivity of 0.693 W/(mK) was calculated. With these dimensions, the optimized design fits perfectly in the 70% section layup above the wire and is integrated in the 50% and 30% sections as well.

6.2.2 Numerical results of optimized IPS design

Testing the new developed design under the icing conditions described in chapter 6.1 is an important step to gain first impressions of its performance. The testing part and determining the required heater powers is an iterative process. After the flow and icing conditions are defined, the first test is performed at the 70% propeller section. Since this is the most critical section of highest velocities and therefore highest rate of convective cooling. As previously observed, the 70% section requires the highest heater power. Furthermore, the heater power needs to be as low as possible, but high enough to still keep the surface free of ice. The power should be kept as low as possible in order to keep both the power supply and the thermal influences on the material as low as possible. Besides this, the internal temperature must not exceed the critical limit of 60 °C, which must be checked especially for the 30% section. After the required heater powers are found, they were also tested at the 50% and 30% sections. For the tests of the FAA icing conditions only the 70% and 30% sections are considered, as it was found that all the requirements of the 50% section are in-between. This implies that when the IPS works for the 70% and the 30% section it must also work for the 50% section.

The first step in the optimization process was to determine how many additional heaters are necessary to avoid runback ice. Regarding the test cases #4 and #5, it was found that four additional heaters are required. Since the 30% section has a much longer chord length, the upper surface length is greater than that of the 70% section and, due to the different flow properties, runback ice occurs even further downstream, as shown in Figure 6.3. Further observations show that in most cases for the 70% section three additional heater pads are enough to avoid runback ice. Since the heat is transferred over the surface, the last heating pad is no longer necessarily required. This effect decreases when reaching the lower limit of the necessary heater power. Out of this observation, all further simulations were done with four additional heater pads along the upper surface of the propeller.

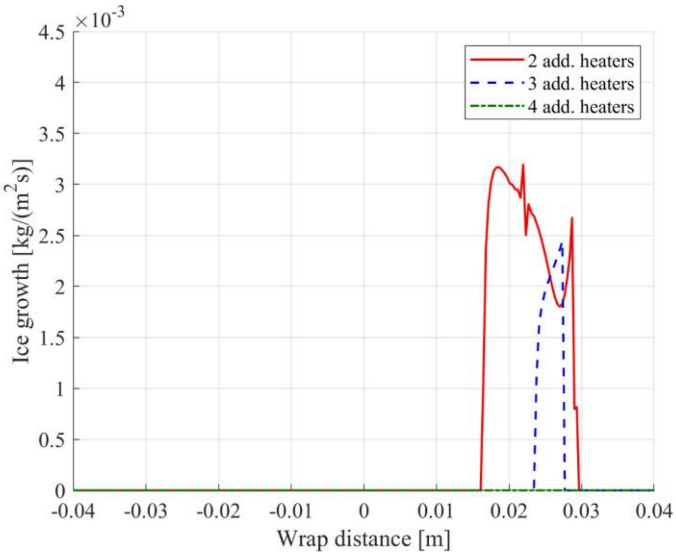

Figure 6.3: Ice growth at the 30% section for test case #4 with different amount of additional heaters

Interesting observations can be found by analyzing the surface temperatures at the three propeller sections when two, three or four heaters are powered independent of the ambient temperature. Figure 6.4 - 6.6, show the surface temperatures of the three propeller sections for test case #4. Regarding the area of the leading edge, the 30% section reaches the highest temperatures as already previously discovered due to the rather steep inflow. The temperature along the upper surface due to the additional heaters increases with a constant gradient. This is also the case for the 50% section, but not for the 70% section. At the 30% section the airstream at the upper surface remains longer laminar and a boundary layer builds up, the effectiveness of heat extraction decreases with the length of the boundary layer and the temperature increases. This is in good agreement with the HTC along the surface. A similar behavior occurs for the 50% section. For the 70% section, an extreme peak of the surface temperature at the fourth heater position develops. This is due to the flow detachment in this area where even backflow appears as described in section 5.2.3. In accordance to the low HTC value at this position, heat extraction is damped and the temperature increases unproportioned since neither evaporation nor convection can extract heat in this case.

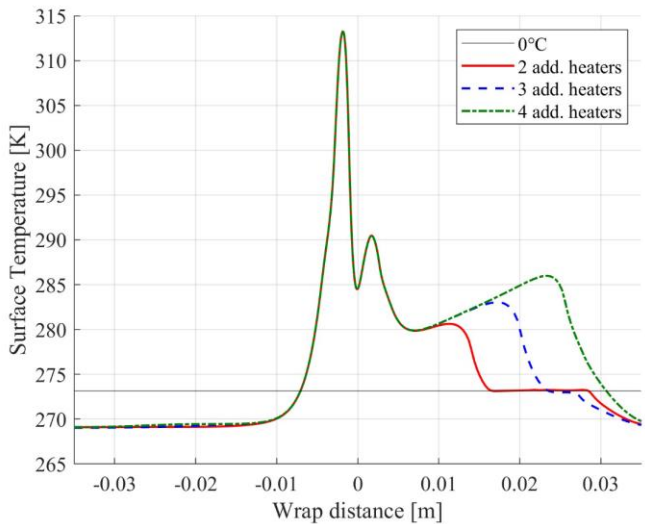

Figure 6.4: Surface temperatures at the 30% section for test case #4 with different amount of additional heaters

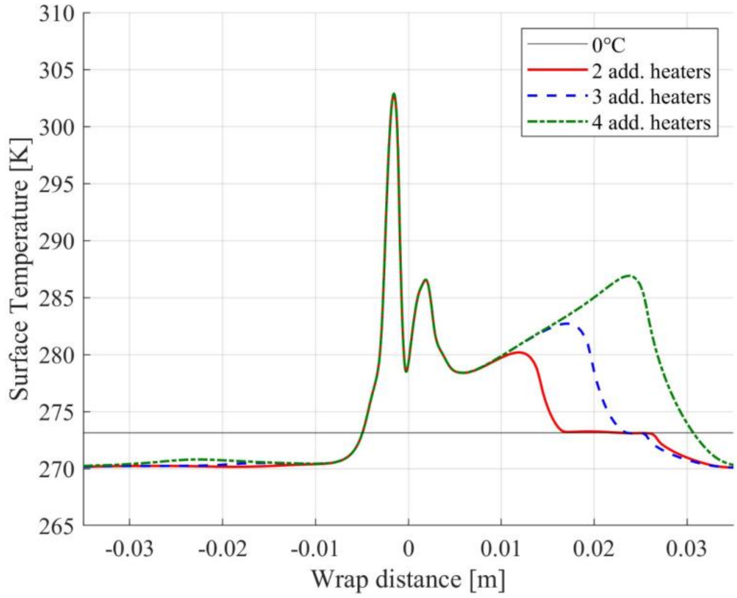

Figure 6.5: Surface temperatures at the 50% section for test case #4 with different amount of additional heaters

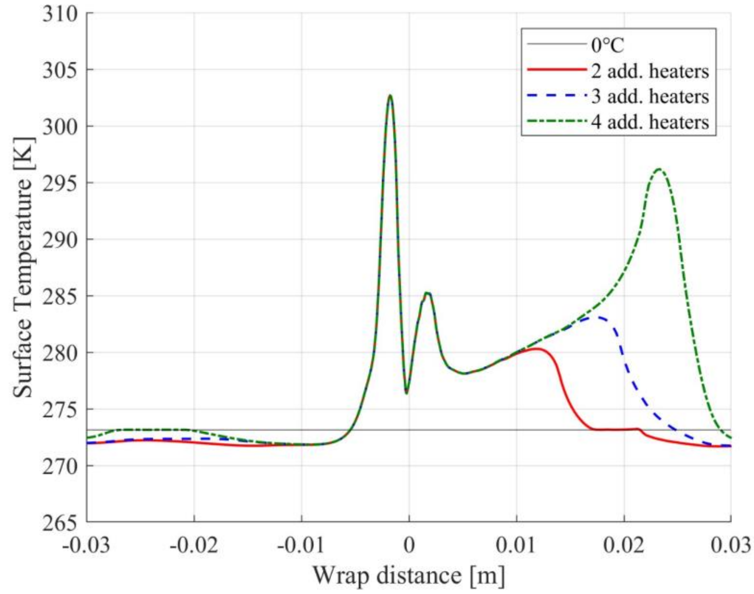

Figure 6.6: Surface temperatures at the 70% section for test case #4 with different amount of additional heaters

Regarding the cases when only two heaters are powered, the surface temperature does not immediately drop below zero degrees behind the second heater. It remains a few millimeters around the freezing point. This is due to the latent heat that is released and heats the surface when water changes its phase from liquid to solid.

For the VTT experimental test cases #4 and #5 the new design performs well. The upper surface stays ice-free and the internal temperature for all cases is below the critical 60 °C as shown in Table 6.3.

Test Case	Power LE [W]	Power add. heater [W]	Max. internal temp. 30% [°C]	Max. internal temp. 50% [°C]	Max. internal temp. 70% [°C]
#4	40.01	59.14	42.45	32.65	31.35
#5	55.01	39.43	55.55	41.75	39.75

Table 6.3: Required powers and maximal internal temperatures of test cases #4 and #5

For the test cases #6 and #7 also no problems appeared, since the ambient temperature is just below the freezing point and even low power levels are sufficient to prevent any ice accumulation. This is not the case for the −15 °C regimes #8 and #9. For these cases, the first limit of the IPS is reached when the heaters in the 70% and 30% are powered equally. With the power required to keep the surface in the 70% section ice-free, the maximum tolerable internal temperature of 60 °C would be exceeded in the 30% section. Table 6.4 shows the smallest possible power differences between the 30% and 70% section when both are developed independently. Interestingly the test case #8 with the rather high LWC and low MVD has a bigger impact on the required power than the case #9 with lower LWC and higher MVD. For #8 the power difference in the leading edge heater is around 25 W while for the additional heater the difference is around 10 W. The differences are smaller for #9 with just 20W in the leading edge and 0 W in the additional heater powers. It seems the LWC in general has a bigger impact on the required heater powers than the MVD. The difference in the powers between the 30% and 70% section can be achieved in two different ways. The easiest solution is to power the heater in the leading edge and the additional heaters separately. This has the consequence of manufacturing issues due to additional wires in the structure. The second possibility might be a passive option by varying the thickness of the heater layers and with it the resistivity is changed. This option might reduce the manufacturing issues since the leading edge and the additional heaters can be connected in series and powered with the same current. On the other hand, this option requires more space in the layup due to the changed thickness. Additionally, the second option is fixed after manufacturing and more designed for a specific temperature regime, while the first option can be adapted to various conditions by the power supply. To improve the setup even further and make it adaptable to even more conditions the additional heaters should not just be separated spanwise but also chordwise. This would offer the possibility to heat every region of the surface of the propeller under consideration of the current surrounding flow conditions.

Test Case	Power LE 70 % [W]	Power add. heater 70% [W]	Power LE 30 % [W]	Power add. heater 30% [W]	Max. internal temp. 70% [°C]	Max. internal temp. 30% [°C]
#6	10	3.9	10	3.9	11.0	11.0
#7	20	4.9	20	4.9	18.0	22.6
#8	85	19.7	60	29.6	59.9	59.2
#9	70	19.7	50	19.7	54.4	57.7
#10	100	24.6	60	22.18	67.0	50.5
#11	100	24.6	50	19.7	76.0	46.6

Table 6.4: Required powers and maximal internal temperatures of test cases #6 - #11

The last cases #10 and #11 are extreme ones. For the 70% propeller it is not possible to avoid runback ice and keep the temperature below 60 °C. In contrast, the 30% section shows satisfactory results. With that outcome, the limit of the IPS is obviously reached and other approaches might be necessary.

In general, it is shown that the most critical part of the design is the heater in the leading edge. In the critical cases, ice accretion is observed at the leading edge when the internal temperature of 60 °C was already reached. The position of the heater is too deep in the structure and the overlying layers have a too big thermal resistance. As a result, the heat is not sufficiently conducted to the surface, but leads to a hot spot at the position of the heater. A change in the composite layup also affects the stiffness and strength of the propeller, which is why a new layup is not possible without testing the mechanical and aerodynamic aspect. For this reason, the structure was retained for this work.

6.3 The effect of an increased heat conductivity layer

The following approach focuses on the above-described issue of high thermal resistance layers around the leading edge heater. A rather abstract consideration is done by applying a copper layer in the propeller structure to show the influence of a reduced heat resistance layer around the leading edge heater. The original propeller setup with just one heater pad in the leading edge was taken. In the numerical setup, the outer glass fiber layer is then applied with the material values of copper according to Table 3.2 and showed on Figure 6.7.

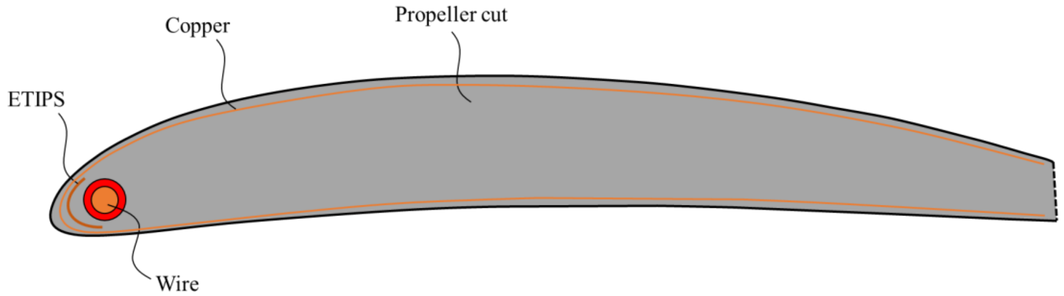

Figure 6.7: Schematic sketch of a copper layer in the propeller structure

Compared to glass fiber, copper has a much higher heat conductivity, higher density and a smaller value of the specific heat. This setup is tested and compared to previous results of test cases #4 and #5.

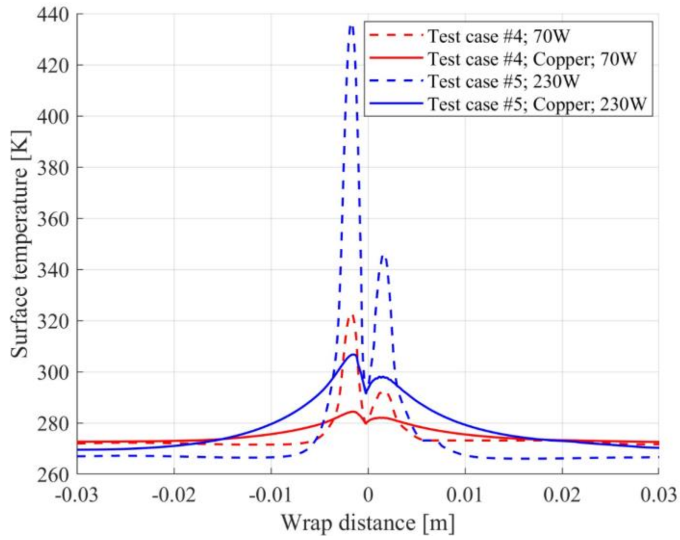

Figure 6.8: Surface temperatures of test cases #4 and #5 with and without copper layer

The results show a much better temperature distribution due to the higher heat conductivity and less heat resistivity. Thus, a reduced maximal internal and surface temperature occurs. Due to the improved heat transfer in the copper layer along the surface, the flattening of the temperature along the surface is longer. Hence, the surface is kept above the freezing point in a larger area. Generally, the internal temperature is more evenly distributed and temperature peaks are reduced due to flow phenomena such as the separation bubble at the lower surface. Regarding test case #4, the maximum internal temperature is reduced from 52.86 °C to 28.1 °C. An even greater reduction occurs for test case #5 with more extreme values of ambient temperature and heater power. The temperature is reduced from 173.14 °C to 88.75 °C. Due to the larger surface area and the associated higher temperature, especially in the areas without a water film, the ratio between convective and evaporative heat flows has changed compared to the results in chapter 5.2.3. For test case #4 the convective heat flux states 65.71% whereas the evaporative heat flux is reduced to 34.29%. The percentages for test case #5 are 59.34% for convection and 40.66% for evaporation. These results show an increased convective heat flux due to larger areas with higher temperatures, while evaporation only occurs when liquid water is present and there is enough energy in form of heat to cause the phase transition.

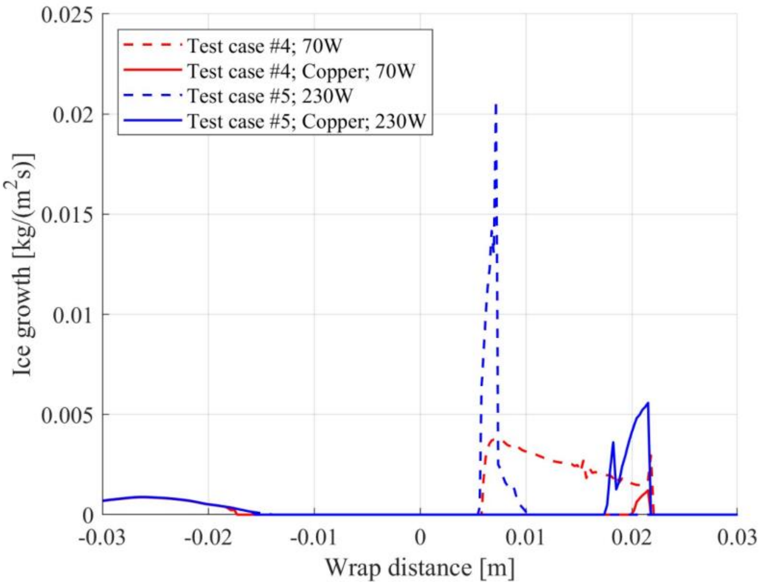

Figure 6.9: Ice growth of test cases #4 and #5 with and without copper layer

As shown in Figure 6.9 ice accretion occurs mainly in the rear part and increases more slowly. On the lower surface, the heat conductivity is not high enough to avoid ice accretion. Nevertheless, even that thin copper layer of just 0.06 mm not only improves the prevention of ice accretion, but also reduces the heat impact on the internal structure by distributing the heat internally much faster and more efficient.

That concept shows numerically interesting results in achieving lower temperature peaks and bigger areas that are free of ice. These tests again neglect the effects on the strength and stability properties of the propeller or the manufacturing possibilities. The biggest problem occurs due to the electrical conductivity of copper, that is directly in contact with the powered heater pad. In addition, copper has a higher density than composite materials and therefore has a greater impact on the propeller weight. Further studies are required for the practical possibilities and applications, but the results obtained show that it might be worthwhile to pursue this idea further. A combination of both optimization concepts might be worth a further study. Thus, the reduction of the required heating pads along the upper surface to completely avoid runback ice could be achieved at the same time as a reduced necessary power. Further might an additional heater along the lower surface in combination with the copper layer avoid the ice accretion on the lower rear side as well.

In summary, both propeller design optimization approaches show interesting results and offer a big field for further work. Nevertheless, it must be taken into account that both approaches have so far only been tested numerically with all the uncertainties described. The next crucial step would be to validate these results experimentally to be able to make well-founded statements.

Further, all results described in this thesis refer to an exact flight situation in terms of inflow speed, rotation rate and environmental conditions. Therefore, further studies could analyze the IPS performance in different flight states to enlarge the data base.

7 Conclusion

In this thesis, investigations of the anti-icing capabilities of an ice protection system for UAV propellers have been performed. The medium sized fixed-wing UAV under consideration has a maximum take of weight of around 25 kg. The IPS uses the method of resistive heating and thus belongs to the category of electro-thermal ice protection systems. An already existing ETIPS design was examined through a combination of experimental validation and numerical simulations. The objective was to evaluate the system's efficiency in preventing ice accretion while at the same time its impact on aerodynamic and thermodynamic factors has been considered. On this basis, further design optimizations were worked out and numerically tested. Always under the scope of not exceeding the critical glass transition temperature of 60 °C of the composite propeller.

Through an experimental test campaign in an icing wind tunnel, the ETIPS was tested in various icing and flow conditions that mimic realistic flight conditions. Internal temperature values measured at three sections along the propeller radius by thermistors integrated in the propeller layup revealed first indications of the internal temperature distribution. The obtained data offered insights on locations of thermal hot spots, the influence of radial distance and the issue of runback ice was obtained. The results showed already high efficiency of the IPS at the leading edge but also stated the weaknesses along the upper surface where in many cases runback ice appeared. Additional thrust measurements confirmed again the importance of an IPS in order to guarantee a safe operation under such critical conditions.

To gain a deeper understanding of the prevailing phenomena, a numerical examination was conducted using computational fluid dynamics simulations. The data obtained through the simulations were initially validated not only by the experimental results but also by data from the literature. The validation showed very good agreement in the comparisons with the experimental results and the literature, thus ensuring a high probability for the correctness of the numerical simulations. Observed differences were discussed under consideration of experimental and numerical uncertainties and were taken into account for the analysis of all numerical results with in this thesis. The numerical 2D simulations were done on three propeller sections according to the thermistor positions of the experimental sensor setup (30%, 50% and 70% of the propeller radius) providing insights in different aerodynamic characteristics. The numerical simulations, which were carried out with the same conditions as the experimental setups, enabled a more precise analysis of the flow phenomena, the temperature distributions within and along the surface as well as the heat transfer mechanisms than it was possible experimentally. The important role of flow characteristics like detachments or laminar-turbulent transitions and their impact on heat transfer coefficient were taken into account. Further studies were done by tests containing different amount of liquid water in the ambient air. This enabled examinations on only the convective heat transfer mechanisms, as compared to cases where the combination of convective and evaporative heat transfer mechanisms played a role.

A large part of the thesis consisted of the optimization process of the ETIPS design. Fundamental were the previously described experimental and numerical inquiries. The focus was on the approach to prevent runback ice along the upper surface, which was mainly caused by the original IPS design being limited to the propellers leading edge. Further, the maximal internal temperature is set at 60 °C by the glass transition temperature of the composite materials. The first optimization case aimed to expand the heated surface along the upper surface by supplementing heater pads. The iterative process of test cases and simulations between the three propeller sections resulted in an IPS design that could be adapted to varying icing conditions. As a result, leading edge heating for keeping the propeller ice-free was elaborated as a critical component under the aspect of generating the highest internal temperatures at this point.

An additional study was done by integrating a copper layer into the propellers composite structure to examine the influence of an enhanced heat conductivity layer. Simulations showed reduced temperature peaks, larger ice-free areas and more uniform temperature distributions. Despite these promising results, this concept requires further examinations regarding structural and manufactural topics as well as electrical issues between the copper layer and heater pad.

In conclusion, this thesis offers an analysis for the development of an electro-thermal ice protection system for an UAV propeller based on both experimental and numerical investigations. The focus is on the thermal effects on the propellers composite structure during anti-icing in-flight. Taking into account thermodynamic and aerodynamic aspects, such as the impact of material properties on heat conduction, relative velocities affecting the heat transfer coefficient or flow behavior near the surface, has deepened the comprehension of thermal distribution patterns. Based on the obtained results, optimization approaches such as additional heaters along the upper surface and an integrated copper layer to enhance the internal temperature distribution showed promising results. The prevention of runback ice, along with a reduction in internal temperature while expanding the operational range concerning temperature conditions and liquid water content, was successfully achieved. The present work represents a solution to close the gap between external requirements of anti-icing and internal temperature limits and on the same time set the basis for future ETIPS developments.

In some of the most remote locations around the world, UAVs often represent the only possibility to ensure a medical- and emergency-care for the people living there. Due to the growing demand of UAVs in such fields, operations in highly challenging geographically and weather conditions have become crucial. The presented approaches will enable a robust and highly reliable anti-icing solution for UAV propellers to ensure safe operations and thereby grants many people access to modern medical care.

8 References

[1] P. Mátyás and N. Máté, Brief history of UAV development, Repüléstudományi Közlemények, vol. 31, no. 1, pp. 155-166, 2019.

[2] R. W. Gent, N. P. Dart and J. T. Cansdale, Aircraft icing, Philosophical Transactions of the Royal Society of London. Series A: Mathematical, Physical and Engineering Sciences, no. 358, pp. 2873-2911, 2000.

[3] R. Hann and T. A. Johansen, Unsettled Topics in Unmanned Aerial Vehicle Icing, SAE EDGE Research, 2020.

[4] R. A. Siquig, Impact of Icing on Unmanned Aerial Vehicle (UAV) Operations, Naval Environmental Prediction Research Facility Report, 1990.

[5] "The world's first ice protection solution for UAS approved by the Norwegian Ministry of Defense," Ubiq, [Online]. Available: https://www.ubiqaerospace.com/post/the-world-s-first-ice-protection-solution-for-uas-approved-by-the-norwegian-ministry-of-defense. [Accessed 21 August 2023].

[6] M. B. Bragg, A. P. Broeren and L. A. Blumenthal, Iced-airfoil aerodynamics, Progress in Aerospace Sciences, vol. 41, no. 5, pp. 323-362, 2005.

[7] K. Szilder and S. McIlwain, In-flight icing of UAVs - The influence of reynolds number on the ice accretion process, SAE Technical Papers, 2011.

[8] R. Hann, A. Enache, M. C. Nielsen, B. N. Stovner, J. van Beeck, T. A. Johansen and K. T. Borup, Experimental Heat Loads for Electrothermal Anti-Icing and De-Icing on UAVs, Aerospace, vol. 8, no. 83, pp. 1-15, 2021.

[9] O. Bünte, MIT-Drohnenunternehmen Aviant startet Lieferservice Kyte in Norwegen, heise online, https://www.heise.de/news/MIT-Drohnenunternehmen-Aviant-startet-Lieferservice-Kyte-in-Norwegen-9179776.html, 2023.

[10] R. Hann, Atmospheric Ice Accretions, Aerodynamic Icing Penalties, and Ice Protection Systems on Unmanned Aerial Vehicles, 2020.

[11] N. C. Müller and R. Hann, UAV Icing: 3D Simulations of Propeller Icing Effects and Anti-Icing Heat Loads, 2023.

[12] "UBIQ," Ubiq, [Online]. Available: https://www.ubiqaerospace.com/. [Accessed 21 August 2023].

[13] K. K. Chawla, Composite materials. Science and engineering, 3. ed.New York, Heidelberg: Springer, 2012.

[14] M. Hassanalian and A. Abdelkefi, Classifications, applications, and design challenges of drones: A review, Progress in Aerospace Sciences, vol. 91, pp. 99-131, 2017.

[15] P. S. RAMESH and J. V. MURUGA LAL JEYAN, Comparative Analysis of Fixed-Wing, Rotary-Wing and Hybrid Mini Unmanned Aircraft Systems (UAS) from the Applications Perspective, INCAS BULLETIN, vol. 14, no. 1, pp. 137-151, 2022.

[16] "Zipline Instant Delivery & Logistics," [Online]. Available: https://www.flyzipline.com/. [Accessed 8 August 2023].

[17] U.S. Air Force Photo / Lt. Col. Leslie Pratt, Public domain, via Wikimedia Commons, https://upload.wikimedia.org/wikipedia/commons/8/89/MQ-9_Reaper_UAV.jpg.
[18] https://luftrettung.adac.de/multikopter/.
[19] C. N. Eastlake, An aerodynamicist's view of Lift, Bernoulli, and Newton, The Physics Teacher, vol. 40, no. 3, pp. 166-173, 2002.
[20] A. Sóbester and A. I. J. Forrester, Aircraft aerodynamic design. geometry and optimizationChicester: Wiley, 2015.
[21] FAA, 14 CFR appendix c to part 25, LII / Legal Information Institute; https://www.law.cornell.edu/cfr/text/14/appendix-C_to_part_25.
[22] H. Schlichting, Boundary-Layer Theory, 9th ed. 2017Berlin, Heidelberg: Springer, 2017.
[23] W. Johnson, Helicopter TheoryNewburyport: Dover Publications, 2012.
[24] B. W. McCormick, Aerodynamics, aeronautics, and flight mechanics, 2. ed.Hoboken, NJ: Wiley, 1995.
[25] D. Uhlig and M. Selig, Post Stall Propeller Behavior at Low Reynolds Numbers, 2008.
[26] P. von Böckh and T. Wetzel, Wärmeübertragung. Grundlagen und Praxis, 5th ed.Berlin, Heidelberg: Springer Vieweg, 2014.
[27] B. Weigand and J. von Wolfersdorf, Manuskript zur Vorlesung Wärmeübertragung, 2007.
[28] J. B. J. Fourier, The analytical theory of heat, New York, Dover Publishers, 1955.
[29] S. B. Giddings, Hawking radiation, the Stefan–Boltzmann law, and unitarization, Physics Letters B, vol. 754, pp. 39-42, 2016.
[30] J. Dohmann, Verdunstungskühlung, pp. 171–182, 2016.
[31] B. Weigand, J. Köhler and J. von Wolfersdorf, Thermodynamik kompakt, 4th ed.Springer Vieweg, 2016.
[32] N. Fajt, R. Hann and T. Lutz, The influence of meteorological conditions on the icing performance penalties on a uav airfoil, 2019.
[33] E.W. Brouwers, J.L. Palacios, E.C. Smith and A.A. Peterson, The experimental investigation of a rotor hover icing model with shedding, 1st ed.Phoenix, AZ: American Helicopter Society 66th Annual Forum, 2010.
[34] N. C. Müller, B. Løw-Hansen, K. T. Borup and R. Hann, UAV icing: Development of an ice protection system for the propeller of a small UAV, Cold Regions Science and Technology, 2023.
[35] S. Nilamdeen, Y. Zhang, I. Ozcer and G. S. Baruzzi, An Ice Shedding Model for Rotating Components, 2019.
[36] N. C. Müller and R. Hann, UAV Icing: A Performance Model for UAV Propeller in Icing Conditions, AIAA AVIATION 2022 Forum, pp. 1-17, 2022.
[37] O. Fakorede, Z. Feger, H. Ibrahim, A. Ilinca, J. Perron and C. Masson, Ice protection systems for wind turbines in cold climate: characteristics, comparisons and analysis, Renewable and Sustainable Energy Reviews, vol. 65, pp. 662-675, 2016.
[38] R. J. Flemming, A History of Ice Protection System Development at Sikorsky Aircraft, 2003.
[39] R. W. Gent, R. J. Moser, J. T. Cansdale and N. P. Dart, The Role of Analysis in the Development of Rotor Ice Protection Systems, 2003.
[40] É. Villeneuve, A. Samad, C. Volat, M. Béland and M. Lapalme, Experimental assessment of the ice protection effectiveness of icephobic coatings for a hovering drone rotor, Cold Regions Science and Technology, vol. 210, p. 103858, 2023.

[41] N. Karpen, S. Diebald, F. Dezitter and E. Bonaccurso, Propeller-integrated airfoil heater system for small multirotor drones in icing environments: Anti-icing feasibility study, Cold Regions Science and Technology, vol. 201, p. 103616, 2022.

[42] N. A. Grunina, T. V. Belopolskaya and G. I. Tsereteli, The glass transition process in humid biopolymers. DSC study, Journal of Physics: Conference Series, vol. 40, pp. 105-110, 2006.

[43] Q. Xue, C. Lv, M. Shan, H. Zhang, C. Ling, X. Zhou and Z. Jiao, Glass transition temperature of functionalized graphene–polymer composites, Computational Materials Science, vol. 71, pp. 66-71, 2013.

[44] ANSYS, Inc., Ansys FENSAP-ICE User Manual, no. 22.2, 2022.

[45] W. G. Habashi, F. Morency and H. Beaugendre, FENSAP-ICE: A Second Generation 3D CFD-based In-Flight Icing Simulation System, 2003.

[46] F. Morency, H. Beaugendre, G. Baruzzi and W. Habashi, FENSAP-ICE - A comprehensive 3D simulation system for in-flight icing, 06112001.

[47] R. Schwarze, CFD-Modellierung. Grundlagen und Anwendungen bei StrömungsprozessenBerlin, Heidelberg: Springer Berlin Heidelberg, 2012.

[48] J. D. Anderson, Fundamentals of aerodynamics, Sixth editionNew York, NY: McGraw-Hill Education, 2017.

[49] C. D. Munz and T. Westermann, Numerische Behandlung gewöhnlicher und partieller Differenzialgleichungen. Ein anwendungsorientiertes Lehrbuch für Ingenieure, 4. Aufl. 2019Berlin, Heidelberg: Springer Berlin Heidelberg, 2018.

[50] N. A. Fallah, C. Bailey, M. Cross and G. A. Taylor, Comparison of finite element and finite volume methods application in geometrically nonlinear stress analysis, Applied Mathematical Modelling, vol. 24, no. 7, pp. 439-455, 2000.

[51] I. Eames and J. B. Flor, New developments in understanding interfacial processes in turbulent flows, Philosophical Transactions of the Royal Society of London. Series A: Mathematical, Physical and Engineering Sciences, vol. 369, no. 1937, pp. 702-705, 2011.

[52] A. Favre, Equations des gaz turbulents compressibles, J. de Mecanique, 1965.

[53] A. J. A. Favre, Formulation of the Statistical Equations of Turbulent Flows with Variable Density, pp. 324–341, 1992.

[54] D. D. Gray and A. Giorgini, The validity of the boussinesq approximation for liquids and gases, International Journal of Heat and Mass Transfer, vol. 19, no. 5, pp. 545-551, 1976.

[55] C. J. Chen, C.-J. Chen and S.-Y. Jaw, Fundamentals of turbulence modelingWashington, DC: Taylor & Francis, 1998.

[56] D. C. Wilcox, Formulation of the k-w Turbulence Model Revisited, AIAA Journal, vol. 46, no. 11, pp. 2823-2838, 2008.

[57] P. SPALART and S. ALLMARAS, A one-equation turbulence model for aerodynamic flows, 01061992.

[58] F. R. Menter, Two-equation eddy-viscosity turbulence models for engineering applications, AIAA Journal, vol. 32, no. 8, pp. 1598-1605, 1994.

[59] I. Ozcer, D. Switchenko, G. S. Baruzzi and J. Chen, Multi-Shot Icing Simulations with Automatic Re-Meshing, 2019.

[60] Y. Bourgault, Z. Boutanios and W. G. Habashi, Three-Dimensional Eulerian Approach to Droplet Impingement Simulation Using FENSAP-ICE, Part 1: Model, Algorithm, and Validation, Journal of Aircraft, vol. 37, no. 1, pp. 95-103, 2000.

[61] Y. Bourgault, W. G. Habashi, J. Dompierre and G. S. Baruzzi, A finite element method study of Eulerian droplets impingement models, International Journal for Numerical Methods in Fluids, vol. 29, no. 4, pp. 429-449, 1999.

[62] H. Beaugendre, F. Morency and W. G. Habashi, Development of a Second Generation In-Flight Icing Simulation Code, Journal of Fluids Engineering, vol. 128, no. 2, pp. 378-387, 2006.
[63] H. Beaugendre, F. Morency and W. G. Habashi, FENSAP-ICE's Three-Dimensional In-Flight Ice Accretion Module: ICE3D, Journal of Aircraft, vol. 40, no. 2, pp. 239-247, 2003.
[64] F. Morency, F. Tezok and I. Paraschivoiu, Anti-Icing System Simulation Using CANICE, Journal of Aircraft, vol. 36, no. 6, pp. 999-1006, 1999.
[65] I. A. Ozcer, G. S. Baruzzi, T. Reid, W. G. Habashi, M. Fossati and G. Croce, FENSAP-ICE: Numerical Prediction of Ice Roughness Evolution, and its Effects on Ice Shapes, 2011.
[66] G. Croce, H. Beaugendre and W. Habashi, CHT3D - FENSAP-ICE conjugate heat transfer computations with droplet impingement and runback effects, 01142002.
[67] “Mejzlik.eu - Design and manufacturing top-quality propellers,” [Online]. Available: https://www.mejzlik.eu/. [Accessed 11 July 2023].
[68] “Pointwise for Computational Fluid Dynamics Meshing,” [Online]. Available: https://www.cadence.com/en_US/home/tools/system-analysis/computational-fluid-dynamics/pointwise.html. [Accessed 2 October 2023].
[69] “NX software | Siemens Software,” Siemens Digital Industries Software, [Online]. Available: https://plm.sw.siemens.com/de-DE/nx/. [Accessed 11 July 2023].
[70] “Airfoil Tools,” [Online]. Available: http://airfoiltools.com/index. [Accessed 11 July 2023].
[71] P. J. Roache and P. M. Knupp, Completed Richardson extrapolation, Communications in Numerical Methods in Engineering, vol. 9, no. 5, pp. 365-374, 1993.
[72] T. O. Hodson, Root-mean-square error (RMSE) or mean absolute error (MAE): when to use them or not, Geoscientific Model Development, vol. 15, no. 14, pp. 5481-5487, 2022.
[73] T. Ohmura, M. Tsuboi and T. Tomimura, Estimation of the Mean Thermal Conductivity of Anisotropic Materials, International Journal of Thermophysics, vol. 23, no. 3, pp. 843-853, 2002.
[74] K. Dong, B. Gu and B. Sun, Comparisons of thermal conductive behaviors of epoxy resin in unidirectional composite materials, Journal of Thermal Analysis and Calorimetry, vol. 124, no. 2, pp. 775-789, 2016.
[75] H. Zhang, W.-Z. Fang, Y.-M. Li and W.-Q. Tao, Experimental study of the thermal conductivity of polyurethane foams, Applied Thermal Engineering, vol. 115, pp. 528-538, 2017.
[76] H. Zhang, K. Wu, G. Xiao, Y. Du and G. Tang, Experimental study of the anisotropic thermal conductivity of 2D carbon-fiber/epoxy woven composites, Composite Structures, vol. 267, p. 113870, 2021.
[77] “Laminate Calculator - R&G Faserverbundwerkstoffe GmbH,” [Online]. Available: https://www.r-g.de/en/laminatecalculator.html. [Accessed 24 July 2023].
[78] D. Miller, T. Bond, D. Sheldon, W. Wright, T. Langhals, K. Al-Khalil and H. Broughton, Validation of NASA thermal ice protection computer codes. I - Program overview.
[79] W. Wright, K. Al-Khalil and D. Miller, Validation of NASA thermal ice protection computer codes. II - LEWICE/Thermal, 01061997.
[80] K. Al-Khalil, C. Horvath, D. Miller and W. Wright, Validation of Thermal Ice Protection Computer Codes: Part 3- The Validation of ANTICE, 35th Aerospace Sciences Meeting 01061997, 2001.
[81] W. Johnson, Helicopter theory, Unabridged and slightly corr. republ., [Nachdr.]New York: Dover, 1994.

[82] T. Mikko, J. Tuomas, M. Lasse and B. Geert-Jan, VTT Icing wind tunnel 2.0, Winterwind Presentations 2016, 2016.

[83] “Series 1780: Drone Thrust Stand,” T. Robotics, [Online]. Available: https://www.tytorobotics.com/pages/series-1780. [Accessed 31 July 2023].

[84] KONTRONIK - Hochleistungsantriebe im RC-Modellbau.

[85] “Q80-9M V2 kv160 | Hacker Q80 | Hacker Außenläufer | Elektromotoren,” [Online]. Available: https://www.hacker-motor-shop.com/Elektromotoren/Hacker-Aussenlaeufer/Hacker-Q80/Q80-9M-V2-kv160.htm?SessionId=&a=article&ProdNr=37418022&p=2986. [Accessed 31 July 2023].

[86] “GHS38109 series High Speed Slip Ring(+Electric Slip Rings) - MOFLON,” [Online]. Available: https://www.moflon.com/ghs38109.html. [Accessed 31 July 2023].

[87] Eaton, Technical Data ELX1105; https://www.eaton.com/content/dam/eaton/products/electronic-components/resources/da[…]ass-sealed-radial-lead-ntc-thermistor-datasheet-elx1105-en.pdf, 2021.

[88] A. Carozza, F. Petrosino and G. Mingione, Numerical procedure for the simulation of an electro-thermal anti-icing system, Aircraft Engineering and Aerospace Technology, vol. 94, no. 8, pp. 1433-1448, 2022.

[89] X. Bu, G. Lin, J. Yu, S. Yang and X. Song, Numerical simulation of an airfoil electrothermal anti-icing system, Proceedings of the Institution of Mechanical Engineers, Part G: Journal of Aerospace Engineering, vol. 227, no. 10, pp. 1608-1622, 2013.

[90] E. Iuliano and M. Ferraiuolo, Coupled numerical simulation of anti-icing problems, 978-84-946909-2-1, 2020.

[91] A. Leslie, K. C. Wong and D. Auld, Broadband Noise Reduction on a mini-UAV Propeller, 2008.

[92] R. K. Jeck, Icing Design Envelopes (14 CFR Parts 25 and 29, Appendix C) Converted to a Distance-Based Format, Federal Aviation Administration, 2002.